Deep Sub-Wavelength Terahertz Near-Field Spectroscopy

Lassen, Henrik Bødker

Publication date:
2023

Document Version
Publisher's PDF, also known as Version of record

Citation (APA):
Lassen, H. B. (2023). *Deep Sub-Wavelength Terahertz Near-Field Spectroscopy*. Technical University of Denmark.

DTU ELECTRO
Department of Electrical and Photonics Engineering

Deep Sub-Wavelength Terahertz Near-Field Spectroscopy

Author: Henrik Bødker Lassen

Author: Henrik Bødker Lassen

Supervisor: Assoc. Prof. Edmund J. R. Kelleher
Co-supervisor: Prof. Peter Uhd Jepsen

DTU Electro
Department of Electrical and Photonics Engineering
Technical University of Denmark
Ørsteds Plads
Building 343
2800 Kongens Lyngby, Denmark

To my uncle

Per Anker Jensen

Preface

This thesis is submitted as a requirement in candidacy for a Ph.D. degree in Photonics Engineering at the Technical University of Denmark (DTU). The project was carried out from November 2020 to October 2023 in the Ultrafast Infrared and Terahertz Science group at the Department of Electrical and Photonics Engineering (DTU Electro). The project was under supervision of the main supervisor Associate Professor Edmund. J. R. Kelleher and co-supervisor Professor Peter Uhd Jepsen.

The resultsin this thesis were obtained at the DTU in the period from November 2020 to October 2023. Finite-element method simulations were conducted by Professor Peter Uhd Jepsen and Associate Professor Edmund J. R. Kelleher. The molybdenum disulfide nanoribbons were grown, and characterised with Raman spectroscopy and SEM by Dr. Ganesh Ghimire and Dr. Denys Miakota in the group of Senior Researcher Stela Canulescu at DTU Electro. All exfoliated graphene samples were prepared and optical microscopy images were obtained by Leonid Iliushyn in the group of Associate Professor Tim Booth at DTU Physics. The platinum thin-films and M4PP measurements were prepared by Jonas D. Buron at Capres A/S - a KLA company. The magic-angle twisted bilayer devices were prepared by Dr. Tuan Khanh Chau along with the optical microscope images in the group of Professor Peter Bøggild at DTU Physics. The bowtie antenna structure was fabricated by Dr. Matej Sebek in group of Professor Peter Uhd Jepsen at DTU Electro.

This project was mainly funded by Danmarks Frie Forskningsfond (DFF) on a DFF Sapere Aude project (ULTRA-LOWD) with partial co-funding from DTU Electro. Carlsberg Foundation funded the THz-TDS extension for the system (DEEP-MAP). Center for Nanostructured Graphene (CNG) indirectly funded the project through the acquisition of the NeaSpec microscope. I received funding from Otto Mønsteds Fond for participation at conferences in The Netherlands and France and for my external stay at Osaka University, Japan, I received funding from Otto Mønsteds Fond, P. A. Fiskers Fond, Augustinus Fonden, and William Demant Fonden.

Henrik Bødker Lassen
Kongens Lyngby, 16th November 2023

Acknowledgements

Throughout my whole study career at the Technical University of Denmark, I have had the pleasure of completing my Bachelor's and Master's theses, and now, embarking on a Ph.D. in terahertz science with with **Prof. Peter Uhd Jepsen**.

Back in 2020, I had the pleasure of doing my Master's thesis in collaboration with **Prof. Koichiro Tanaka** at Kyoto University, and I remember at the end of the stay, Prof. Tanaka suggested that I should continue and do a Ph.D., which at that point I had yet to think more about. That was when I had the pleasure to come into contact with **Assoc. Prof. Edmund J. R. Kelleher** about a recent Ph.D. position with him and Peter, which, in the end, I was lucky to be offered. This was the beginning to an unforgettable 3 years at DTU studying terahertz science under their supervision.

Ed - Thank you for giving me the chance to study a whole new field together and for allowing me to pursue whatever idea and thought I had during the last 3 years. Our weekly 2-hour supervisory meetings with Peter scheduled in the calendar from 9 a.m. to 10 a.m. have been utmost fun and informative, though I do not recall many times we have kept the allocated time. Your immense interest in all scientific aspects has left a huge impact on my view of science and how to approach different topics.

Peter - Thank you for introducing me to the world of photonics and terahertz all the way back in my first semester as a bachelor student, now 8 years ago and for being a great supervisor through all the years. I have learned a lot from your extensive knowledge not only about terahertz but about all aspects of optics and lasers. Your humour and witty jokes made the atmosphere in the group amazing, as well as having an excellent taste in music.

Furthermore, during my journey at DTU, I had the delightful opportunity to meet numerous colleagues and friends. Their presence greatly enriched my experience, and I wish to mention and express my sincere appreciation for their support and camaraderie.

Mattias Rasmussen, with whom I have been studying since our Bachelor's enrolment, and now we have both completed our Ph.D.s in the same group His friendship and support have been invaluable throughout the years, as well as having an identical study style made for a perfect partnership. On a personal level, I enjoyed

our jamming sessions, where I have been taught most of what I know about guitars, and our enjoyment of Czech beer.

Dr. Tobias Buchmann for his guidance and willingness to help whether that be a fundamental question or aiding in the lab. Furthermore, having a great sense of humour contributed to lively and enjoyable office banter, something I'm confident our colleagues would enthusiastically agree with. Sharing many interests and studying Japanese together, where we after each class celebrated our advances with beer, pool, and darts made for amazing memories.

Assoc. Prof. Binbin Zhou for always being available to answer any question and his great expertise in the lab. It has been an utmost pleasure to learn from his many years of maintaining all the lab equipment and experience how to handle sudden breakdowns.

Sergio I. R. Puentes who made the group much more lively and was always ready for beers on Friday evenings, when I was convinced to leave my car at home and take the bus to DTU.

Dr. Malte Welsch, and **Dr. Martin Cross** for their support as fellow Ph.D. students of the same generation and their willingness to entertain me when I stopped by their office for a coffee and banter break.

Dr. Matej Sebek for amazing discussions on promising projects and opportunities, and his great interest in recent results and eagerness to help with measurements in addition to his great knowledge of 2D materials. It has been a joy to both learn and explore various parts of the world together.

Dr. Korbinian J. Kaltenecker for his guidance and help with understanding how to operate the system. **Assoc. Prof. Nicolas Stenger**, and **Dr. Laura Casses** for sharing the NeaSpec system together, their great humour, and friendship.

Leonid Iliushyn for the many pleasant days spent in the lab measuring graphene, and the great discussion about upcoming music ranging from J-pop to metal.

Asst. Prof. Simon Jappe Lange for his immense enthusiasm for terahertz and innovation, which has been nothing less than a pleasure to experience.

My office mate throughout the the three years, **Dr. Miriam Galbiati**, **Lorenza P. Foglia**, **Dr. Simon Christensen**, **Thea Bjørk Kristensen**, **Oliver Nagy**, **Thorsten Bæk**, and **Oscar Garcia** for great discussions and a great office atmosphere.

Prof. Masayoshi Tonouchi and his group at Osaka University. They hosted me for 6 months during my external stay and I had the great pleasure of working under **Prof. Tonouchi** and **Assoc. Prof. Kazunori Serita** and learn their extensive knowledge of terahertz dynamics. Furthermore, a thank you to all the groups members, especially **Fumikazu Murakmi**, **Ms. Mayo Iwami**, **Wang Ke**, and **Yang Dongxun**. They made me feel very welcome and made my time in Japan most enjoyable, sharing many beers and sake.

Lastly, to my family and friends who have supported me through thick and thin throughout all the years. Without all these individuals, and many others whom I may not have mentioned, I would not have had such an enjoyable time as a Ph.D. student and they deserve all the credit. These friendship and connections will hopefully last for a long time.

Thank you very much to everyone.

Abstract

Terahertz time-domain spectroscopy has stretched its influence far, from investigating carrier dynamics and probing the optical and electrical properties of materials to accurately measuring layer thicknesses of compound materials. In this thesis, we combine this technique with scattering-type scanning near-field optical microscopy, an optical microscopy method independent of the wavelength. A general introduction to the fundamentals of this technique is given along with the state-of-the-art theoretical models describing the near-field interactions.

The first part focuses on nanoribbons of the semiconductor molybdenum disulfide and aims to extract the optical properties in the THz range. We find that from the coined *whitelight* scans, which occurs when the delay stage in the terahertz generation system is parked at the peak intensity in the time domain, we can extract the real part of the permittivity and present it as a two-dimensional spatial map. Additionally, full spectroscopic analysis of the sample in question reveals a first attempt at extracting the full complex dielectric function in the near-field for these enhanced nanoribbons in the spectral range from 0.5 THz to 1.5 THz.

The second part shifts the focus to conductive materials with the aim of investigating and quantitatively extracting the conductivity at the nanoscale. Despite current state-of-the-art theory predicting conductive surfaces to be near-perfect reflectors even with a low conductivity, we experimentally observe contrast stemming from variations in conductivity. We show that we can indeed distinguish between layers of graphene and thicknesses of platinum thin films due to the difference in conductivity and support these findings with finite element method simulations. Excellent agreement between experimental observations and simulations provides a promising foundation for analysing the optical and electrical properties of conductive surfaces in the near-field with terahertz techniques.

Lastly, the third part aims to provide an overview of ongoing research topics of more complex nature and devices. We aim to map the field enhancement of a resonant gold structure and through our broadband source we are able to spatially map the resonant behaviour in the structure. Additionally, magic-angle twisted bilayer graphene is studied and shows a decrease in scattered signal compared to AB stacked bilayer and monolayer, attributed to structural changes in the properties of the material.

Overall, this thesis highlights the many applications of performing terahertz spectroscopy at the nanoscale and provides the foundation upon which further improvements will be built.

Resumé

Anvendelserne af terahertz tidsdomæne-spektroskopi har en stor rækkevidde fra at undersøge ladningsbærerdynamik og udtrækkelse af de optiske og elektriske egenskaber af materialer helt til nøjagtigt at måle lagtykkelser af sammensatte materialer. I denne afhandling kombinerer vi denne teknik med spredningstype scanning nær-felt optisk mikroskopi, som er en optisk mikroskopimetode uafhængig af bølgelængden. En generel introduktion til grundlaget for denne teknik gives sammen med de nyeste teoretiske modeller, der beskriver nær-felts interaktionerne.

Første del fokuserer på nano-bånd af halvlederen molybdændisulfid og sigter mod at udtrække de optiske egenskaber i THz-området. Vi finder, at fra de såkaldte "hvidlys" skanninger, som er når forsinkelsesbåndet i terahertz-genereringssystemet er parkeret på maksimale intensitet i tidsdomænet, er vi i stand til at udtrække den reelle del af permittiviteten og præsentere den i et todimensionalt rumligt kort. Derudover afslører en fuld spektroskopisk analyse af prøven et første forsøg på at udtrække den fulde komplekse dielektriske funktion i nær-feltet for disse forbedrede nanobånd i det spektrale område fra 0,5 THz til 1,5 THz.

Anden del skifter fokus til ledende materialer med det mål at kvantitativt udtrække ledningsevnen på en nanoskala. På trods af, at nuværende state-of-the-art teorier forudsiger ledende overflader at være næsten perfekte reflektorer selv med en lav ledningsevne, observerer vi eksperimentelt kontrast som følge af variationer i ledningsevnen. Vi viser, at vi faktisk er i stand til at skelne mellem lag af grafen og tykkelser af platin tyndfilm på grund af forskellen i ledningsevne og understøtter disse fund med finite element method simuleringer. Fremragende overensstemmelse mellem eksperimentelle observationer og simuleringer giver et lovende fundament for at analysere de optiske og elektriske egenskaber af ledende overflader i nær-feltet med terahertz-teknikker.

Endelig sigter tredje del mod at give et overblik over igangværende forskningsemner af mere kompleks natur og prøveopbygninger. Vi sigter mod at kortlægge felt-forstærkningen af en resonant guldstruktur og gennem vores bredbåndskilde er vi i stand til rumligt at kortlægge den resonante adfærd i strukturen. Derudover studeres magisk-vinkel roteret bilags grafen og viser en nedgang i spredt signal sammenlignet med et enkeltlag, som tilskrives strukturelle ændringer i materialets egenskaber.

Samlet set fremhæver denne afhandling de mange anvendelser af at udføre terahertz-spektroskopi på en nanoskala og grundlægger fundamentet, hvorpå yderligere forbedringer vil blive bygget.

Publications and contributions

Journal publications

Included in this thesis

- Henrik B. Lassen, Edmund J. R. Kelleher, Leonid Iliushyn, Timothy J. Booth, Peter Bøggild, and Peter U. Jepsen,
  "Terahertz s-SNOM reveals nanoscale conductivity of graphene" (**submitted**)
- Henrik B. Lassen, Ganesh Ghimire, Denys I. Miakota, Stela Canulescu, Edmund J. R. Kelleher, and Peter U. Jepsen,
  "Terahertz nanoscopy of MoS_2 nanoribbons" (**in preparation**)

Additional work not included

- Korbinian J. Kaltenecker, Shreesha Rao D. S., Mattias Rasmussen, Henrik B. Lassen, Edmund J. R. Kelleher, Enno Krauss, Bert Hecht, N. Asger Mortensen, Lars Grüner-Nielsen, Christos Markos, Ole Bang, Nicolas Stenger, and Peter Uhd Jepsen,
  "Near-infrared nanospectroscopy using a low-noise supercontinuum source,"
  APL Photonics, vol. 6, 6 2021.

Conference contributions

- Henrik B. Lassen, Jonas D. Buron, Roy Kelner, Peter F. Nielsen, Edmund J. R. Kelleher, and Peter Uhd Jepsen,
  "THz nanoscopy of platinum thin films",
  2022 47th International Conference on Infrared, Millimeter and Terahertz Waves (IRMMW-THz), Delft, Netherlands, 2022, pp. 1-2, doi: 10.1109/IRMMW-THz50927.2022.9896118. (**talk**)

- Henrik B. Lassen, Jonas D. Buron, Roy Kelner, Peter F. Nielsen, Edmund J. R. Kelleher, and Peter Uhd Jepsen,
  "THz nanoscopy of platinum thin film conductivity",
  2022 9th International Conference on Optical Terahertz Science and Technology (OTST), Budapest, Hungary, 2022. (**poster**)

- Henrik B. Lassen, Jonas D. Buron, Roy Kelner, Peter F. Nielsen, Edmund J. R. Kelleher, and Peter Uhd Jepsen,
  "Terahertz nanoscopy of thin film metals",
  2022 2nd International Nanoscale Analytics Workshop, Munich, Germany, 2022. (**talk**)

- Henrik B. Lassen, Mohsen Ahmadi, Zhipei Sun, Peter Bøggild, Edmund J. R. Kelleher, and Peter Uhd Jepsen,
  "THz nano-imaging of conductivity inhomogeneity in CVD-grown graphene",
  Graphene2021, Grenoble, France, 2021. (**talk**)

Abbreviations

AFM	Atomic force microscope
Au	Gold
CNG	Charge neutrality point
CVD	Chemical vapour deposition
CW	Continuous wave
EO	Electro-optic sampling
FDM	Finite dipole model
FEM	Finite element method
Gr	Graphene
hBN	Hexagonal boron nitride
LT-GaAs	low-temeperature grown gallium arsenide
LTEM	Laser emission terahertz microscopy
M4PP	Micro four-point probe
MoS_2	Molybdenum disulfide
mtBLG	Magic-angle twisted bi-layer graphene
N_2	Nitrogen
NSOM	Near-field scanning optical microscopy
OPTP	Optical-pulse terahertz-probe
PCA	Photo-conductive antenna
PDM	Point dipole model
PLD	Pulsed laser deposition

Pt	Platinum
QCL	Quantum cascade laser
RPA	Random phase approximation
$\mathbf{RuCl_3}$	Ruthenium trichloride
s-SNOM	Scattering-type scanning near-field optical microscopy
SEM	Scanning electron microscope
SNR	Signal-to-noise ratio
SPM	Scanning probe microscopy
SRR	Split-ring resonator
STM	Scanning tunnelling microscope
TDS	Time domain spectroscopy
THz	Terahertz
THz-SNOM	s-SNOM combined with THz-TDS

Contents

Introduction

In the pursuit of technological advancement, the miniaturisation of devices has become a pivotal trend, propelling industries into an era where the functional limits of materials and components are tested at previously unimaginable length scales. The relentless drive toward smaller, faster, and more efficient systems has necessitated a profound understanding of the fundamental principles governing matter's behaviour at the nanoscale. Physics, as the bedrock of all material sciences, plays a critical role in this quest, offering insights that are essential for innovation.

The nanoscale is a realm where the classical laws of physics start to intertwine with quantum phenomena, giving rise to entirely new properties and behaviours. As we engineer devices that approach these dimensions, traditional approaches and understandings no longer suffice. The electrons, photons, and other quanta, which operate seamlessly in bulk material, begin to exhibit peculiar characteristics due to quantum confinement, surface effects, and the increased significance of intermolecular forces.

Therefore, the study of nanoscale physics is a gateway to the future, enabling us to conceive and fabricate materials with tailor-made properties, engineer devices with unparalleled performance, and solve some of the most pressing challenges of our time. As we continue to shrink the building blocks of technology, the need for an intimate knowledge of nanoscale physics becomes not just beneficial but essential.

0.1 Microscopy and Optical near-field techniques

Characterising materials at the nanoscale is an intricate endeavour that challenges our ability to observe, measure, and manipulate matter with precision. Sophisticated techniques such as scanning tunnelling microscopy (STM), atomic force microscopy (AFM), and electron microscopy have been developed to visualise the nanoworld, while spectroscopic methods like Raman spectroscopy and X-ray diffraction provide insights into the structural and electronic properties of materials, though still being limited in their spatial resolution. Here, we will mention some of these characterisation methods used to study material at the nanoscale.

0.1.1 Atomic force microscopy

Atomic Force Microscopy (AFM) is a powerful microscopy technique under the umbrella of scanning probe microscopy (SPM), capable of capturing three-dimensional images of surfaces at the nanometre and even atomic scale [1–5]. AFM is prominently used across multiple disciplines such as material science [6, 7], biology [8, 9], and nanotechnology [7], providing detailed insights into the topographical, mechanical, and chemical properties of samples. AFM operates by utilising a cantilever with a sharp tip at its end, which scans over the surface of a sample. The interactions between the tip and surface forces cause the cantilever to deflect, and these deflections are meticulously measured and mapped to generate a detailed topographic image of the surface [10]. A schematic of this is shown in Figure 0.1(a). A deflection laser is reflected off the backside of the cantilever onto a four-segment photodiode, which is used to monitor slight deviations from its zero position. From these slight variations, height information can be extracted.

An AFM can be run in different configurations depending on which regime in a force-distance curve it is operated. A typical force-distance curve can be seen in Figure 0.1(b) where the different operation regimes have been highlighted. When the tip approaches the surface of the sample, it first feels attractive van der Waals forces and is thus pulled towards the surface before being repelled at closer distances. Operating the AFM in the repellent regime is known as contact mode, while operating in the attractive regime is known as non-contact mode. Another quintessential mode of operation in AFM is the so called *tapping mode*, also known as intermittent mode. Unlike the contact mode, where the tip continuously touches the surface of the sample, the tapping mode allows the cantilever to oscillate at or near its resonance frequency above the surface. As the cantilever gently ”taps” on the sample’s surface during its oscillation cycle, it reduces lateral forces that might damage soft or loosely bound samples, making it particularly advantageous for studying biological specimens or other delicate materials [10].

In tapping mode, feedback mechanisms maintain a constant oscillation amplitude, adjusting the tip-to-sample distance to navigate the sample’s contours effectively. The topography is extracted using a continuously running feedback loop and a proportional-integral-derivative (PID) controller. This mode enables the achievement of high-resolution images, preserving both the tip and the sample’s integrity. The detailed information obtained through tapping mode AFM is instrumental in unveiling surface characteristics offering invaluable data in research and technological developments.

0.1.2 Aperture near-field scanning optical microscopy

Aperture near-field scanning optical microscopy is an advanced optical microscopy technique that transcends the diffraction limit, which traditionally restricts the resolution of conventional optical microscopes, given by the Abbe criterion,

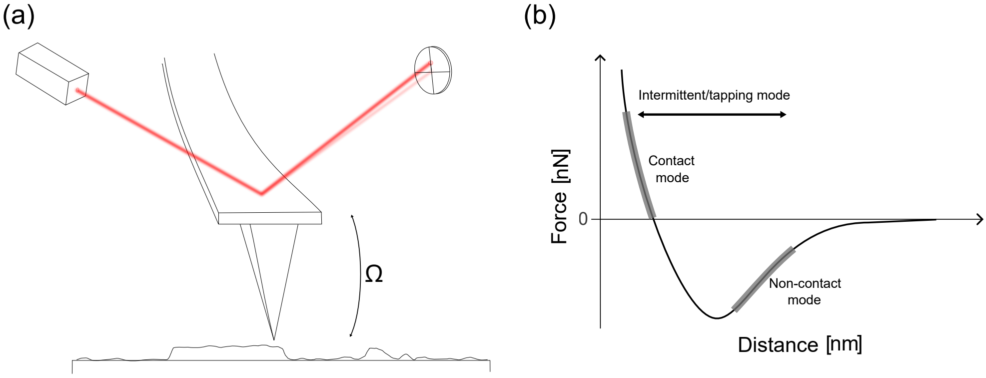

Figure 0.1. (a) Schematic of AFM in tapping mode configuration with tapping frequency Ω, and (b) typical force-distance curve for an AFM with the different operation regimes highlighted.

$$d = 0.61\frac{\lambda_0}{\mathrm{NA}}, \tag{1}$$

where λ_0 is the free-space wavelength and NA is the numerical aperture. This technique is part of the greater Scanning Near-field Optical Microscopy (SNOM) or Near-field Scanning Optical Microscopy (NSOM) family, and it aims to provide a spatial resolution far beyond what conventional optical microscopy offers, enabling the exploration of nanostructures and various phenomena at the nanoscale.

The concept of the technique was first thought up by Synge in 1928 [11], and decades later the first experimental demonstrations of the technique were performed [12–15]. NSOM operates on the fundamental concept of near-field optics, where evanescent waves, which decay rapidly, are studied. In this technique, light is passed through a small aperture at the end of, e.g., a metal-coated, tapered optical fibre, where the aperture is smaller than the wavelength of the light [15]. The fibre is closely positioned near the surface of the sample, often within a few nanometres. Due to the proximity of the aperture to the sample, evanescent waves or near-fields can be captured and analysed, enabling the revelation of ultra-fine details significantly below the wavelength of the light. Aperture near-field scanning optical microscopes typically has a spatial resolution of 50-100 nm, but as low as 10-30 nm can be achieved [15]. A sketch of this is shown in Figure 0.2(a).

The spatial resolution achievable by aperture based near-field optical microscopes is, however, related to the wavelength which is used. Thus, for long wavelengths such as in the THz regime, the use of this technique becomes exceedingly difficult. A similar technique called apertureless near-field scanning optical microscopy, however, is not limited by the wavelength of the light.

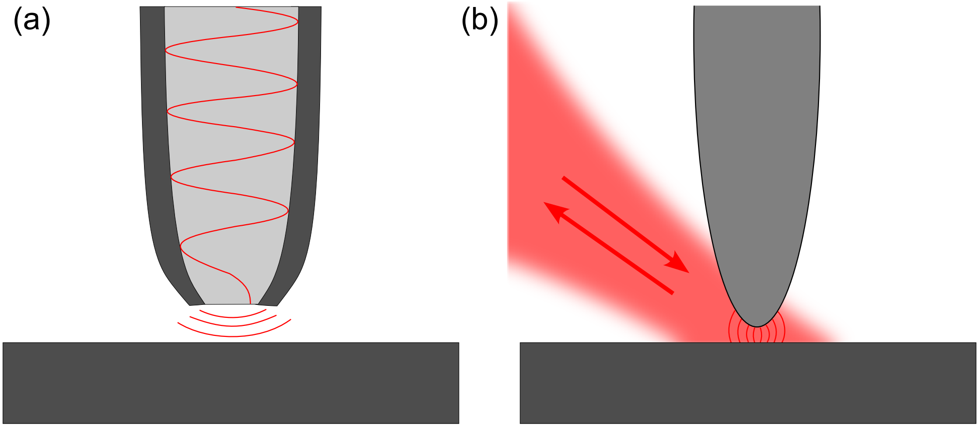

Figure 0.2. (a) Aperture based scanning near-field optical microscope probe where light propagating inside a metallic coated optical fibre is passed through an aperture much smaller than the wavelength. (b) Apertureless scanning near-field optical microscope where light is focused onto adn scatters off a sharp metallic tip subsequently detected in the far-field.

0.1.3 Scattering-type scanning near-field optical microscopy

Apertureless near-field scanning optical microscopy or scattering-type scanning near-field optical microscopy (s-SNOM) is a microscopy technique similar to the aperture based microscopes in which structures, far beyond the diffraction limit of the light in use, are investigated.

The fundamental mechanism of s-SNOM revolves around a sharp metallic probe (usually an AFM tip) that is illuminated by a focused laser [16–19]. As the tip approaches the surface of the sample, it concentrates and scatters the incident light for detection in the far-field, enabling the collection of near-field optical signals from the background signal. An illustration of this principle in shown in Figure 0.2(b).

Most s-SNOM instruments operate on the basis of the aforementioned tapping mode AFM, however, here, instead of scanning the tip across the surface of the sample, we maintain the tip at a fixed position and place the sample on a piezo stage with sub-nanometre control in the z-direction, and nanometre precision in the lateral x, y-directions. The tip oscillates at a given frequency Ω above the sample's surface in the intermittent mode and detected signals are demodulated at this oscillation frequency to extract near-field information. This process effectively separates the relevant signals from unwanted background, thereby achieving remarkable resolution and sensitivity. Notably, the resolution is independent of the incident wavelength and is only limited by the apex radius of the tip [19].

s-SNOM is extraordinarily versatile and applicable in various scientific domains. Its ability to provide high-resolution images along with spectroscopic information [20–22] makes it indispensable for studying complex materials [23], surface plasmons [24–

27], phonon polaritons [28, 29], and various nanoscale optical phenomena. Through s-SNOM, researchers can delve deep into the intricacies of light-matter interactions, unveiling the nature at the nanoscale.

0.2 Terahertz spectroscopy

Terahertz time-domain spectroscopy (THz-TDS) has for many decades been a stable in material characteristics such as optical and electrical properties due to its non-invasive nature [30]. However, a limiting factor is the nature of the diffraction limit, as outlined in Eq. (1). Due to its long wavelength, the spatial resolution is limited to hundreds of microns Therefore, ways to circumvent this limit would open great possibilities within material science.

0.2.1 Laser emission terahertz microscopy

One technique which circumvents this fundamental limit is laser emission terahertz microscopy (LTEM), which studies THz radiation emitted from the surface of materials on a scale much smaller than the wavelength of the THz radiation emitted [31]. This is done, by focusing an optical pump onto the surface of the sample, from where carriers are generated and accelerated through an effect called the photo-Dember effect, which due to the difference in mobility between electrons and holes cause THz emission from the surface. A photoconductive antenna (PCA) can then placed in the near vicinity of the surface in order to avoid significant attenuation of the signal, which detects the emitted THz radiation. A simplified sketch of an LTEM setup can be seen in Figure 0.3.

Through this method, studies of dynamics on a length scale much smaller than the wavelength of the THz radiation used to probe the dynamics can be studied. This method has been pioneered by Prof. Tonouchi at Osaka University and has been used to study integrated circuits and their defects, as well as other material properties [31–35].

Instead of being spatially limited by the THz, in this configuration we are limited by the excitation laser, which in most cases resides in the visible region ($\sim$ 800 nm), since the THz radiation is emitted from the diffraction limited spot of the excitation laser. This then yields a spatial resolution of a few hundreds of nanometres. To further increase the spatial resolution, one could implement the aperture based SNOM from Figure 0.2(a), where the evanescent waves exiting the optical fibre close to the surface of the sample, would be used to generate THz in the surface. With this, one would be able to push the spatial resolution down to below 100 nm, and therefore study a material's carrier dynamics directly on such a length scale.

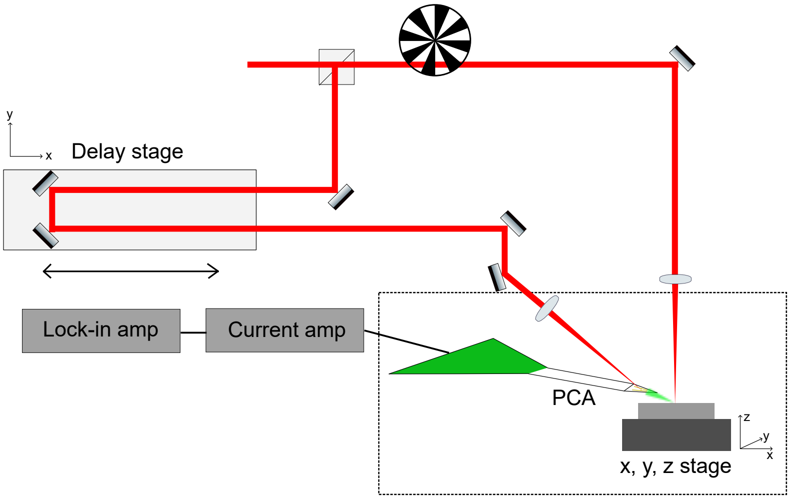

Figure 0.3. Sketch of laser emission terahertz microscopy (LTEM) setup. The probe is split by a 50/50 beam splitter, with one arm used to excite the surface of the sample and the other arm used as a trigger for the photoconductive antenna (PCA). The signal is sent through a fast current amplifier before a lock-in amplifier, referenced to the frequency of the chopper, is used to detect the signal.

0.2.2 Terahertz time domain spectroscopy and s-SNOM

A different approach to study material properties at the nanoscale with THz radiation is to combine far-field THz-TDS with s-SNOM, since the spatial resolution in s-SNOM is independent of the incident light. Thus, even though the wavelength of the THz light is in the order of several hundreds of microns, features all the way down to tens of nanometres would be able to be resolved. An illustration of this is shown in Figure 0.4. Figure 0.4 is an exaggerated sketch, since in reality the tip shank length is around 80 µm and the diffraction limited spot size of the focused THz light is around 150 µm, meaning the THz light would cover not only the whole shank of the tip but also most of the cantilever, which is close to 300 µm in length.

We use PCAs for both generation and detection of the THz radiation. We use a Menlo Systems TeraSmart system where the PCAs are pumped by a 1550 nm, 100 MHz repetition rate, erbium doped fibre laser, which in the far-field has a bandwidth up to 4 THz. Figure 0.5 shows the time-domain trace and associated spectrum in the far-field.

Other source generation than PCAs have also been demonstrated, where, e.g., the aforementioned THz emission spectroscopy, i.e., THz radiation emitted from a surface under illumination of a visible pump, is scattered by the tip into the far-field for detection [36, 37]. Near-field studies with single frequency THz generated through quantum cascade lasers (QCLs) have also seen a plethora of advances with

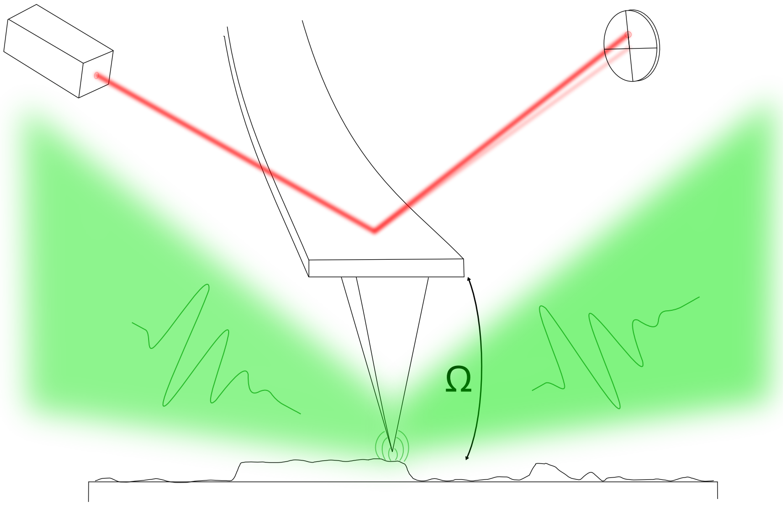

Figure 0.4. Sketch of focusing THz radiation from a photoconductive antenna onto an oscillating, sharp metallic tip, which concentrates the field just below the apex of the tip and scatters to the far-field for detection and demodulation.

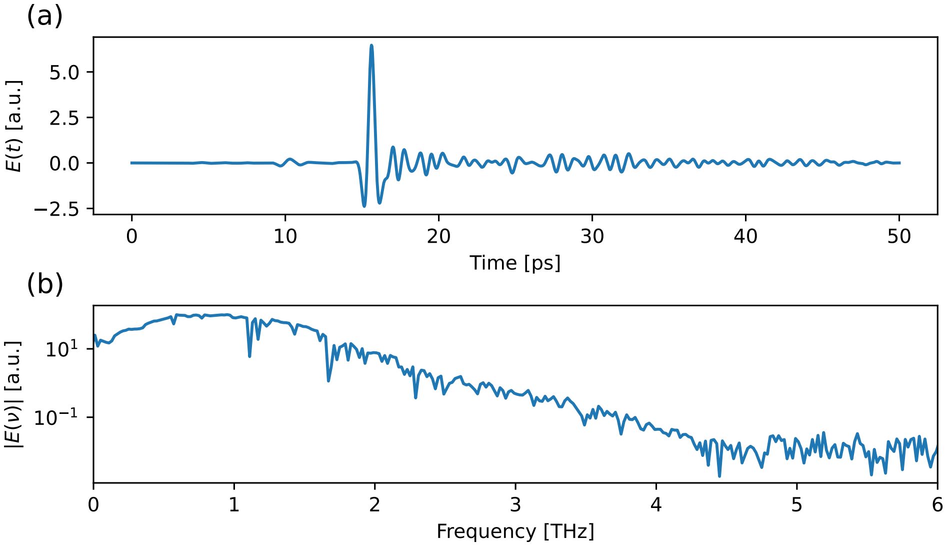

Figure 0.5. (a) Time-domain trace and (b) spectrum of the THz pulse generated by the TeraSmart system in the far-field.

the study of ring resonators [38], quantum-well photodetectors [39], and self-detecting QCLs [40–42], where the source is used for both generation and detection.

In this thesis, we will, through the use of THz-TDS and s-SNOM (THz-SNOM), study a wide variety of materials. Initially, chapter 1 will serve to give an introduction to the theory and models pertaining to s-SNOM and how the near-field interactions are described. In chapter 2, we will discuss and show some of the practices that are used to generate data and discuss tips and tricks gained from working with the system and software. We will discuss how we retrieve the pulse form from the system as well as introduce approach (or retract) curves, which are used to estimate the spatial resolution of a given tip. In chapter 3, we will study the THz near-field response of pulsed laser deposition (PLD) grown molybdenum disulfide nanoribbons and extract the optical properties through its permittivity. The study of highly conductive materials such as graphene and thin-film metals will be the purpose of chapter 4, where we will aim to shed light upon the ability to see contrast between small variations in conductivity. Lastly, chapter 5 and chapter 6 will showcase some of our ongoing projects, where more complicated structures and devices will be investigated, and an outlook into the future of THz-SNOM will be given.

CHAPTER 1

Theoretical concepts and models

To fully uncover all aspects of the near-field interactions, we must first establish a theoretical foundation upon which to build our understanding We will begin by describing the near-field interactions in the simplest way, assuming the tip to be a spherical dipole, and then expand these concepts to include more realistic tip shapes and sample constructions. Lastly, we will adopt a numerical approach to describe the near-field interactions, enabling us to compare these with the analytical models. This chapter will provide the basis for discussing the phenomena we observe. In subsequent chapters, we will explore further extensions to these models and discuss their limitations in fully describing complex systems.

1.1 Point dipole model

The simplest way to describe the interaction between an AFM probe and a dielectric surface involves assuming the probe to be a polarisable sphere with a radius R (see Figure 1.1) [18,19]. The probe, in close proximity to the surface, couples the light to the surface and is then scattered off to the far-field for detection. When an electric field is applied to this polarisable sphere, it is characterised by a dipole moment,

$$\mathbf{p} = \alpha \mathbf{E}, \tag{1.1}$$

where, α, is the polarisability of the sphere, and is given in SI units as [43,44],

$$\alpha = 4\pi\varepsilon_0\varepsilon_{\text{out}} R^3 \frac{\varepsilon_{\text{in}} - \varepsilon_{\text{out}}}{\varepsilon_{\text{in}} + 2\varepsilon_{\text{out}}}. \tag{1.2}$$

Here, ε_{in} and ε_{out} describes the permittivity inside the sphere and outside, respectively. When the sphere, representing the AFM probe, is made out of a solid metal situated in air, then this ratio becomes close to unity due to the extremely high permittivity of the metal. Thus, common practice is assuming the probe to be a perfect conductor [45]. When the dipole is in proximity with a surface, a mirror image of the dipole is formed [18], with a dipole moment given as $p' = \beta\left(\varepsilon\right)p$, with $\beta\left(\varepsilon\right)$ being the electrostatic reflection coefficient or ”near-field reflection coefficient”, which in turn is a function of the permittivity, given as [46],

$$\beta\left(\varepsilon\right)=\frac{\varepsilon_2-\varepsilon_1}{\varepsilon_2+\varepsilon_1}. \tag{1.3}$$

This mirror image dipole acts on the original dipole, thus enhancing it, which in turn enhances the mirror image dipole, and so forth. The total dipole moment of the probe can be found by evaluating this interaction as an infinite sum [47]. The resulting polarisability can be thought as an effective polarisabilty given as,

$$\alpha_{\mathrm{eff},\perp}=\frac{\alpha\left(1+\beta\right)}{1-\frac{\alpha\beta}{16\pi h^3}}, \tag{1.4}$$

for an electric field perpendicular to the surface of the sample, and

$$\alpha_{\mathrm{eff},\parallel}=\frac{\alpha\left(1-\beta\right)}{1-\frac{\alpha\beta}{32\pi h^3}}, \tag{1.5}$$

for an electric field parallel to the surface, with h being the the distance from the centre of the sphere to surface. Due to the nature of the system and the fact that the probe is elongated, the system is predominantly polarised in the perpendicular direction and thus Eq. (1.4) mainly describes the near-field interactions in the PDM [47].

1.1.1 Scattered electric field

The incoming electric field interacts with the probe and sample described by the effective polarisability above, and the electric field radiated by the dipole is then detected in the far-field. This can be described as,

$$E_{sca}=\left(1+r_{\mathrm{s}}\right)^2\alpha_{\mathrm{eff}}E_{\mathrm{inc}}, \tag{1.6}$$

where r_{s} is the Fresnel far-field reflection coefficient, which accounts for the light not interacting with the probe. The pre-factor $\left(1+r_{\mathrm{s}}\right)^2$ takes into account both the reflection from the incoming field and the scattered field from the dipole, and is therefore a squared response [48]. In most cases, due to the fact that the far-field reflection varies over much larger distances than the effective polarisability, simple referencing will remove its contribution to the signal [49]. This is also a standard practice within THz-TDS where the material response is often found from the ratio of a full response and a reference response [30]. Recently, harmonic normalisation have also been used, where harmonics of the same signal are divided with each other, thus not only eliminating the far-field response completely, but also artefacts within the scan itself [50].

1.2 Finite dipole model

The PDM has done well in explaining qualitative phenomena, but is still a simplified description of a complex system and therefore might fail in explaining more complicated phenomena [45]. The finite dipole model (FDM) describes a more realistic tip geometry in assuming the tip to be an elongated spheroid [45, 47] (see Figure 1.1). Following the derivation performed by Ocelic [47], the near-field interactions are described by two charges situated in the elongated spheroid, Q_0 and Q_i and their corresponding mirror images Q_0' and Q_i'. The opposite charges inside the spheroid $-Q_0$ and $-Q_i$ are assumed to not partake in the near-field interactions. The charge Q_i is induced by the image charge Q_0' and can thus, be viewed as a near-field induced charge, which can be found as the solution to the equation,

$$Q_i = \beta \left(f_0 Q_0 + f_1 Q_i \right), \tag{1.7}$$

where, β is, again, the near-field reflection coefficient containing the material properties of the surface underneath the tip in form of the permittivity. The two functions appearing with the charges, f_0 and f_1, are purely geometric function, which account for the shape and curvature of the tip, given as,

$$f_{0,1} = \left(g - \frac{R + 2H + W_{0,1}}{2L} \right) \frac{\ln \frac{4L}{R + 4H + 2W_{0,1}}}{\ln \frac{4L}{R}}. \tag{1.8}$$

These geometric functions are functions of time, due to their dependence on the tapping height of the tip, $H(t)$. The parameters $W_0 = \frac{1.31RL}{L+2R}$ and $W_1 = \frac{R}{2}$ are the approximate positions of the two charges Q_0 and Q_i, respectively, and L is the half-length of the elongated spheroid. The factor g describes the fraction of the total induced charge contained by Q_i, and is typically given as $g = 0.7 \pm 0.1$ [45,47], derived from experimental fits, though other studies suggest the use of a different value [49]. This factor may also contain a phase term, which accounts for slight phase shift [48] stemming from propagation between the charges, however, for THz frequencies this phase term is negligible. The resulting dipole moments arising from these charges are described as,

$$p_0 = 2Q_0 L, \tag{1.9}$$
$$p_i = Q_\mathrm{i} L, \tag{1.10}$$

and after solving Eq. (1.7), the total dipole moment is then expressed as the sum of the two dipole moments,

$$p_\mathrm{eff} = p_0 + p_\mathrm{i} = 2Q_0 L \left(1 + \frac{1}{2} \frac{\beta f_0}{1 - \beta f_1} \right), \tag{1.11}$$

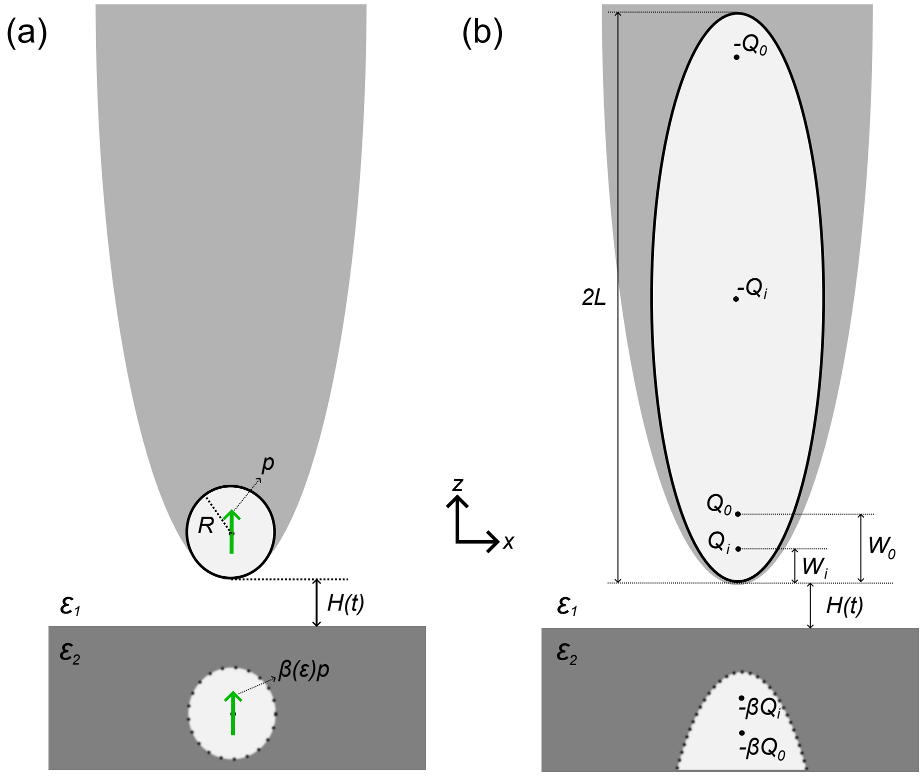

Figure 1.1. (a) Sketch of the PDM where the tip is modelled as a small sphere with radius R. (b) Sketch of the FDM where instead of modelling the tip as a sphere, it is modelled as an elongated sphere to better resemble the actual tip. Adapted from [45].

where the value of the initial monopole is,

$$Q_0 = W_0^2 \left(\gamma_0 - 1\right) E_0, \tag{1.12}$$

with γ_0 being the enhancement factor of field provided by the presence of the tip, which contains the relevant information about the tip such as its dielectric properties in form of the permittivity, $\varepsilon_{\text{probe}}$ [47]. Following the definition in Eq. (1.1), the full expression for the effective polarisability then becomes [47, 51],

$$\alpha_{\text{eff}} = \frac{p_{\text{eff}}}{E_0} = 2LW_0^2 \left(\gamma_0 - 1\right) \left(1 + \frac{1}{2} \frac{\beta f_0}{1 - \beta f_1}\right), \tag{1.13}$$

where the field enhancement factor γ_0 is given as,

$$\gamma_0 = \frac{(\varepsilon_{\text{probe}} - 1)\left(2\sqrt{1-\frac{R}{L}} + \frac{R}{L}\ln\frac{1-\sqrt{1-\frac{R}{L}}}{1+\sqrt{1-\frac{R}{L}}}\right)}{2\sqrt{1-\frac{R}{L}}\left(1-\varepsilon_{\text{probe}}\frac{R}{L}\right) - \frac{R}{L}\left(\varepsilon_{\text{probe}}-1\right)\ln\frac{1-\sqrt{1-\frac{R}{L}}}{1+\sqrt{1-\frac{R}{L}}}} + 1. \tag{1.14}$$

The effective polarisability from Eq. (1.13) can be divided into two parts; the first which is related to the tip shape and parameters, and last which is related to the contrast between measurements and materials known as the contrast factor, η. The part related to the tip shape and properties does not depend on surface properties and in many cases, the permittivity of the probe is assumed to be $\varepsilon_{\text{probe}} = -\infty$ since many probes have a metallic coating. Thus, in most cases, this factor is eliminated by simple normalisation. Due to this fact, we can estimate the effective polarisability as,

$$\alpha_{\text{eff}} \propto \eta = 1 + \frac{1}{2}\frac{\beta f_0}{1-\beta f_1}, \tag{1.15}$$

which describes the contrast between measurements in the system and thus the near-field interactions.

1.3 Layered structures extension

Up until now, both in the PDM and the FDM, the scenario we have been describing is that of having to semi-infinite half-planes of dielectrics; one being the air the probe is situated in, and the other being the surface material which the probe interacts with. This scenario is what is represented in Figure 1.1. When studying simple bulk materials this approximation is fairly accurate, but most samples are made of different layers of different materials, and thus this approximation is no longer sufficient. A representation of such a sample construction is shown in Figure 1.2.

Hauer *et al.* proposed a method of expanding the FDM to account for a single layer in between two semi-infinite half-spaces, which could in principle be expanded to any number of layers [52]. This expansion is encompassed in a modification of the near-field reflection coefficient, β_X and a modification to the geometric functions to account for the placement of the monopole charges, given by,

$$f_{0,1} = \left(g - \frac{R + 2H + X_{0,1}}{2L}\right)\frac{\ln\frac{4L}{R+4H+2X_{0,1}}}{\ln\frac{4L}{R}}. \tag{1.16}$$

Using these two modifications, one can describe a layered dielectric structure. However, since this method requires the evaluation of the surface potential in the presence of a tip and its derivatives, it can become quite complex.

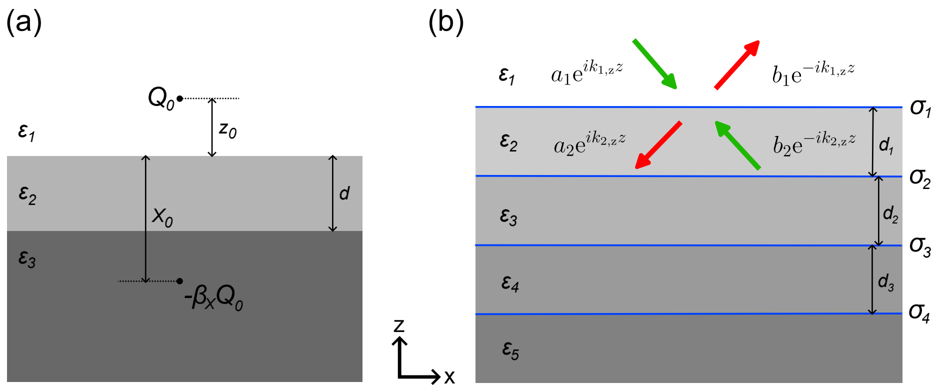

Figure 1.2. (a) Layered model extension for the FDM where the altered positions of the point charges are described and (b) illustration of layered structure described by the transfer matrix method with the incident and reflected beams defined in the figure. Adapted from [52] and [53].

1.3.1 Transfer matrix formalism

Later, Wirth *et al.*, proposed a method of using a transfer matrix method, first described by Zhan *et al.* [53], to modify the near-field reflection coefficient to describe the case when having an infinitely thin conductive layer between two dielectrics [54].

The transmission of the light between the two dielectrics can be described by the following field coefficient relation,

$$\begin{bmatrix} a_i \\ b_i \end{bmatrix} = D_{i,j} \begin{bmatrix} a_j \\ b_j \end{bmatrix} \tag{1.17}$$

where $D_{i,j}$ is the transmission matrix that describes how the light is refracted at the interface, given as,

$$D_{i,j} = \frac{1}{2} \begin{bmatrix} 1+\eta+\xi & 1-\eta-\xi \\ 1-\eta+\xi & 1+\eta-\xi \end{bmatrix} \tag{1.18}$$

with the parameters,

$$\eta = \frac{\varepsilon_i k_{j,\mathrm{z}}}{\varepsilon_j k_{i,\mathrm{z}}}, \tag{1.19}$$

$$\xi = \frac{\sigma_{\mathrm{s}} k_{j,\mathrm{z}}}{\varepsilon_0 \varepsilon_j \omega}. \tag{1.20}$$

Here, $k_{i,\mathrm{z}} = \sqrt{\varepsilon_i \frac{\omega^2}{c^2} - q^2}$ is the wavevector perpendicular to the surface, as indicated by the coordinates in Figure 1.2, with q being the in-plane momentum, and σ_s is the conductivity of the infinitely thin conductive layer at the interface between the two dielectrics ε_i and ε_j. Eqs. (1.19) and (1.20) describes the case for perpendicularly polarised light, which is the dominant polarisation in the FDM. It is noteworthy to observe the appearance of the light's frequency, , in the denominator in Eq. (1.20).

If multiple layers are present in the structure, a propagation term is needed to describe how the light propagates through the given medium. This propagation matrix is given as,

$$P(d) = \begin{bmatrix} \mathrm{e}^{-ik_\mathrm{z}d} & 0 \\ 0 & \mathrm{e}^{ik_\mathrm{z}d} \end{bmatrix}, \tag{1.21}$$

where d is the thickness of the medium the light propagates through.

The full transmission through multiple layers can then be determined by the transfer matrix, $\mathcal{M}$, which is calculated as matrix product of all propagation and transmission matrices,

$$\mathcal{M} = D_{1,2}P(d_2)D_{2,3}P(d_3)\cdots P(d_{N-1})D_{N-1,N}. \tag{1.22}$$

The reflection coefficient can be found from the elements of the transfer matrix defined in Eq. (1.17) as [55],

$$\beta = \frac{\mathcal{M}_{21}}{\mathcal{M}_{11}}. \tag{1.23}$$

Thus, the total reflection coefficient of any number of layers with any thickness can be determined through Eqs. (1.22) and (1.23), and the new total reflection coefficient replaces the reflection coefficient in Eq. (1.15).

If we look at the case when having a single infinitely thin conductive layer in between two dielectrics, which could be the case when having a graphene layer on silicon situated in ambient air, then the transfer matrix simply becomes $\mathcal{M} = D_{1,2}$. Thus, the reflection coefficient can be calculated as,

$$\beta = \frac{D_{1,2}^{21}}{D_{1,2}^{11}} = \frac{\varepsilon_2 - \varepsilon_1 \frac{k_{2,\mathrm{z}}}{k_{1,\mathrm{z}}} + \frac{\sigma_s k_{2,\mathrm{z}}}{\varepsilon_0 \omega}}{\varepsilon_2 + \varepsilon_1 \frac{k_{2,\mathrm{z}}}{k_{1,\mathrm{z}}} + \frac{\sigma_s k_{2,\mathrm{z}}}{\varepsilon_0 \omega}}. \tag{1.24}$$

In s-SNOM, the tip scatters the light to extremely high in-plane momenta, which opens the possibilities of many interesting physical phenomena. A general rule of thumb for how far the tip scatters the light is estimated simply as the inverse of the tip apex radius, $q \sim 1/R$.

In a more general form, the tip will scatter the light to various different in-plane momenta. This scattering will have some distribution with a peak momentum, where the rule of thumb approximates this peak momentum. The distribution for a layer in between two dielectrics following the FDM, can be found as [56, 57],

$$W_q(q) = q\mathrm{e}^{-2qR}\mathrm{e}^{q(H+R)}. \tag{1.25}$$

A similar expression can be found within the framework of the PDM [58, 59]. The coupled weight functions and their distribution can be seen in Figure 1.3, along with the approximation of $q \sim 1/R$. Although the approximation generally slightly overshoots, it remains a decent approximation for the dominant in-plane momentum.

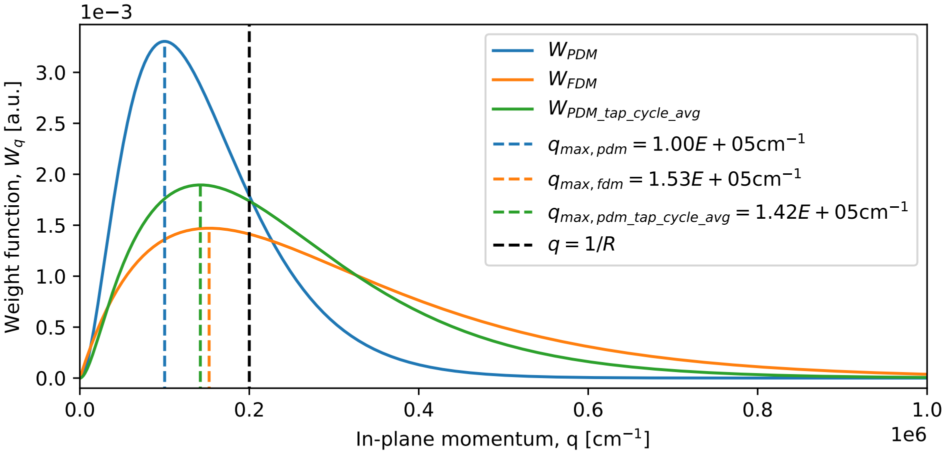

Figure 1.3. Weighted distribution of in-plane momenta q for a tip radius of $R = 50$ nm as predicited by the FDM and PDM. The green curve shows the distribution from the FDM when averaged over one tapping cycle with a tapping amplitude of $A = 100$ nm. The dashed vertical lines shows the maximum given in the legend and the black dashed line shows the $1/R$ estimation.

As seen in Figure 1.3, the light is scattered to extremely high in-plane values. Comparing these values to the wavenumber of the light, which for 1 THz in free-space is in the order of $k \approx 10^2\mathrm{cm}^{-1}$, we see that the in-plane momentum is the dominating term in the wavevector $k_{i,z}$. Thus, using $q^2 \gg \frac{\omega^2}{c^2}$, which is the quasi-electrostatic approximation, Eq. (1.24) simplifies to,

$$\beta = \frac{\varepsilon_2 - \varepsilon_1 + \frac{i\sigma_s q}{\varepsilon_0 \omega}}{\varepsilon_2 + \varepsilon_1 + \frac{i\sigma_s q}{\varepsilon_0 \omega}}. \tag{1.26}$$

If the infinitely thin layer in between the two surrounding dielectrics is assumed to have no conductivity, Eq. (1.26) is reduced to the electrostatic reflection coefficient in Eq. (1.3).

In this thesis, the transfer matrix method will be the main model used for analysis of structured samples.

1.4 Detection of the scattered field

The light scattered from the tip-sample interaction was previously mentioned to be given as,

$$\sigma = \frac{E_{\text{sca}}}{E_{\text{inc}}} = (1 + r_{\text{s}})^2 \, \alpha_{\text{eff}}, \tag{1.27}$$

where, we in this case have defined the response in terms of the scattering coefficient, σ.

The effective polarisability, α_{eff}, is a function of the distance between the tip and sample, H, as seen in Eqs. (1.4) and (1.8). The tip inside the AFM is oscillating with a motion described by,

$$H(t) = h_0 + \frac{1}{2}A(1 + \cos(\Omega t)), \tag{1.28}$$

with A being known as the tapping amplitude, h_0 is the minimum distance between the tip and sample, and Ω is the tapping frequency of the tip. Due to the interactions between the tip and surface underneath, the motion becomes highly non-linear and as a result higher harmonics of the tip frequency are generated. This motion modulates the near-field signal, since it is height dependent, and the near-field signal can then be found by demodulating the signal at the tapping frequency Ω. The detected signal is a combination of the near-field interactions between the tip and sample, but also contains far-field contributions, such as far-field reflection and scattering from the sample, which is not interacting with tip. However, demodulating the signal at higher harmonics causes the background contributions, which do not partake in the near-field interactions, to be suppressed [18, 19, 60, 61]. In Figure 1.4(a) we see the time-domain signal of the effective polarisability, which constitutes the mechanism for the contrast observed between measurements and material characteristics. Taking the Fourier transform decomposes the non-linear signal into its Fourier components, which is depicted in Figure 1.4(b). From Figure 1.4(b) it is clear that with increasing harmonic order, the signal simultaneously decreases. Thus, a compromise between increased near-field to far-field ratio and signal strength is needed. This usually results in either the 2nd or 3rd order to be chosen. This will be discussed more in practice in chapter 2.

To save computational power and time, instead of computing the whole Fourier transform each time, one can compute a the response at a single harmonic $\Omega_m = m\Omega$ by computing the mth Fourier component as [48],

$$\sigma_m(\beta) = \int_0^T \sigma(\beta, H(t))\, \mathrm{e}^{i\Omega_m t} \mathrm{d}t = (1 + r_{\text{s}})^2 \, \alpha_{\text{eff},m}, \tag{1.29}$$

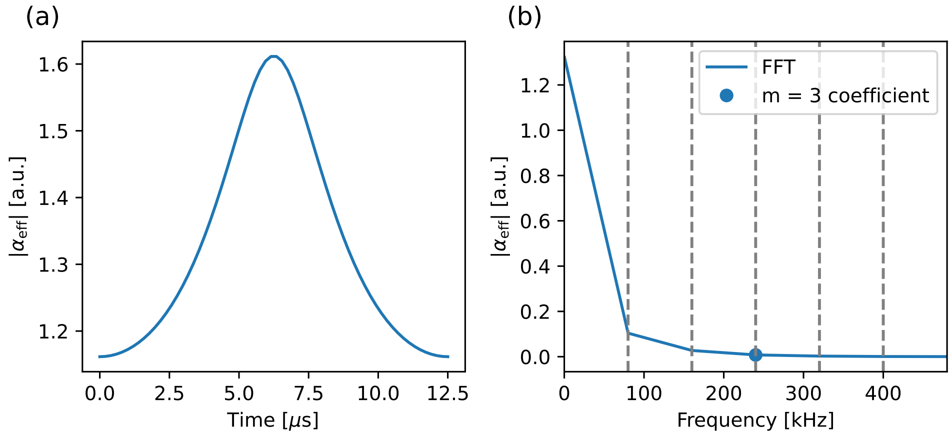

Figure 1.4. (a) Example of a time domain trace of the effective polarisability for a single cycle and (b) the corresponding spectrum where the solid line is the Fourier transform of the time trace and single point is the value calculated through Eq. (1.29) at $m = 3$. The vertical dashed lines corresponds to the positions of harmonics $m = 1, 2, 3, 4, 5$.

where T defines the tapping period of the tip. This computing of the signal is depicted in Figure 1.4(b) for the $m = 3$ harmonic.

With being able to recreate the effective polarisability α_{eff}, we can compute what is known as approach (or retract) curves, which give an indication of how quickly the near-field signal decays in the z-direction. We do this by calculating the effective polarisability at various heights and then plot the demodulated amplitude as a function of the height. This is shown in Figure 1.5(b).

From the approach curves, the $1/e$ decay length give an indication of the spatial resolution achievable in the current configuration. This is the spatial resolution in the out-of-plane direction, i.e., z-direction, however, since the PDM assumes the tip as a sphere, the out-of-plane resolution would be comparable to the in-plane resolution. This is not entirely the case with the FDM, however, it remains a reasonable approximation.

1.5 FEM simulation techniques

Using the developed models outlined above describes the near-field interactions between a sharp tip in close proximity with a surface, illuminated by a light source, however, the models utilises approximations and thus, might not encapsulate all aspects of the near-field interactions. Another approach to simulate the response of

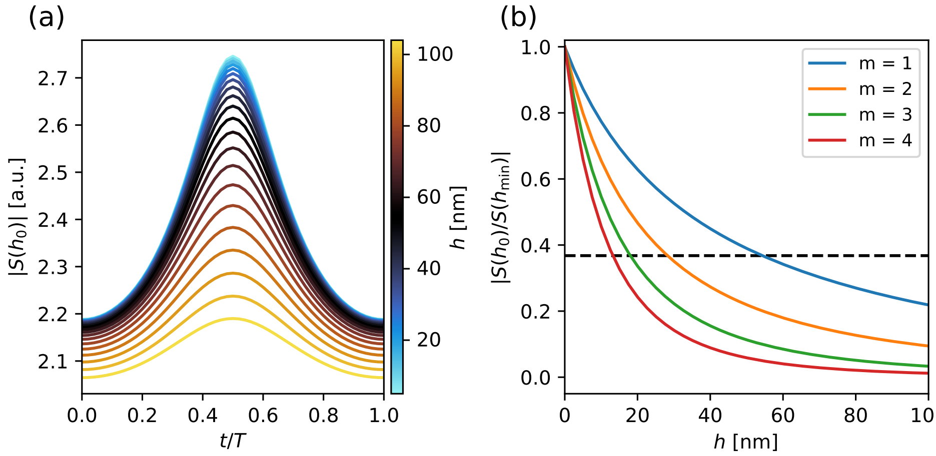

Figure 1.5. (a) Effective polarisability at different height for a single tapping cycle. (b) Calculated approach curves for the $m = 1, 2, 3, 4$ harmonics of the effective polarisability. The dashed horizontal line indicates the $1/e$ decay length, which is an indicator of the spatial resolution [62].

these interactions is to perform finite-element simulations (FEM), which simulate the response based on pure electromagnetic interactions. Tremendous efforts has been put into studying the near-field interactions through numerical methods both in 2D [49, 63, 64] and 3D [65, 66] in all aspects of the technique.

In this thesis we use the commercial software COMSOL Multiphysics to simulate the near-fields interactions arising from the scattering of THz fields off an oscillating AFM tip. Following the approach by Conrad *et al.* we simplify the simulation domain to 2D [63]. The reason behind this is rooted in the long wavelength of the THz fields. To fully capture the THz fields we would as a minimum need a spatial domain size of around twice the wavelength, which at 1 THz would correspond to a $600 \times 600 \mu\text{m}^2$ domain. The radius of the tip we use in our simulation is typically $R = 50$ nm. Thus, to finely mesh the area around and under the tip, we would need a meshing grid with distances between the cells on the nanometre scale, while the whole domain is almost on the millimetre scale. For 2D this is possible with an adaptive meshing, which is shown in Figure 1.6, yielding $\sim 10^6$ cells. Extending this to a third spatial dimension would exponentially increase the amount of cells and therefore the computational demand, increasing the difficulty of performing parameter sweeps. Thus we limit our simulations to 2D.

Conrad *et al.* make use of a two-step method in which they simulate the domain without the presence of the tip and afterwards simulate the domain with the tip using the resulting fields. However, we opt to use a one-step approach where we simulate the domain as a whole, since this resembles the physical experiment the most. We

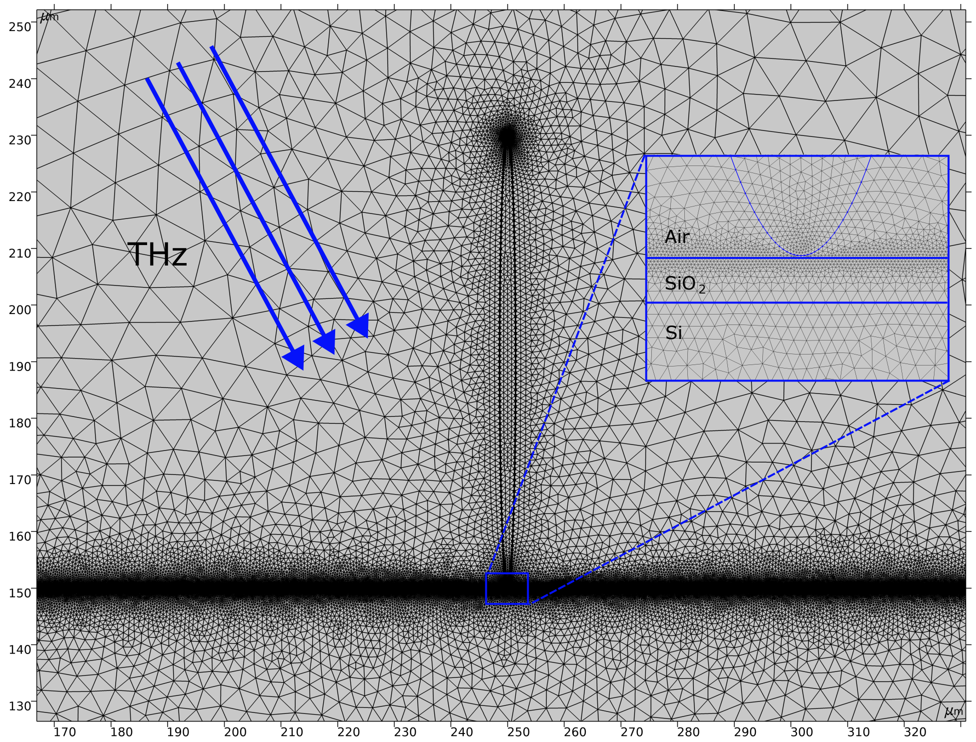

Figure 1.6. Example of the meshing of simulation domain showcasing the finely meshed interfaces and tips ends. The inset show a zoom in of the tip in close proximity with a SiO_2/Si surface.

calculate the scattered field as the surface integral of the out-of-plane electric field over the tip, $\int_{\text{tip}} E_y \mathrm{d}l$ [63].

We simulate half of the tapping cycle (Eq. (1.28)) and mirror the result to obtain a full tapping cycle. Then, in post processing we perform the demodulation into the harmonic components of the tip oscillation frequency, identical to Figure 1.4. All simulations are performed using a plane wave as representation of the incoming light, thus to perform broadband simulation, a parameter sweep of the frequency is needed. With this, we can compare our experimental results to FEM predictions of a similar setup, which will aid in our understanding and interpretation of the near-field interactions.

CHAPTER 2

THz-SNOM in practice

This chapter is dedicated to practical learning, focusing on how to extract and process data from the system. We will also discuss common measurement practices, including purging, approach curves, and typical operational values. Consequently, this chapter aims to assist future operators of the system.

2.1 Retrieval of terahertz pulse

When performing a full sampling of the THz waveform with the system, we obtain both an amplitude and a phase signal, which are shown in Figure 2.1(a) and (b), respectively. As we can see, at first glance this does not resemble a typical THz pulse obtained by standard electro-optic (EO) sampling or measured by a photoconductive

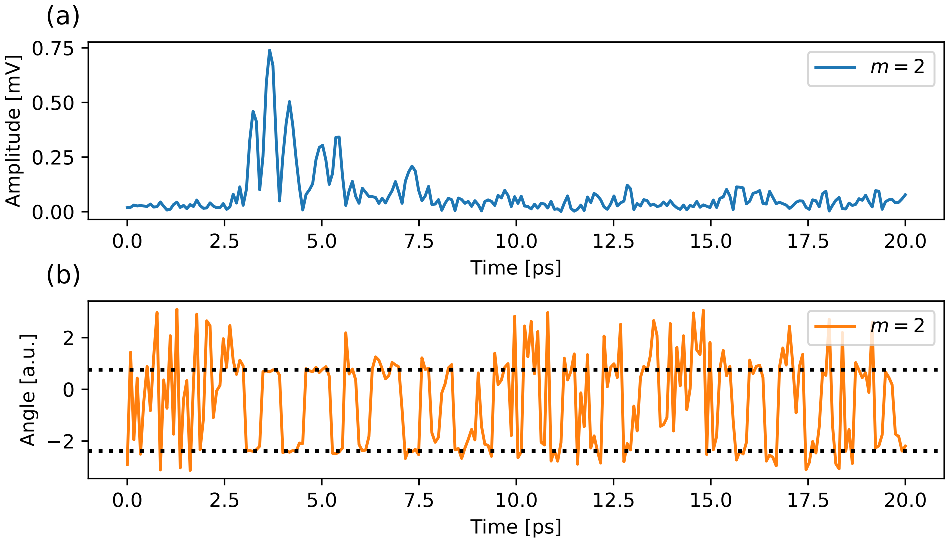

Figure 2.1. (a) Amplitude and (b) phase signal obtained by performing a full sampling of the THz waveform in the near-field.

antenna (PCA) in the far-field. We observe that the system provides the absolute values of the amplitude and a corresponding phase, which oscillates by π with an offset from zero. Thus, we need to convert the amplitude and phase into an electric field, however, first we must ensure that the phase oscillates from 0 to π by shifting the phase by the phase offset φ_{offset}. The resulting phase along with an unchanged amplitude is shown in Figure 2.2.

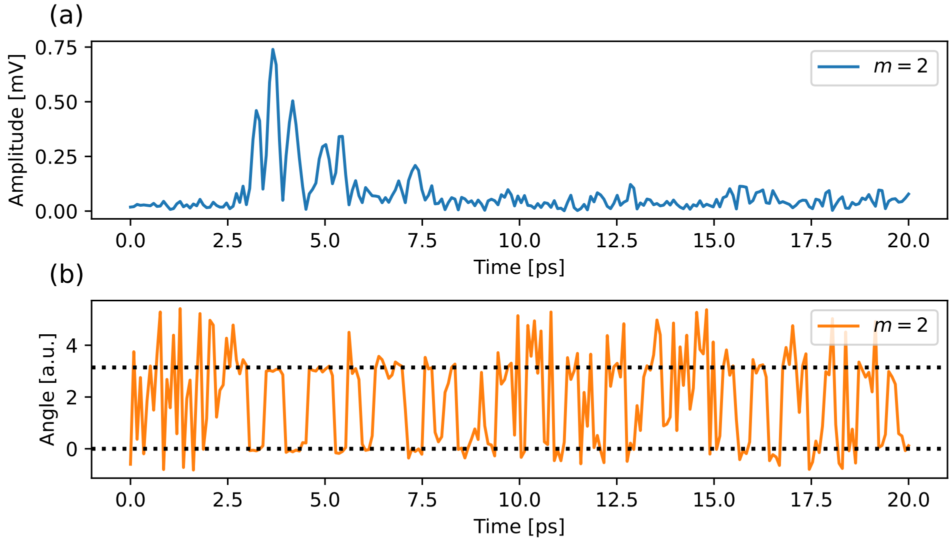

Figure 2.2. (a) Amplitude and (b) phase from a full sampling of the THz waveform in the near-field, where the phase off has been corrected to ensure it oscillates between 0 and π.

In practice, this is done by defining the phase offset to be the phase value at the peak in the time-domain, and then shifting the whole phase trace by that singular offset. The purpose of shifting the phase to oscillate between 0 and π is to ensure the resulting electric field remains a real quantity, devoid of any imaginary part. With the phase offset defined and accounted for, we can convert the amplitude and phase into an electric field through,

$$E(t) = Ae^{-i(\varphi+\varphi_{\text{offset}})t}. \tag{2.1}$$

The resulting electric field is shown in Figure 2.3 for the $m = 2$ harmonic, where we observe a near-zero imaginary part across the whole time window.

2.1.1 Comparison of harmonic orders

As mentioned earlier, by increasing the harmonic order we are able to suppress the background contribution to the signal. However, as visible from Figure 1.4(b), we

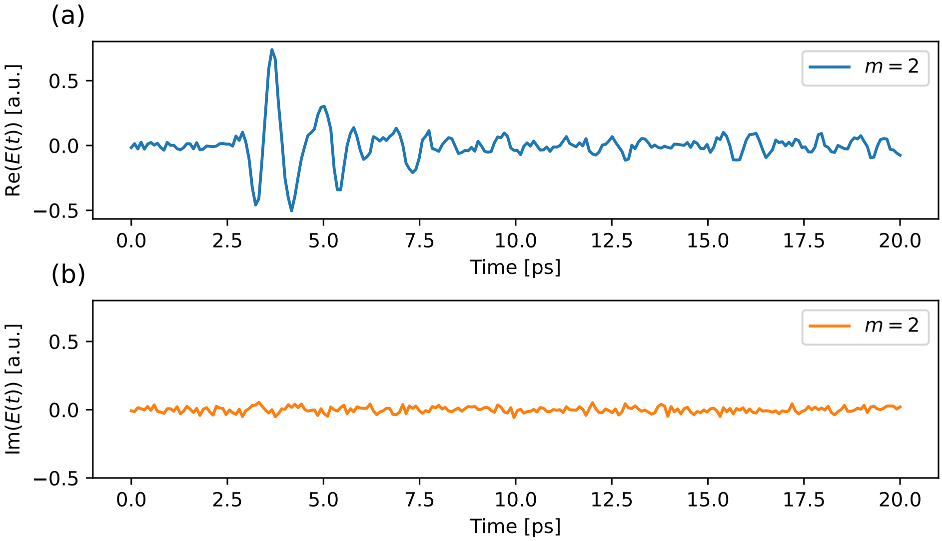

Figure 2.3. (a) Real and (b) imaginary part of the reconstructed electric field from the amplitude and phase signals.

observe that increasing the harmonic order also decreases the signal strength. An example of this shown for a full time trace of the THz pulse is shown in Figure 2.4 for the different harmonics. In this figure, we clearly observe that in the $m = 2$ harmonic order, we are able to resolve the main pulse as well as the after-ringing and even what appears to be a second reflection. However, in the $m = 5$ harmonic order, we

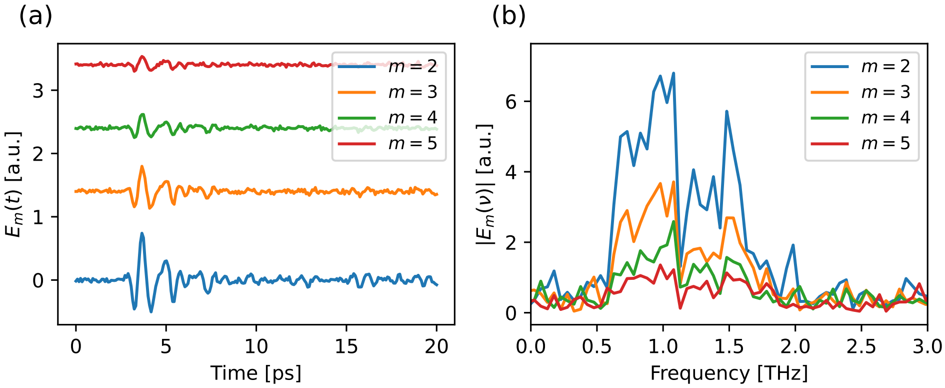

Figure 2.4. (a) THz waveform at harmonics $m = 2, 3, 4, 5$, where the time traces have been shifted in the y-direction for better representation, and (b) corresponding spectra.

are barely able to distinguish the main part of the pulse from the noise floor. Based on this, it is therefore common practice to use either the $m = 2$ or $m = 3$ harmonic order depending on the signal-to-noise ratio (SNR) in the measurement.

2.1.2 Increase signal-to-noise ratio: Tip denting

A common way to increase the SNR with a given tip, is to increase the scattering cross-section of the tip. This will increase the area of which the light is scattered off, however, by increasing the the scattering cross-section the spatial resolution will decrease. This is especially the case when working with visible or near-infrared light, however for THz radiation, this trade-of is not as detrimental but still significant [67]. Practically, this can be achieved by slightly perturbing the optical table while the tip is in contact with the sample. This forces the tip to make physical contact with the surface, thereby denting or bending it and increasing the scattering cross-section. Figure 2.5 shows scanning electron microscope (SEM) images of a brand new tip, which has been purchased to have sub-40 nm apex tip radius in Figure 2.5(a), and a tip after denting it in Figure 2.5(b). It is important to note, that the tip in the two SEM images is not the same, but an example of how a tip looks before and after denting. We notice in Figure 2.5(b) that the dented tip has gained a kink and one can speculate whether such a bend aids in maintaining the spatial resolution.

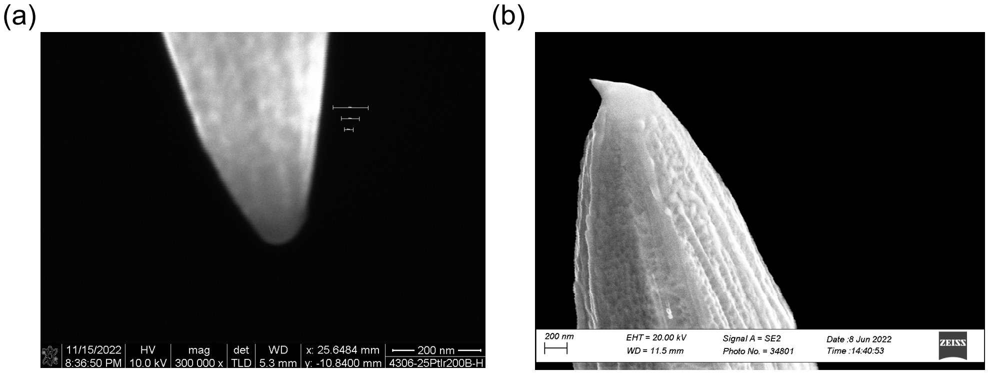

Figure 2.5. Scanning electron microscope (SEM) images of PtIr probes for (a) brand new and (b) after denting. The scale bar is both images is 200 nm. The tip in (a) and (b) are not the same, but a representative of before and after denting.

The process of denting the tip this way is random by nature, and therefore some dented tips may yield excellent SNR while also maintaining an great spatial resolution, whereas other tips may only worsen the spatial resolution without an increase in SNR. Thus, when denting a tip, it is important to check the resulting approach curves, since they can be correlated to the spatial resolution achievable by the tip. Denting a tip usually leads to an increase in peak intensity of around a factor of 2 in the $m = 2$ harmonic signal for a good tip.

2.2 Approach curves

In this section, we shall see a typical set of approach curves and how to analyse them. When performing an approach curve scan with the system, a typical result will look similar to what is shown in Figure 2.6.

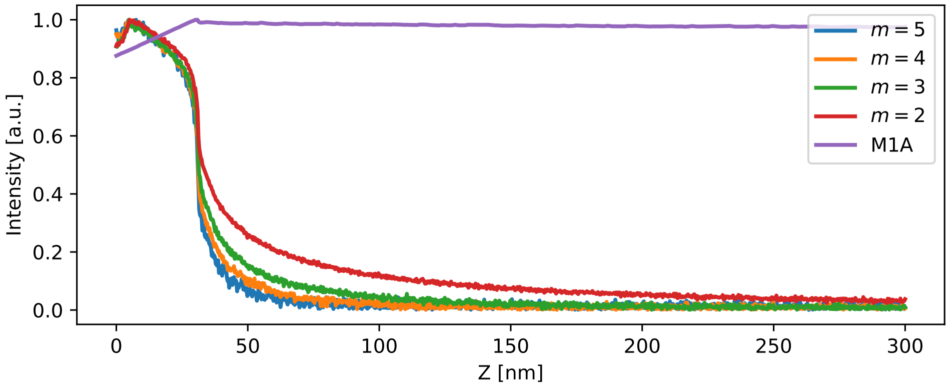

Figure 2.6. Raw approach curves as extracted from the system for the $m = 2, 3, 4, 5$ harmonic as well as the first order tapping amplitude M1A.

In this figure, we have normalised each harmonic to its maximum as well as for the tapping amplitude of the cantilever, denoted M1A. We observe that, as we retract the tip, the tapping amplitude rises linearly until a certain threshold, beyond which it attains its free-standing tapping amplitude. This position is often identifiable by a kink in the curve. Consequently, we define the contact point of the system as 90% of the free-standing tapping amplitude, as visible in Figure 2.6. For the optical amplitudes, we note a slight decrease at the beginning of the retraction. Upon reaching the free-standing tapping amplitude — indicating the tip is no longer in contact with the sample — there is a rapid decrease in the signal. We use this decay length to approximate the spatial resolution.

Figure 2.7 shows the same approach curves as Figure 2.6, however, here we have shifted the axis to the point of not being in contact, i.e., just after the kink in the tapping amplitude. We then approximate the spatial resolution as being the 1/e decay length [62], which in this example is around 25-30 nm for the $m = 2$ harmonic and approximately 15-20 nm for the $m = 3$, showing excellent confinement. One can then fit the approach curves for each harmonic with a double exponential function, which is shown in Figure 2.7 by the black, dotted curves.

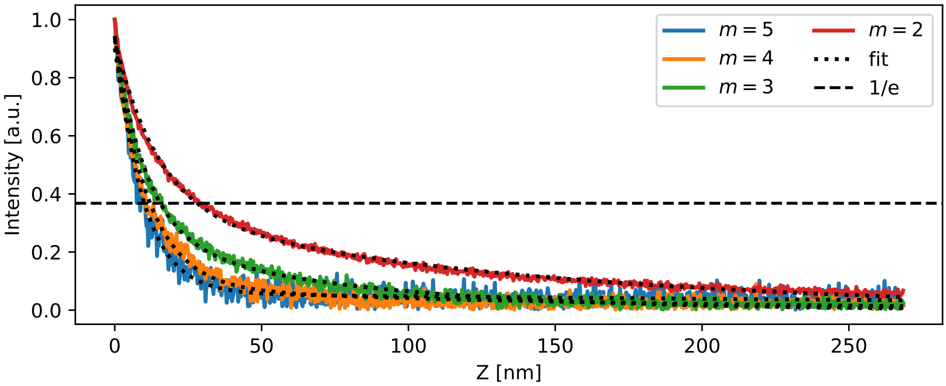

Figure 2.7. Approach curves for the $m = 2, 3, 4, 5$ harmonic fitted with a double exponential function shown as the black dotted curve. The horizontal, black dashed line indicates the 1/e decay length.

The position at which the tip goes out of contact with the sample, depicted by the kink in the tapping amplitude in Figure 2.6, depends on the value of the tapping amplitude. If a large tapping amplitude is used, e.g., 200 nm, then the plateau of the optical signal in the beginning will be extended, before an exponential decay starts. Furthermore, using a large tapping amplitude may also worsen the spatial resolution predicted by the approach curves, in exchange for more signal. For this reason, a typical range of tapping amplitudes for our measurements are around 100-150 nm when in contact.

2.3 Purging with N_2

The THz spectrum is heavily dominated by water absorption lines which are visible in the far-field spectrum of the system shown in Figure 0.5(b) with significant absorption at 1.1 THz, 1.7 THz, and 2.3 THz. Since in the near-field our spectral bandwidth is limited, ranging from 0.5 THz to a maximum of approximately 2.5 THz, avoiding these water absorption lines would significantly increase the effective bandwidth of our system. We achieve this by enclosing the system in a purge box and replacing the ambient air with a constant flow of nitrogen N_2. As the microscope is contained within its own housing, the airflow will not affect the system's stability. Over time, the nitrogen will gradually replace the ambient air through the housing's openings. The effects of purging the system are shown in Figure 2.8.

In this figure, we observe a significant impact of the purged environment not only in the spectrum but also in the time-domain. In the time-domain in Figure 2.8(a), we observe a significant increase in peak intensity as well as a slight shift in position.

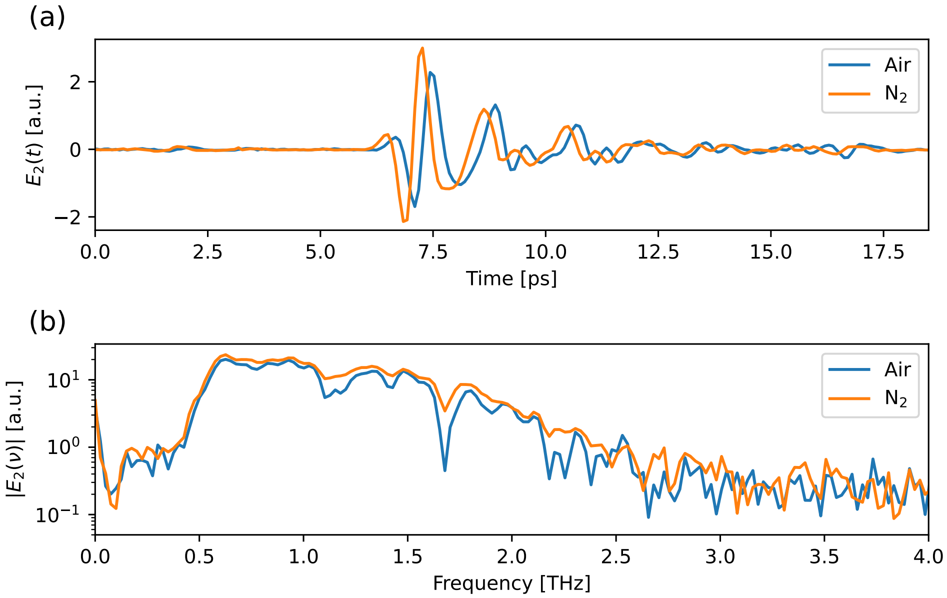

Figure 2.8. (a) Time-domain trace of the $m = 2$ harmonic order THz pulse in ambient air and a N_2 purged environment and (b) corresponding spectra. After obtaining the ambient air time trace, the system was purged for an hour to ensure a high percentage of N_2, before obtaining the purged time trace.

Since the main operation mode of the system is performing scans with the delay stage parked at the peak intensity in the time-domain, the so called *whitelight* scan, purging the system results in an increase in SNR in this scanning mode. Furthermore, in Figure 2.8(b), we observe that the water absorption lines at 1.1 THz and 2.3 THz have almost completely been removed, and the impact of the 1.7 THz absorption line has been significantly lessened. Overall, purging the system increases our effective bandwidth and our SNR in whitelight mode.

In this thesis, all the proceeding results are obtained in a purged environment unless otherwise stated.

Part I

Dielectrics: Semiconductors

CHAPTER 3

Molybdenum disulfide nanoribbons

Molybdenum disulfide (MoS_2) is, among other transition metal dichalcogenides (TMDs), a promising candidate for future devices due to its relatively high carrier mobility, large refractive index, mechanical flexibility, and advances in growth on a large-scale basis [68–71]. The potential use-case for TMDs such as MoS_2, WSe_2, WS_2, and more, range from field-effect transistors [72–74] and electrocatalytic hydrogen evolution reaction (HER) [75–77] to photovoltaic devices [78, 79] and ultrafast photodetectors [80]. This is due to their intrinsic nature which typically exhibit a bandgap in the range of 1-2 eV, with an indirect-to-direct band gap crossover when reducing the thickness from bulk down to a few layers [81].

Nanostructuring TMDs into, e.g., nanoribbons opens up even more possibilities within device fabrication as it allows for efficient light-matter interactions [82–84]. Thus, studying these nanostructured materials and their optical and electrical properties is of utmost importance for further advances within material engineering.

3.1 Material characteristics

The layered TMD, MoS_2, is a semiconductor with an indirect bandgap of 1.2 eV in bulk, however, this bandgap transits to a direct bandgap, with a bandgap of 1.8 eV when lowering the dimensions to 2D. Not only does a bandgap transition from indirect-to-direct occur when lowering the dimensions, but the material properties can also change dramatically [76, 85–87]. The direct bandgap of monolayer MoS_2 can be widely tuned by mechanical strain, not only lowering the bandgap energy, but also causing a direct-to-indirect bandgap transition [88–90]. These properties of MoS_2 is the reason behind its emergence and immense popularity as building block for future devices. The ability to tune the bandgap makes MoS_2 an ideal candidate for photovoltaic devices and thus, being able to characterise the optical and electrical properties of both monolayer and few-layer MoS_2 is a necessity for further advances in device fabrication. One of the most common techniques for characterising the properties of MoS_2 is (angle-dependent) Raman spectroscopy, which reveals information pertaining the crystal symmetry, stacking order, and material strain presence [91, 92].

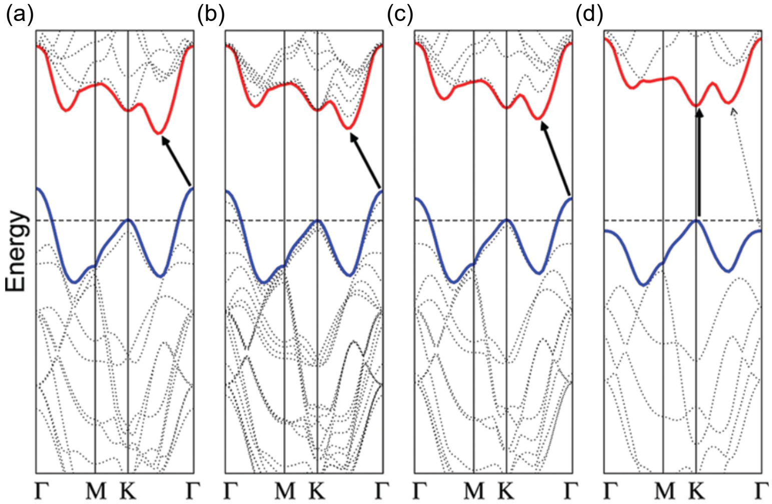

Figure 3.1. Band structure calculated through density functional theory of (a) bulk MoS_2, (b) four layers of MoS_2, (c) bi-layer of MoS_2, and (d) monolayer of MoS_2. When lowering the dimensions of MoS_2, the transition from indirect-to-direct bandgap can be seen. Reproduced from [87].

Techniques such as ellipsometry [93] and photoluminescence [94, 95] are also used as characterisation methods, but all these methods are severely limited in the achievable spatial resolution. As the demand for miniaturisation in devices continues to escalate, it is imperative to have a methodology capable of determining the optical and electrical properties at increasingly small length scales.

3.1.1 Terahertz properties

A useful technique for studying a material's optical and electrical properties is THz-TDS, from which one can extract a frequency resolved complex dielectric function and conductivity through the application of, e.g., the Drude-model [30].

Yan *et al.* performed THz-TDS and ellipsometry on a bulk (10 mm × 10 mm × 90 μm) crystal of MoS_2 and showed that the real part of the permittivity slightly increases with higher frequency in the THz region, while no distinct features are present [96]. This fact is illustrated in Figure 3.2. In their work, they find the properties of the MoS_2 crystal to be described by the Drude model and their specific sample to have a carrier concentration of $N = 3 \cdot 10^{15} \mathrm{cm}^{-3}$. Thus, we can describe the complex permittivity of MoS_2 with a Drude-Lorentz model, with resonance frequency of $\omega_0 = 0$, resulting in a Drude response, given as [96–98],

$$\varepsilon(\omega) = \varepsilon_\infty - \frac{\omega_\mathrm{p}^2}{\omega^2 + i\omega\Gamma}, \tag{3.1}$$

with ε_∞ being the permittivity in the high-frequency limit, Γ being the carrier damping rate, and $\omega_\mathrm{p} = \sqrt{\frac{ne^2}{\varepsilon_0 m^*}}$ being the plasma frequency, where n is the carrier concentration, e is the elemental charge, ε_0 is the free-space permittivity, and m^* is the effective mass.

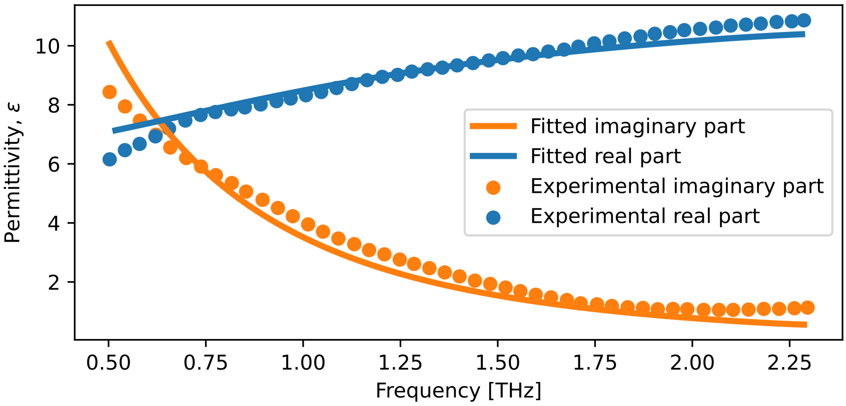

Figure 3.2. Real and imaginary part of the permittivity of bulk MoS_2 extracted from far-field THz-TDS and fitted with a Drude-Lorentz model. Reproduced from [96].

The value of the high-frequency limit permittivity of MoS_2 varies significantly with experimentally reported values being $\varepsilon_\infty = 4.2$ [96], $\varepsilon_\infty = 4.4$ [99, 100], $\varepsilon_\infty = 11.45$ [98], and $\varepsilon_\infty = 12.15$ [101]. One report even justifies using $\varepsilon_\infty = 1$, assuming the material to be conductive, thus following the Drude response of metals [97]. The techniques used to extract these values are mainly ellipsometry and THz measurements, with the latter yielding the higher extractions values. This, at first, slight discrepancy is most likely due to the fact that MoS_2 has a significant amount of resonances when approaching the infrared and visible regime from the low-frequency regime, thus effectively lowering the optimal fit parameter for ε_∞ within the given probing range. The reported values for the effective mass also ranges significantly from $m^* = 0.32m_0$ to $m^* = 0.60m_0$ [96,99,100,102,103], with m_0 being the mass of an electron.

The value of the permittivity within the THz regime depends highly on carrier concentration of the material, which is evident from Eq. (3.1). Figure 3.3 shows the permittivity within a frequency range of 0.1 THz to 3 THz for a number of different carrier concentration ranging from a low doped concentration of $n = 1 \cdot 10^{16}\mathrm{cm}^{-3}$ to a relative high concentration of $n = 5 \cdot 10^{17}\mathrm{cm}^{-3}$. Shen *et al.* even reported chemical vapour deposition (CVD) MoS_2 films with a carrier concentration of $n = 2.2 \cdot 10^{18}\mathrm{cm}^{-3}$, which corresponds to a extremely highly doped state [99]. From Figure 3.3 we observe that with increasing carrier concentration, in the low frequency range, the material properties become similar to those of metals.

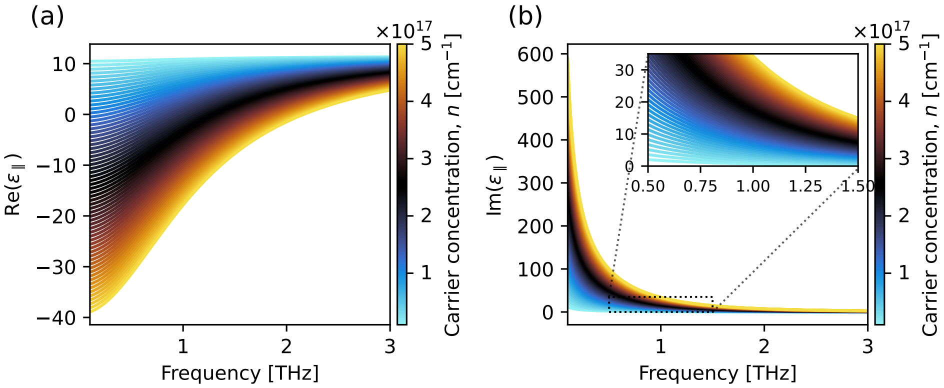

Figure 3.3. The impact of the carrier concentration on the complex permittivity of MoS_2 for (a) the real part and (b) the imaginary part, using a Drude-Lorentz model.

3.2 Molybdenum disulfide nanoribbon samples

In this section, we will introduce specific samples of MoS_2 nanoribbons, detailing their characteristics. These include their Raman response, which provides information about crystallinity and layering (monolayer or multilayer), and measurements from scanning electron microscopy (SEM) and atomic force microscopy (AFM) to determine their geometric dimensions. Additionally, a brief description of the nanoribbons' growth process will be provided for completeness. These samples were fabricated by our collaborators at DTU Electro in the Photovoltaic Materials and Systems group led by Dr. Stela Canulescu. For a more detailed explanation of the specific growth and nature regarding these nanoribbons, please refer to the work by Ghimire *et al.* [86] and Miakota *et al.* [104].

3.2.1 Growth process

The MoS_2 nanoribbons were synthesised in a two-step process in which ultra-thin oxide films of MoO_3 grown by pulsed laser deposition (PLD) were sulfurised on the second step in the presence of a NaF layer and the details of the process can be found in described in [86, 104]. The synthesis technique of MoS_2 nanoribbons used is similar to that described by Li et.al. [82] and shares many similar ideas on liquid phase creation and vapor-liquid-solid phase reaction. Briefly, the growth process evolves via the formation of the Na–Mo–O liquid phase, which mediates the formation of MoS_2 multilayer nanoribbons in a sulfur-rich environment [82, 86, 104]. MoS_2 seed crystals are formed in the liquid phase and can diffuse and merge into larger multilayer crystals. The nanoribbon grows unidirectional from the liquid phase droplet and follows a path of favourable surface energy. During the growth of the nanoribbon it may merge with other droplets facilitating monolayer growth around the edges of the nanoribbon. Figure 3.4 shows the growth steps, where the MoO_x precursors are created through PLD and deposited on a sapphire substrate before a 20 nm NaF layer is deposited using thermal evaporation. Lastly, the MoO_x precursor is placed in a sulfur rich environment at high temperature which facilitates the growth process.

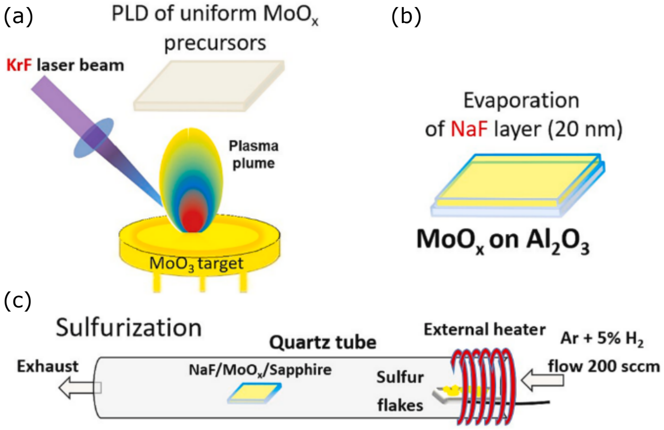

Figure 3.4. Graphical depiction of synthesising MoS_2 nanoribbons based on a two-step process including pulsed laser deposition (PLD). (a) Laser ablation of a MoO_x thin film with a 248 nm KrF laser on a sapphire substrate. (b) Deposition of a 20 nm NaF layer using thermal evaporation. (c) Sulfurisation process where sulfur exchanges with oxygen.

3.2.2 Sample characteristics

To characterise the nanoribbons we employ scanning electron microscopy (SEM), Raman spectroscopy, and atomic force microscopy (AFM). Figure 3.5 shows secondary-electron SEM images of a typical MoS_2 nanoribbons on c-cut Al_2O_3 (sapphire) substrates. The nanoribbons can have a length of up to tens of microns and generally a width of less than 0.5 µm, resulting in a length-to-width ratio of over 20. From the SEM images, we clearly see that some nanoribbons have an adjacent monolayer surrounding the nanoribbon, while others do not.

Figure 3.6 shows a typical Raman spectrum from a nanoribbon as well as a monolayer flake. The Raman spectra were taken using a 532 nm laser which was focused onto the sample to a diffraction-limited spot size. The inset shows the whole Raman spectra obtained and highlights the zoomed in region with the two characteristic Raman peaks. The two Raman peaks of MoS_2 arising are from the in-plane ${E^1}_2$ and out-of-plane A_{1g} Raman modes. The peak position difference between the Raman modes of 25 cm^{-1} for the nanoribbon usually denotes a bulk MoS_2, which is similar to previous reports [100, 105, 106].

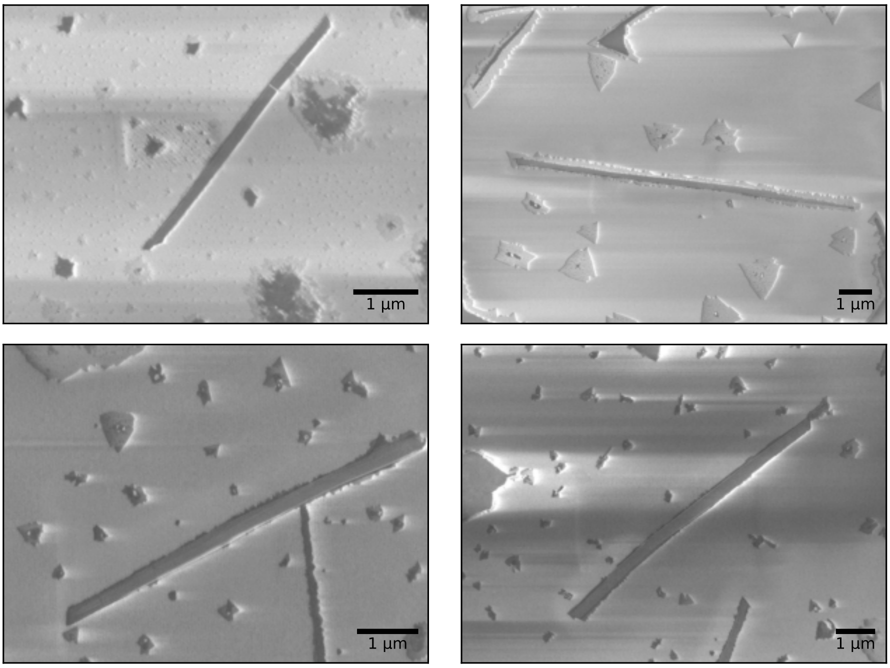

Figure 3.5. Scanning electron microscope (SEM) images of typical nanoribbons grown through the two-step process with varying length and size. Monolayer regions cannot only be found near the nanoribbons, but also in some cases at the base of the nanoribbon.

An AFM map of the specific nanoribbon which we study with THz-SNOM can be seen in Figure 3.7, where Figure 3.7(a) is a large area scan capturing all of the nanoribbon and surrounding pieces, and Figure 3.7(b) is a close-up of one corner of the nanoribbon, indicated by the white dotted square in Figure 3.7(a). The step sizes for the large area scan and the close-up scan are 36 nm and 7.5 nm, respectively.

Interestingly, in Figure 3.7, the nanoribbon lacks monolayer edges. Furthermore, a comparison between the AFM map and the SEM images reveals a significantly higher number of nanoribbons in the early stages of growth, suggesting a subsequent halt in their development. Additionally, there is a noticeable absence of triangular monolayer flakes. This indicates that the nanoribbons grew unobstructed, not colliding with other liquid phase droplets which would lead to the formation of the monolayer edges. The height of the nanoribbon varies between 10 nm and 15 nm. The nanoribbon has a length of $\sim$7 µm with a width of $\sim$ 0.8 µm.

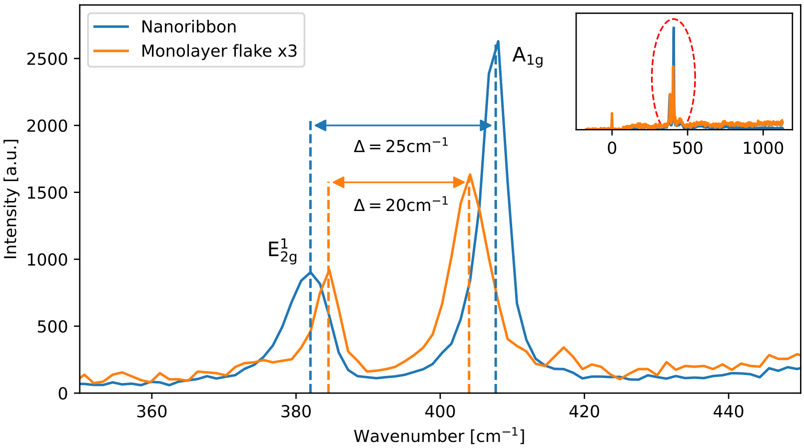

Figure 3.6. Raman response of a nanoribbon and a monolayer flake in near proximity of the nanoribbon. The monolayer response is multiplied by a factor of 3 for better visual comparison. The Raman peaks E^1_{2g} and A_{1g} peak are indicated with dashed lines and the distances between the peaks are found to be 20 cm^{-1} and 25 cm^{-1} for the monolayer and the nanoribbon, respectively.

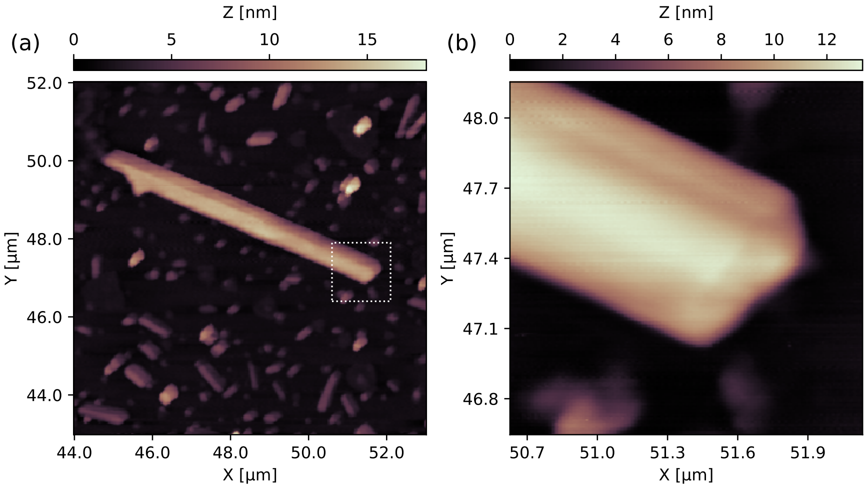

Figure 3.7. Atomic force microscope maps of the specific nanoribbon on a c-cut Al_2O_3 (sapphire) substrate used for the THz-SNOM measurements. (a) A 9 × 9 µm^2 overview scan of the entire nanoribbon and its surrounding with a 36 nm step size, and (b) a zoomed in 1.5 × 1.5 µm^2 scan of the corner of the nanoribbon with a 7.5 nm step size, indicated by the white dotted square in (a).

3.3 THz-SNOM response

Having outlined general characteristics of the nanoribbon, we now begin studying the MoS_2 nanoribbon in the terahertz region. We use the THz-SNOM, since the dimensions of the nanoribbon are several orders of magnitude lower than the diffraction limit of the light. We start by performing the whitelight scans, which will give us a weighted frequency averaged response of the nanoribbon. Figure 3.8 shows the whitelight response for the large area scan for the harmonic orders $m = 2, 3, 4$. Each harmonic order has been normalised to their respective background, represented by the mean of a 10x10 pixel square seen in the bottom right corner of Figure 3.8. As mentioned previously, by increasing the harmonic order, we increase the field concentration and thereby in turn increase the near-field to far-field ratio. This increases the contrast between regions of different material properties, however, doing so also decreases the intensity of the measured signal, thus lowering the signal-to-noise ratio. This is evident from Figure 3.8(c), which shows the $m = 4$ harmonic signal, where the background response, which ought to be close to unity due to the normalisation, varies from 0.9 to 1.20. This indicates we are approaching the noise floor of the detector. We also notice, that some features which are visible in the $m = 2$ and $m = 3$ signal are no longer distinguishable from the substrate, again highlighting the trade-off of going to the higher harmonic orders. Therefore, we will mainly focus on the $m = 2$ and $m = 3$ signal.

Examining the whitelight response of the nanoribbon we notice that the reflected signal is less than that of the substrate. This indicates that the near-field reflection coefficient β, and by that extension the permittivity, of the MoS_2 nanoribbon is smaller than that of sapphire in the frequency band covered by the light source (0.5 THz - 2 THz). Within the nanoribbon itself, we also see a variation in contrast, indicating that the material properties of the nanoribbon varies at the nanoscale.

In Figure 3.9 we see the whitelight response of the corner of the nanoribbon. Figure 3.9(a) shows the same overall characteristics as we saw for the large-area scan in Figure 3.8(a), with the nanoribbon yielding a lower signal than the substrate. In the close-up scan, we specifically enhance the visualisation of the contrast within the nanoribbon itself, where a slight ridge with increased signal is seen going down the nanoribbon. A line profile of this feature along with the AFM profile can be seen in Figure 3.12(a), where it is evident the increase in signal aligns with a decrease in height of the nanoribbon. This suggests that the change in layers or the interface between layers might be the cause of the change in material properties in that region. Furthermore, we notice that around the nanoribbon we have a small band with increased signal. This band is attributed to the fact that the tip when moving from the nanoribbon onto the substrate feels a contribution from both materials, which effectively appears as a rising edge.

Grischkowsky *et al.* measured the refractive index of common dielectrics and semiconductors with far-field THz-TDS back in 1990, where they measured the refractive index of crystalline sapphire for both its in-plane (ordinary) and out-of-plane (extraor-

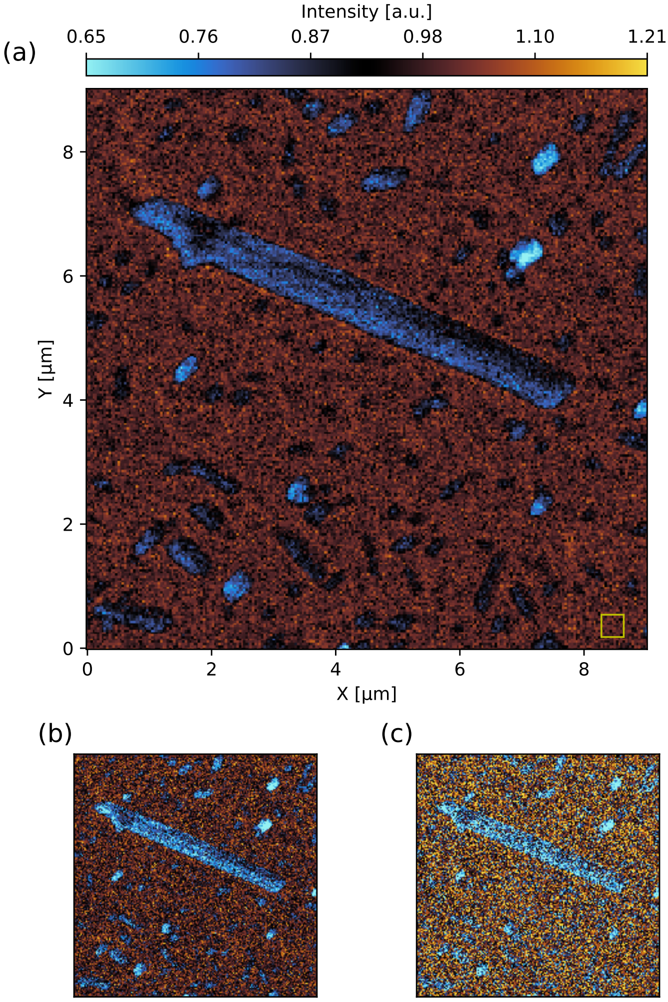

Figure 3.8. Whitelight map of the whole nanoribbon and its surroundings for (a) second harmonic order, (b) third harmonic order, and (c) fourth harmonic order. Each map has been normalised to the background. The yellow square in the bottom right corner of (a) indicates the 10x10 pixel area used for the background normalisation. The step size used for this scan is 36 nm. (b) and (c) have the same coordinates as (a) and all maps are plotted on the same colour scale.

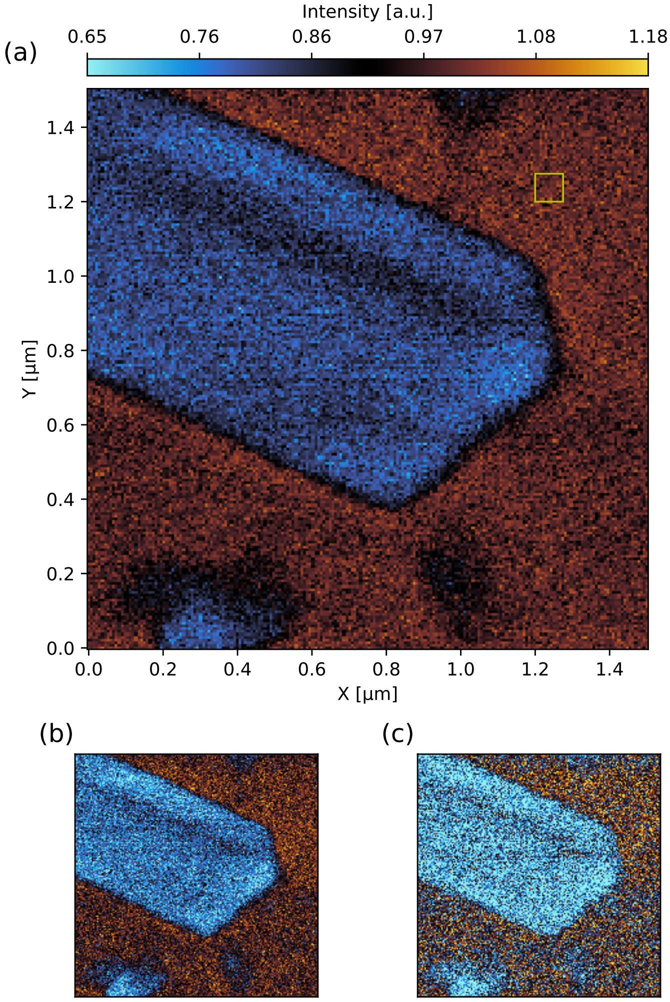

Figure 3.9. Close-up whitelight map of the corner of the nanoribbon for (a) second harmonic order, (b) third harmonic order, and (c) fourth harmonic order. Each map has been normalised to the background. The yellow square in the top right of (a) indicates the 10×10 pixel area used for the background normalisation. The step size used for this scan is 7.5 nm. (b) and (c) have the same coordinates as (a) and all maps are plotted on the same colour scale.

dinary) components [107]. Since, the tip mainly probes the out-of-plane component as described in chapter 1, this suggest that we should use the extraordinary component of the refractive index of sapphire. Within our bandwidth the refractive index shows only a slight increase with increasing frequency, thus we choose the refractive index of the substrate to be $n_{\mathrm{sub}} = 3.41$ across our bandwidth.

3.3.1 FEM simulations

As previously established, the finite dipole model (FDM) describes the tip-sample interactions under the illumination of a light source, where the scattered field is described through the effective polarizability (α_{eff}) and the near-field reflection coefficient $\beta(\varepsilon)$. Yet, due to the complex nature of tip-sample interactions, it is currently not possible to directly invert the model and extract the optical and electrical properties from the sample without approximations [48]. Therefore, root-finding routines and finite element method (FEM) simulations are currently being explored in order to perform quantitative studies [49, 59, 64]. We perform FEM simulations as described in section 1.5, where we model the geometry of the MoS_2 nanoribbon as a rectangle with a width of 800 nm and a height of 15 nm.

The material properties of the MoS_2 nanoribbon were modelled according to Eq. (3.1), with the parameters for the MoS_2 and the tip modelling shown in Table 3.1.

Description	Parameter	Value
Dipole half-length	L	40 µm
Tip radius	R	30 nm
Minimum height distance	h_0	3 nm
Maximum height distance	h_{max}	100 nm
High-frequency limit permittivity	ε_∞	11.45
Scattering time	τ	500 fs
Carrier concentration	n	$1 \cdot 10^{17}$ cm^{-3}
Optical frequency	ν	1.25 THz
Effective mass	m^*	$0.58m_0$

Table 3.1. Parameters used in FEM simulations.

The carrier concentration n, was estimated based on electrical measurements on similar nanoribbons, where electrodes had been fabricated onto the nanoribbons. Those measurements suggest a relatively high carrier concentration, but still within previously reported values [99].

The scattering time τ, has been chosen to be $\tau = 500$ fs, which is a long scattering time compared to previous literature [96, 99, 108], where in the terahertz region the reported scattering time is $\sim$ 135 fs. However, assuming the semiconductor to be described by the Drude model given in Eq. (3.1), then in order to recreate the contrast ratio we see from the whitelight maps, such a long scattering time is necessary.

Optical-pump terahertz-probe (OPTP) experiments have revealed carrier mobility values for multilayer MoS_2 at room temperature, measuring 257 $cm^2V^{-1}s^{-1}$, and at cryogenic temperature (30 K), measuring 4200 $cm^2V^{-1}s^{-1}$ [109]. Using the relationship $\tau = \mu m^*/e$, these values correspond to scattering times of approximately 90 fs and 1.4 ps, respectively, while Docherty *et al.* reports OPTP measurements of chemical vapour deposition (CVD) grown monolayer and trilayer MoS_2 with scattering times of $\sim$ 120 fs and $\sim$ 20 fs, respectively [110]. Thus, while assuming a scattering time of 500 fs in multilayer MoS_2 is not entirely implausible, it implies extremely high quality MoS_2, which might be a strong claim for nanoribbons grown by PLD. Therefore, further investigations on this topic is needed.

As we have established previously, by nature of the technique, the light is scattered to large values of in-plane momenta, as governed by Eq. (1.25) which describes the weighted in-plane momenta distribution. By that extension, the inclusion of a momentum dependency of the permittivity may result in lowering of the scattering time needed to reproduce the contrast ratios in the FEM simulations. This can be done by utilising a Lindhard-Mermin model [111,112], though currently implementing this is a non-trivial matter, and would require extensive computational power. As a result, for now we ignore any non-local effects in the modelling of the permittivity. In the proceeding chapter, however, we will investigate the effects of non-locality and its impact on a material's conductivity.

Figure 3.10(a) shows a 2D cross-section of the nanoribbon and the tip and how the dynamic meshing has been defined by COMSOL. We see a high density of nodes around the MoS_2 and the apex of the tip, whereas further away the nodes become less dense. This is in order to capture all the interactions of the material and directly under the tip while simultaneously lessening the computational strain by minimising the nodes far away from the interaction points.

A still frame of the incoming and scattered fields can be seen in Figure 3.10(b). This figure highlights the fact that the tip functions as an antenna strongly enhancing the field at both ends of the tip, as well as showing the refraction going from air to sapphire. As previously described, the scattered field is approximated as the line integral around the ellipsoidal tip.

To replicate the tapping motion of the tip, we conduct simulations at varying tip-sample distances. From these, we then demodulate into the higher harmonic components to isolate the near-field response. An example of the field enhancement under the tip is visualised in Figure 3.11 for different tip-sample distances. Utilising the equation for the field enhancement in Eq. (1.14) with our parameters, shown in Table 3.1, we achieve a field enhancement of $\gamma_0 \approx 400$. In this figure, we clearly see how at the closest distances (Figure 3.11(d) the field is strongly enhanced and localised within the sample to a scale significantly lower than the free-space wavelength. While the field also permeates the substrate, the visibility of this penetration is limited due to the colour map.

The result of the FEM simulation can be seen in Figure 3.12(b). Upon comparison between the FEM simulation and the experimentally obtained data shown in Figure 3.12(a), it is clear that the simulation closely replicates the observed trends.

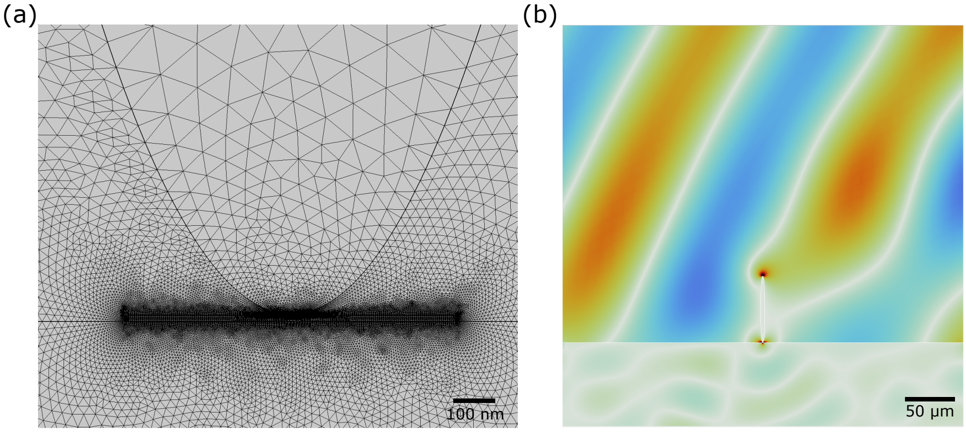

Figure 3.10. (a) Dynamic meshing used to simulate the tip-sample interactions, and (b) still-frame of the interacting out-of-plane fields, E_y, for the incoming and scattered fields.

With increasing harmonic order, we see an increase in contrast between substrate and sample as expected. Notable, in Figure 3.12(a), we see an overall arch arising with the nanoribbon in the $m = 4$ signal, not to be confused with the slight increase in signal around 0.8 µm, whereas a flat response is observed across the nanoribbon in the $m = 2$ and $m = 3$ signal. Similar tendency is observed from the FEM simulations.

Another striking feature from the FEM simulations are the significant decrease in signal at the edges of the nanoribbon, which we do not observe in the experimental data. This is most likely an artefact arising due to the step-function shape of the nanoribbon. In order for the tip to measure the substrate response just before the edge, it is necessary to raise the tip slightly to avoid collision with the nanoribbon, thus effectively decreasing the near-field response.

An important note is, when comparing the experimental data with the FEM simulation, the simulated response is at a single frequency, $\nu = 1.25$ THz, whereas the experimental data is a whitelight response, and therefore a weighted response of all frequencies involved. Thus, there may be some interactions in the experimental data which is not captured in the simulation, and the two plots in Figure 3.12 cannot be directly compared, but only the overall trend is comparable.

3.4 Extraction of optical parameters

The optical properties in the THz range can be extracted from the terahertz response, which has been a common practice in far-field THz-TDS for many years [30], however, this practice differs when studying the near-field THz response. As described in

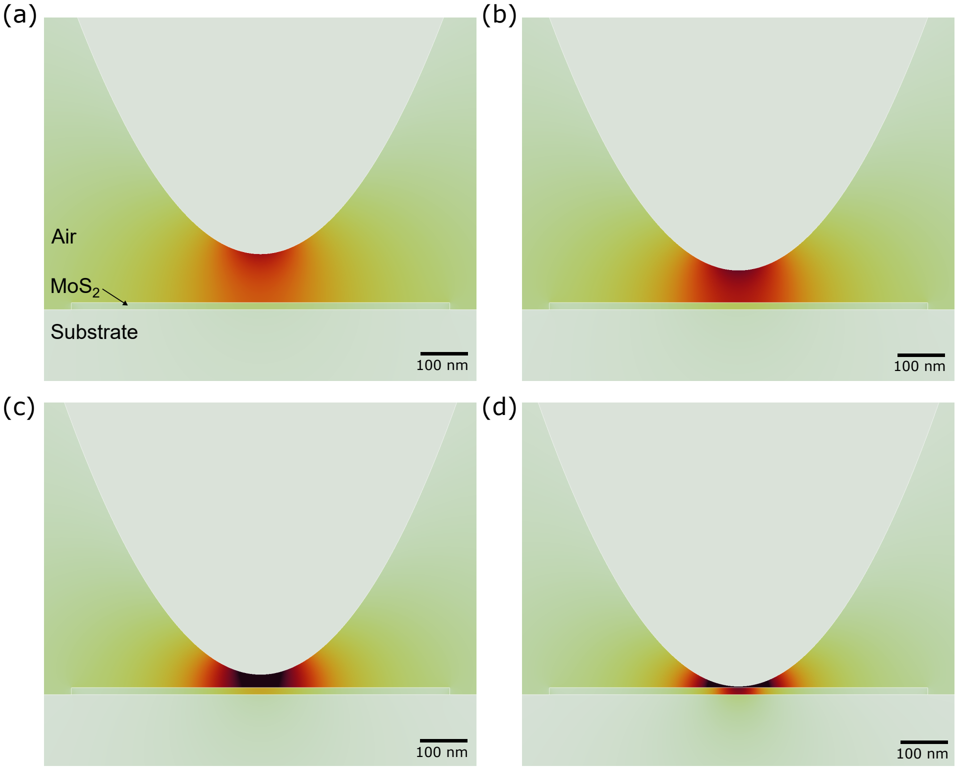

Figure 3.11. Visualisation of field enhancement caused by the metallic tip as calculated from FEM simulations for distances (a) 100 nm, (b) 68 nm, (c) 28 nm, and (d) 3 nm from the surface of the sample, with a tip radius of $R = 150$ nm.

Eq. (1.29), the scattering cross-section, which is the quantity we measure in the system, is given as,

$$\sigma_m(\beta) = \int_0^T \sigma(\beta, H(t))\,\mathrm{e}^{i\Omega_m t}\mathrm{d}t = (1 + r_s)^2\,\alpha_{\mathrm{eff},m}. \tag{3.2}$$

Due to the complex nature of this relation, it is currently not possible to directly invert and extract the the optical properties, though attempts to simply the expression through, e.g., a Taylor expansion of the effective polarisability α_{eff} have shown promising results [48].

Another approach is to calculate the near-field response through Eq. (3.2), based on a modelled response of the optical properties of the material and employ root-finding and minimisation methods to determine the material properties. This is done by varying it as a free parameter until a match with the experimental data is found. The minimisation method is the approach we choose to employ to extract the

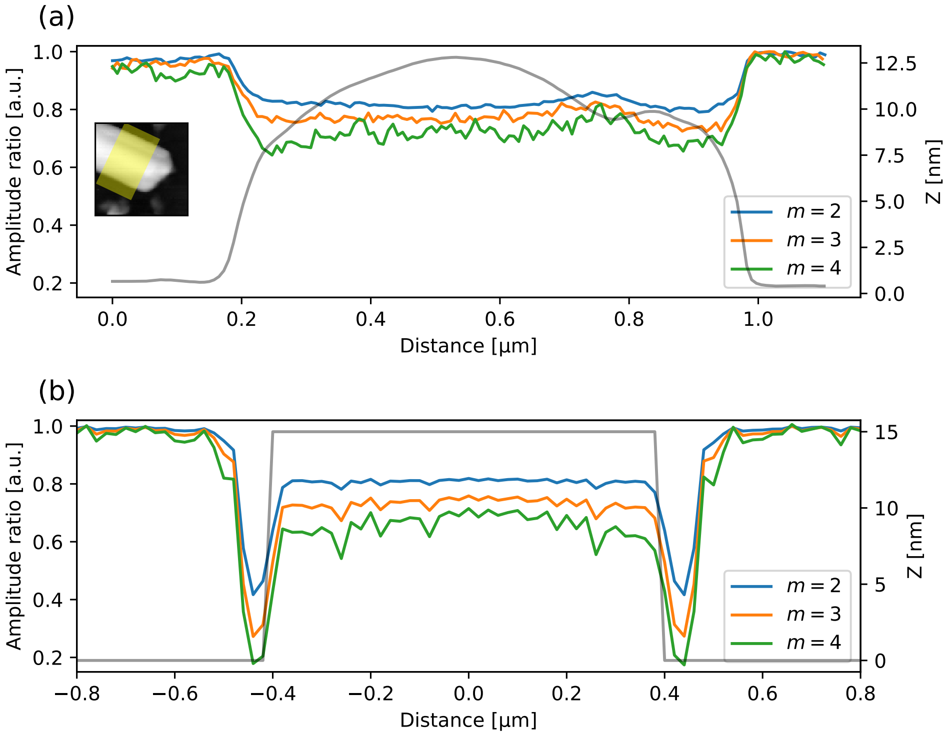

Figure 3.12. Whitelight line profiles for (a) experimental, and (b) FEM simulation. (a) Line profile averaged over a region of the nanoribbon highlighted by the yellow square on the AFM amp shown in the inset. The grey solid line shows the height profile extracted from the AFM map along the same line. (b) Line profiles extracted from FEM simulations with parameters given in Table 3.1. The solid grey line indicates the height profile of the nanoribbon.

permittivity of the nanoribbon. The goal is then to create a two-dimensional map depicting the permittivity as a function of the spatial coordinates.

Currently, we have the two-dimensional maps depicting the whitelight response of the nanoribbon. These maps include a scan over a large area, as shown in Figure 3.8, and a close-up of the corner, shown in Figure 3.9. Since we employ a minimisation method, meaning we calculate a simulated response and adjust the permittivity until it aligns with the experimentally measured data, we can use the whitelight maps to extract a “frequency averaged” permittivity. This is only possible if no distinct features, such as resonances, are present within our bandwidth. In Figure 3.2 we see that, based on far-field THz-TDS measurements of bulk MoS_2 and the model shown in Figure 3.3(a), we would not expect there to be any distinct features within the bandwidth of our source (0.5 THz - 2.0 THz) for our sample. However, a one-to-one comparison may be difficult to make, since the nanoribbon is only 15 nm in height, and we show the response of bulk MoS_2 as well as the far-field response. Nonetheless, we proceed under the assumption of no distinct features in the spectrum for our bandwidth.

3.4.1 Minimisation technique

For the minimisation, we use the "**minimize**" function within the python package "**scipy.optimize**". This package contains a multitude of different minimisation techniques, with many having advantages and disadvantages accompanying them. To our experience, the "**minimize**" function was one of the fastest, which given the pixel densities of our maps was a significant attribute, while also being relatively stable. The stability of the techniques was characterised by how close and consistent they would arrive at a known testing value. Within the "**minimize**" function we used its "**COBYLA**" method, which stands for Constrained Optimisation BY Linear Approximations. The "**COBYLA**" method uses linear approximations of the objective and constraints to guide the search for the optimal solution. The disadvantages of the "**COBYLA**" method is that it may find a local minimum (or maximum) instead of the global minimum (or maximum). Due to this fact, the method might converge to an incorrect value, depending on the complexity of the objective function and constraints. Another method worth mentioning is the "**differential evolution**", which aims to find the global minimum (or maximum) of a scalar objective function over a specified search space, which can be bounded or unbounded, and the method is stochastic by nature. "**Differential evolution**" is used for global optimisation. Thus, if you have a specific starting point and are interested in finding a local minimum or maximum, then "**minimize**" is a decent choice. This could be the case, when you have a good initial guess. On the other hand, if you need to find the global minimum or maximum over a broader search space, especially for complex, multi-modal functions, "**differential evolution**" is more suitable, albeit more computationally demanding.

Our objective function is chosen to be,

$$f(x) = \left|(\eta_{\text{target}} - \eta_{\text{theory}})\right|^2 , \tag{3.3}$$

where η is the scattering ratio given as, $\eta = \frac{\sigma_{m,\text{sample}}}{\sigma_{m,\text{substrate}}}$. Describing the objective this way allows us to account for both the real and imaginary part.

We use the transfer matrix model described in subsection 1.3.1, with a single propagation layer and no surface conductivity. The thickness of the MoS_2 nanoribbon layer at each pixel is directly inferred from the corresponding AFM map. A height threshold is set on each WL map based on the AFM map. Any point below the threshold is considered to be substrate and the permittivity is set to be $\varepsilon_{\text{substrate}} = 11.63$.

An additional noteworthy aspect is the handling of the phase map obtained from the whitelight scan. When performing a measurement at a given spatial position and delay stage position, an amplitude and phase is obtained. This is because of the demodulation of the higher harmonic orders from the tapping motion. As described in section 2.1 when measuring a full time trace, we need to adjust for the phase offset. We do this by defining the phase at the peak position in time domain to be zero. Thus, the phase map obtained from a whitelight scan, should in principle be zero everywhere. Therefore, we only need the amplitude map to extract the optical parameters from the map. As a consequence of this, however, we are also limited to only probing the real part of the permittivity, since we do not possess any phase information. The extracted permittivity should therefore in principle yield an imaginary part equal to zero, if an complex permittivity is used in the minimisation.

When calculating the modelled response, the use of an effective frequency is necessary. Since, at the peak of the pulse in time-domain, all frequencies are assumed to be in phase, all frequencies are assumed to participate in the interactions, thus we opt for an approximation based on the spectral profile of our pulse, which exhibits maximal intensity around 1 THz. Therefore, we approximate the effective frequency as $\nu_{\text{eff}} = 1$ THz.

A summary of all the parameters used to calculate to theoretical response through the FDM can be seen in Table 3.2.

Description	Parameter	Value
Dipole half-length	L	40 µm
Tip radius	R	30 nm
Minimum height distance	h_0	0 nm
Tapping amplitude	A	170 nm
Tapping frequency	Ω	83 kHz
Fraction of induced charge	g	0.7
In-plane momentum	q	$2.47 \cdot 10^5$ cm^{-1}
Optical frequency	ν_{eff}	1 THz
Substrate permittivity	$\varepsilon_{\text{subs}}$	11.6281 [107]

Table 3.2. Parameters used in FDM calculations.

3.4.2 Permittivity minimisation

Figure 3.13 and Figure 3.14 show the resulting permittivity maps extracted from their respective whitelight images using the minimisation routine. The permittivity extraction has been performed for the $m = 2$ and $m = 3$ harmonic orders. As expected, the imaginary part of the complex permittivity is extremely small, where the structure in the plot is visible simply due to the masking of the substrate.

The two harmonic orders should in principle yield the same permittivity, and therefore be identical, however, we observe some differences in the values of the permittivity at the same position. The $m = 3$ harmonic order appears to converge at a slightly lower value for most points, while still maintaining the highest values in the same range as for the $m = 2$ harmonic order. To further investigate this, we extract a line profile across the nanoribbon for the $m = 2$ and $m = 3$, which is shown in Figure 3.15. From Figure 3.15 we see that the two harmonic orders overall are well in agreement, but it is also evident that the $m = 3$ harmonic generally yields a lower permittivity in some regions. The signal also appears to fluctuates significantly more, which most likely is related to the increase in noise due to increasing the harmonic order.

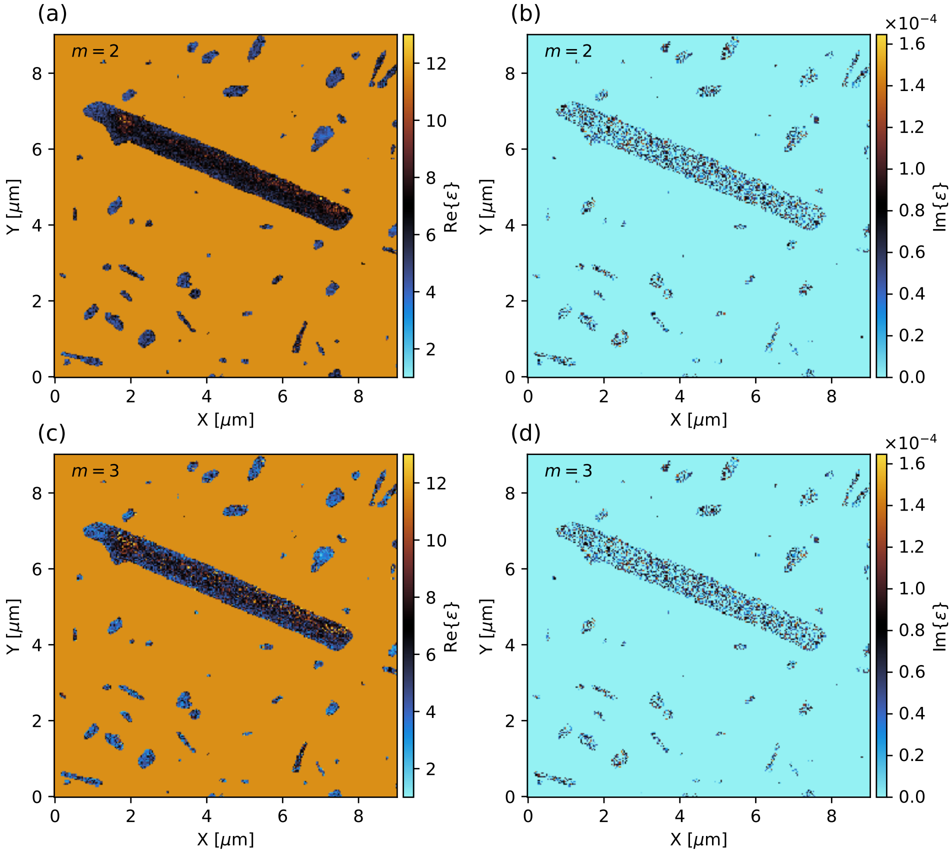

Figure 3.13. Extracted permittivity for the large-area scan of the MoS_2 nanoribbon. (a) Real part of the permittivity and (b) imaginary part for the $m = 2$ harmonic order, and (c) and (d) for the $m = 3$ harmonic order.

An explanation for this slight deviation between the harmonic orders might be the height used at each pixel. Govyadinov *et al.* investigated the extraction of permittivity and depth and the interplay between the different harmonic orders [113]. In their work, they suggest to use a thickness of the material under investigation such that all harmonic orders yield the same extracted permittivity. The thickness of the nanoribbon we use in the permittivity is directly taken from the AFM map acquired

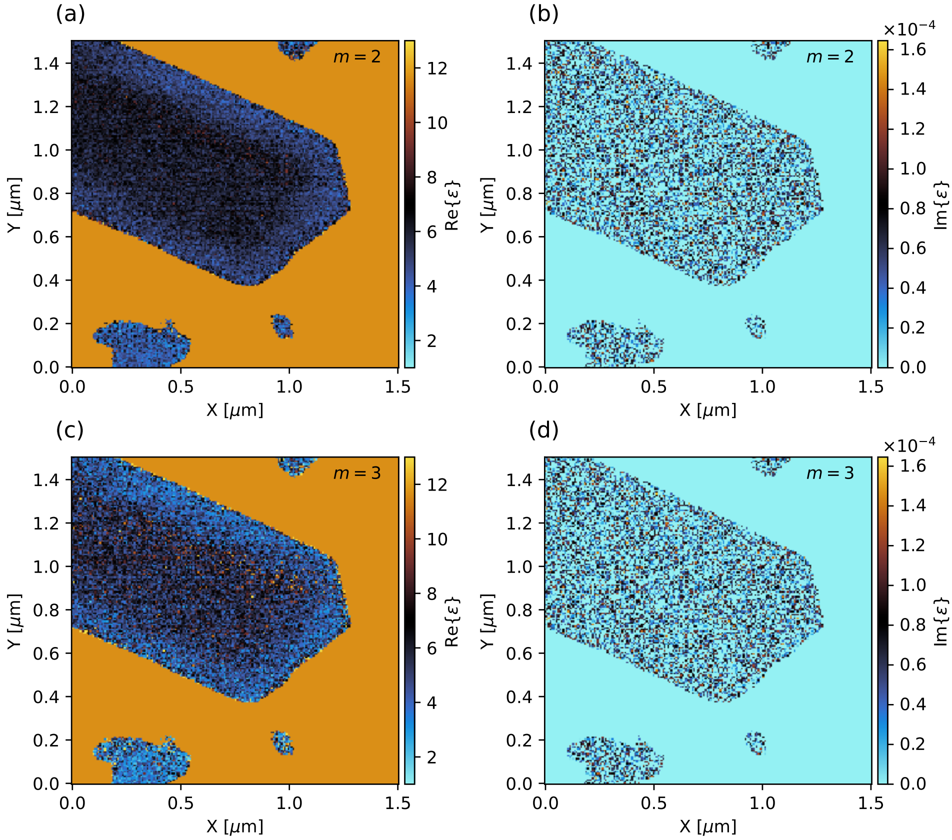

Figure 3.14. Extracted permittivity for the close-up scan of the corner of the MoS_2 nanoribbon. (a) Real part of the permittivity and (b) imaginary part for the $m = 2$ harmonic order, and (c) and (d) for the $m = 3$ harmonic order.

at the same time as the whitelight scan. It is possible that using a different value for the thickness would cause the harmonic orders converge to the same permittivity. Thus, an approach to further investigate this dependence on the thickness, would be to sweep the thickness in the modelled permittivity until the harmonic order are equal. This, however, requires extensive computation, since at each pixel a several minimisation iterations would be needed: one for each thickness. Then a comparison between each optimal permittivity needs to be performed to find the convergent permittivity, before moving to the next pixel. While adopting this approach would likely enhance the accuracy of the extracted permittivity, it remains to be implemented. Regardless, Figure 3.15 suggests that the current extracted values relatively accurate and can therefore be used as estimation of the true permittivity, with the given model parameters.

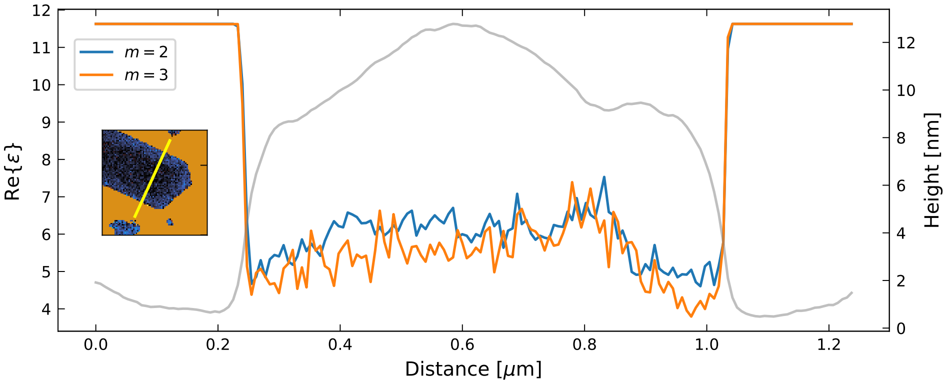

Figure 3.15. Line profile of the extracted permittivity of the close-up scan across the nanoribbon for the $m = 2$ and $m = 3$ harmonic orders. The width of the line profile is 5 pixels and the location at across which the line profile was taken can be seen in the inset. The AFM profile is shown in grey with the height seen on the right.

To further investigate the correlation between the extracted permittivity and the height of the nanoribbon at which point it was extracted, we can plot all permittivities as a function of the height. The result of this can be seen in Figure 3.16(a) for the large area scan and Figure 3.16(b) for the close-up high resolution scan. Desirable results in this context would show as a narrow, linear profile, implying that the permittivity of the MoS_2 nanoribbon exhibits little height dependency. This behaviour would align with our assumption that the nanoribbon behaves similarly to bulk material. Expecting a narrow, straight line would imply that no variation in the permittivity exists within the nanoribbon at the nanoscale. On the whitelight maps shown in Figure 3.9 and the permittivity maps shown in Figure 3.14, we do, however, see a slight contrast within the nanoribbon itself. But we have also seen, that this increase in contrast coincides with a decrease in the height. Therefore, we might expect a region of heights with increased permittivity. It is crucial to emphasise that this examination of the relationship between height and permittivity differs from the previously mentioned method of optimising height between harmonic orders. Although performing a height optimisation could result in slight altering of the distribution we observe in Figure 3.16, it is not a guarantee that the optimal height at each pixel would yield in a narrow, straight line distribution, since variation within the nanoribbon itself would still be present.

The overarching pattern seen in Figure 3.16 mirrors the expected distribution, though there exists a substantial spread in permittivity values at a given height. Furthermore, we also observe a slight tilt in the distribution, indicating lower permittivity at lower height. The presence of a tilt makes intuitive sense, since we have established that when decreasing the thickness of MoS_2 down towards a single layer, the material properties change drastically.

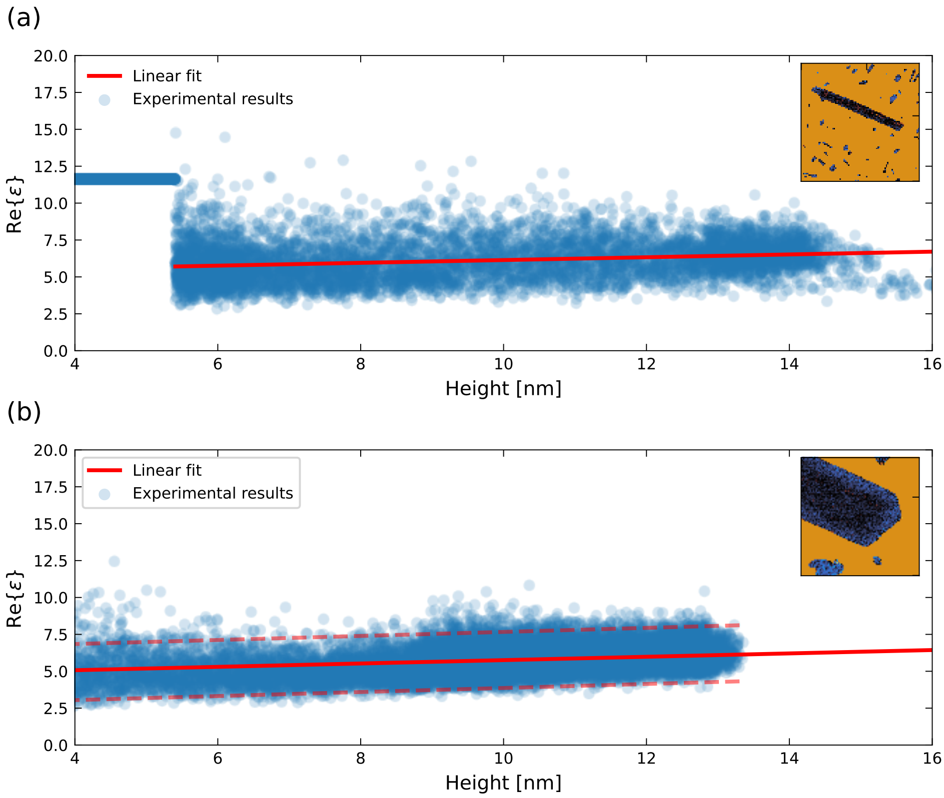

Figure 3.16. Distribution of the extracted permittivity against the height of the MoS_2 at which is was extracted for (a) the large-area scan and (b) the close-up scan of the corner of the nanoribbon. The solid red line is a linear regression fit yielding (a) $y = 0.0947x + 5.195$ and (b) $y = 0.114x + 4.616$ in units of [nm] for x. The parameters used for the FDM are listed in Table 3.2. The dashed red lines in (b) are guidelines used to estimate the upper and lower bounds of the permittivity spread at each height. Each data point is plotted with a transparency of 0.2, thus a more solid colour indicates multiple data points overlapping.

However, another feature we observe is the contrast within the nanoribbon itself, specifically evident in the high-resolution close-up scan of the corner. This shows up as an increase in permittivity at the specific heights. The dashed red lines in Figure 3.16(b) indicates the upper and lower bounds of the spread of permittivity, but around 9-11 nm we observe a cluster of higher permittivities. Comparing this height to the location of the observed increase in signal seen in, e.g., Figure 3.12(a) and Figure 3.15 we observe a strong agreement. The cluster is therefore attributed to the contrast within the nanoribbon.

The few high value permittivities we see between 4 nm to 5 nm are most likely not from the nanoribbon, but instead from the small flakes around it. The general trend we see from these flakes around the nanoribbon is they appear with lower permittivity than the nanoribbon, but also have a few points near the edge which yields a permittivity closer to that of the substrate. The explanation for this could be that at the boundary between substrate and sample we have an increased contribution from the substrate which has a higher permittivity, due to the interaction volume. Thus, depending on how well a height threshold is set some sample points near the edge may be more effected by the substrate than those near the centre.

3.4.3 Impact of FDM parameters on extracted permittivity

To calculate the FDM response we have estimated the parameters based on currently accepted values seen in literature. However, an investigation of the impact each parameter has on the extracted permittivity will shed light on the sensitivity of the model to these parameters. We run the minimisation routine sweeping through parameters of the model such as, e.g., the in-plane momentum q, the length of the dipole L, the tip radius R, and the fraction of induced charge g, while keeping the other parameters fixed.

Figure 3.17 shows the distribution of permittivities as a function of the height for the large-area map in the left column and for the close-up map in the right column for different in-plane momenta. The specific in-plane momentum is labelled in the top left corner of each plot. Figure 3.17(e) and (d) corresponds to the peak in the weighted in-plane momenta distribution averaged for a single tapping cycle with a tip radius of $R = 30$ nm. Here it is evident that shifting the momentum significantly changes the value of the extracted permittivity, as seen from the intercept of the linear fit. The overall shape of the distribution appears largely independent of the momentum, except for at low momenta outliers from the main distribution appears more frequent.

Currently, we lack an experimental methodology to accurately measure the in-plane momenta to which the tip scatters light. Consequently, an in-plane momentum of $q = 2.47 \cdot 10^5$ cm^{-1} is selected as the most representative value. This decision is based on the observation that increasing the momentum beyond the anticipated value yields only marginal modifications in the distribution. In contrast, reducing it significantly increase the spread in extracted permittivities at a specified height. Given that the whitelight images exhibit a relatively consistent response, a minimal spread in the extracted permittivities at a particular height is anticipated.

Studying the impact of the tip radius R resulted in marginal modifications to the extracted permittivity, where changing the tip from a minimum of 15 nm radius to a 200 nm radius only resulted in a 12% increase in the intercept of the linear fit, and a 7% increase in the slope. The distribution remained largely unchanged. The same trend was observed for the major semi-axis length L, which is to be expected, since within the framework of the FDM, the length L and the tip radius R mostly

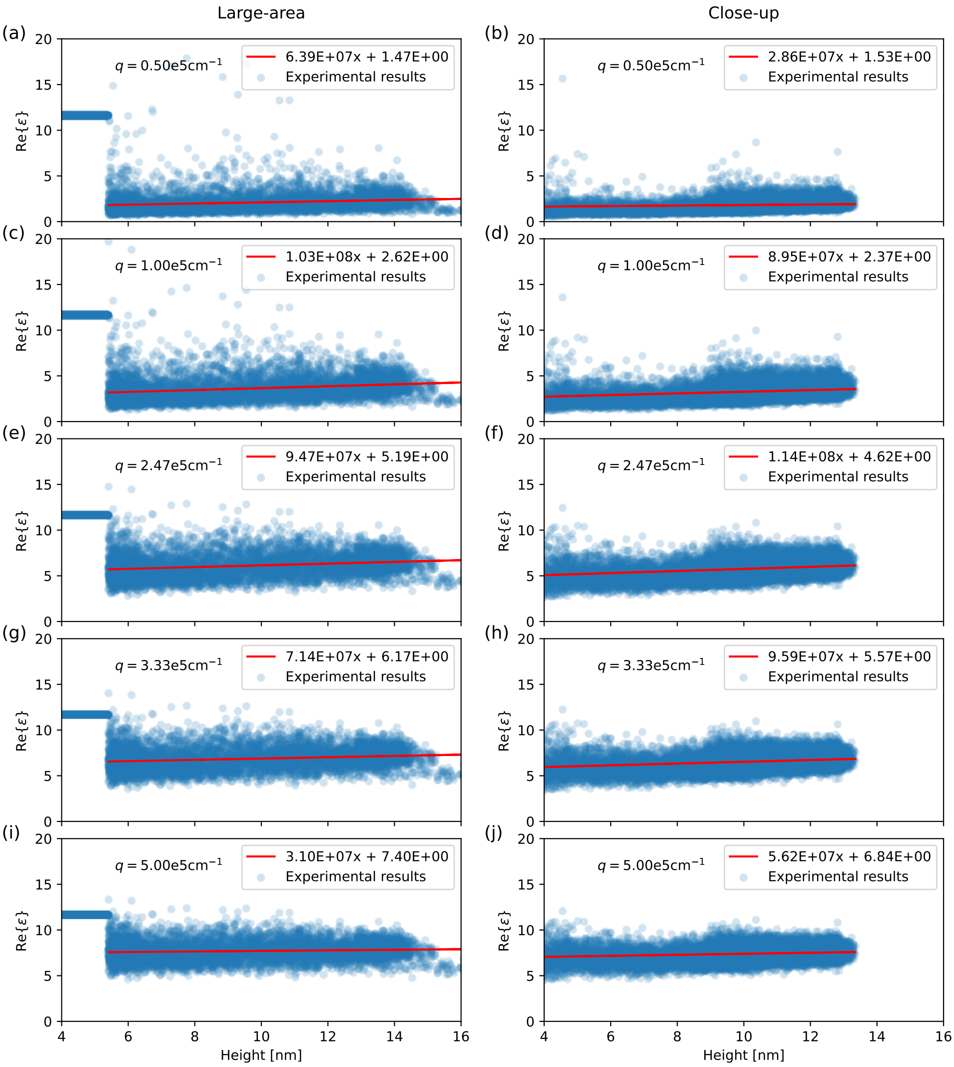

Figure 3.17. Extracted distributions of permittivities from the minimisation routine performed at different in-plane momenta noted in each plot for the large-area scan on the left and the close-up scan on the right. The slope and the intercept of the linear fit to each plot is given in the legends in units of [m] for x.

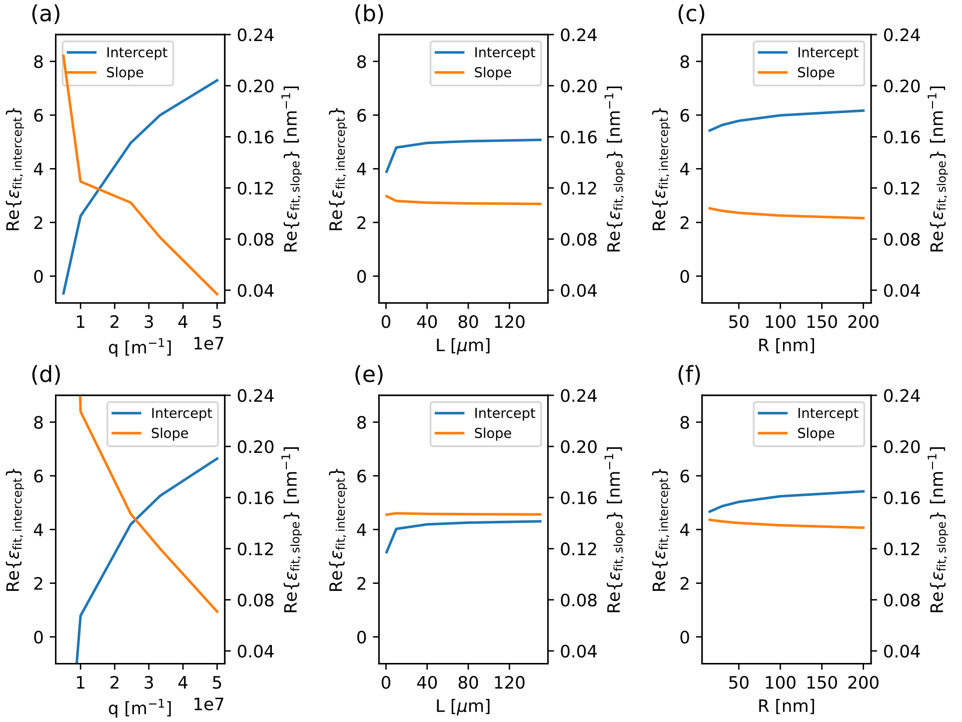

Figure 3.18. Slope and intercept from the linear fit made to the height distribution as see in Figure 3.17 as a function of the in-plane momentum q, major semi-axis length L, and tip radius R for (a)-(c) large-area scan and (d)-(e) close-up scan. Limits on all axes are the same for ease of comparison.

appear in terms of ratios. A summary is shown in Figure 3.18, where we observe that for the major semi-axis length and tip radius the extracted permittivities are largely unaffected over a range of reasonable values, whereas over a reasonable range values for the in-plane momentum we see a significant impact.

Lastly, the fraction of induced charge g has so far been an empirically determined quantity, primarily chosen as $g = 0.7$ [45, 47]. Later, an additional phase factor was added to the g-factor yielding $g = 0.7\mathrm{e}^{i0.06}$, which served as a correction accounting for propagation dispersion between the charges in the framework. Sweeping different values of the phase factor of g reveals that the model is independent of this phase factor in the THz range, which is expected due to the extremely long wavelength of the THz radiation. Based on these studies, we opt for the parameters seen in Table 3.2.

3.5 Spectroscopic response and challenges

In addition to the whitelight studies we also perform full spectroscopic analysis of the nanoribbon. We perform a line scan across the nanoribbon shown in Figure 3.19(a), where at each point full sampling of the pulse in the time domain was obtained. The line scan has a length of 1.64 µm with a total of 160 pixels yielding a step size of 10.25 nm. At each pixel 5 time traces where obtained for averaging. The line scan starts on the sapphire substrate, and moves over the MoS_2 nanoribbon and back onto the substrate. Figure 3.19(b) and (c) show examples of time traces and their respective spectra for three positions on the MoS_2 nanoribbon named, “start”, “middle”, and “end”, and a reference. The three nanoribbon time traces shown are each an average of three neighbouring scans, since the step size is just 10.25 nm and the estimated spatial resolution obtainable with the tip is ∼30 nm, this averaging can be justified. The reference is generated by averaging 10 substrate scans, with 5 scans from each side of the nanoribbon, since the substrate response has a slight variation on each side of the nanoribbon, which is seen in Figure 3.20(b), where the scattering ratio is plotted.

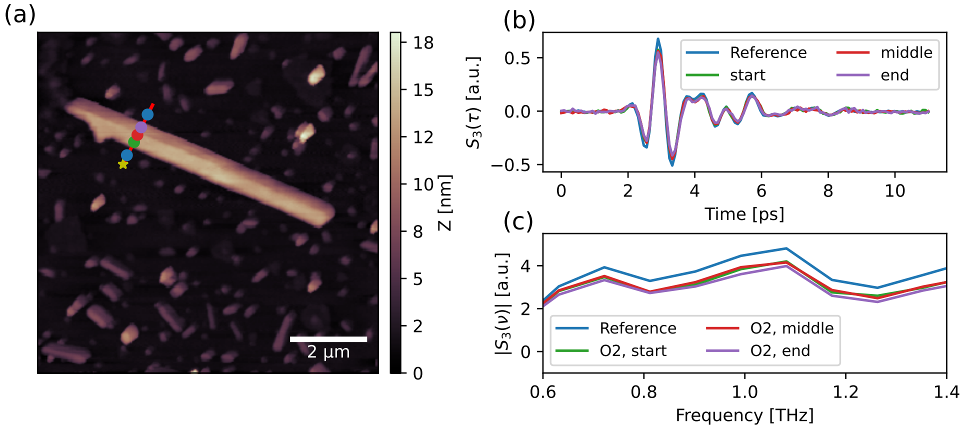

Figure 3.19. (a) Line scan performed across the nanoribbon. Yellow start marks the start position of the line scan. (b) Time traces from the substrate and three positions on the nanoribbon, marked start, middle, and end. The substrate time trace is an average of 5 traces from each side of the nanoribbon. The positions taken are marked in (a). (c) Corresponding spectrum within our bandwidth.

More importantly, we do not observe any strong features in the spectral shape of the MoS_2 nanoribbon, which is the expected response from the far-field bulk studies, further justifying the possibility of using an averaged spectral response, i.e., the whitelight image, to extract an averaged permittivity. On the contrary, the phase show a slight increase towards higher frequencies for not only the MoS_2 nanoribbon, but also just around the edges of the nanoribbon, which could suggest some edge effects.

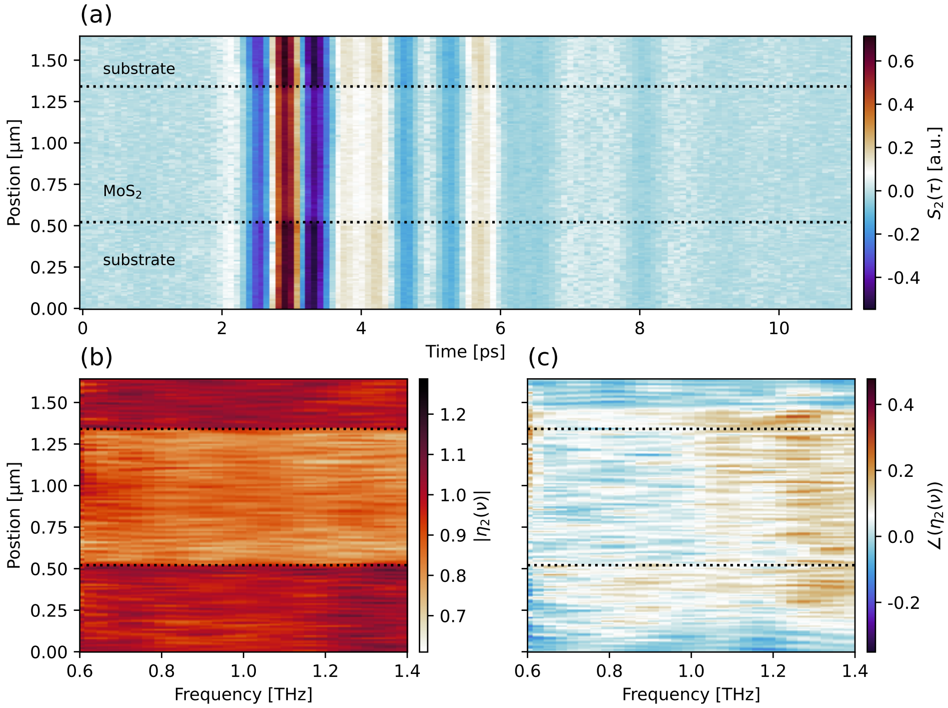

Figure 3.20. Visualisation of the two dimensional data obtained from the line scan across the nanoribbon. (a) Shows the non referenced time traces, (b) shows the spectral scattering amplitude ratio and (c) shows the associated phase. The bandwidth has been limited to 0.6 THz to 1.4 THz due approaching the noise floor elsewhere.

With the spectral amplitude and phase ratio between the substrate and nanoribbon shown in Figure 3.20(b) and (c), we can extract the frequency resolved permittivity using the same minimisation routine as we did for the frequency averaged extraction. Not only will this give us the real part but also the imaginary part and thus describe the full complex permittivity of the MoS$_2$ nanoribbon in our given bandwidth. The result of this are shown in Figure 3.21.

We observe that the spectrally resolved permittivity shows similar values for the real part as we observed from the whitelight image inversion. Furthermore, we now observe a non-zero imaginary part. Comparing these results to the far-field behaviour shown in Figure 3.2, we observe an opposite trend than expected. We observe a decrease in real part with increasing frequency and an increasing imaginary part, whereas the real part for the far-field response slowly converge towards the high frequency permittivity ε_∞ and the imaginary part converge towards zero. This may

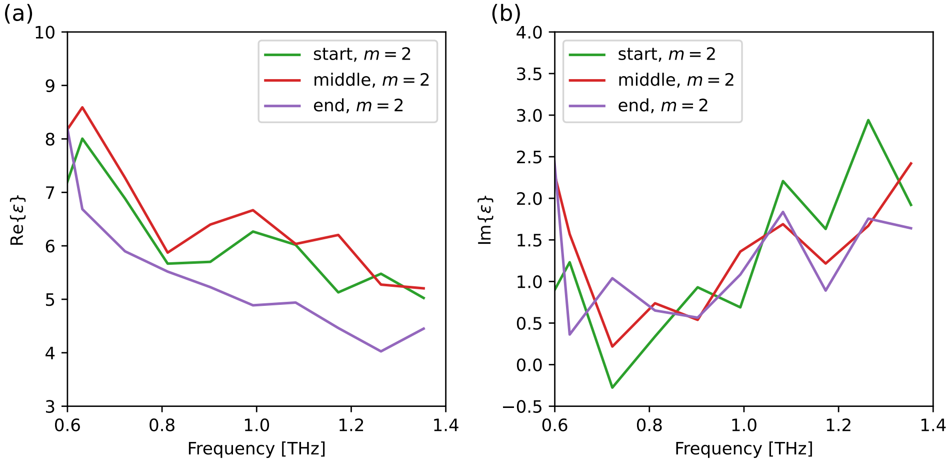

Figure 3.21. Extracted (a) real and (b) imaginary part of the permittivity of the MoS_2 nanoribbon at three positions on the nanoribbon for the $m = 2$ harmonic.

be related to the current limitations that nanoscale THz-TDS faces. The spectrum is heavily dominated by resonances stemming from the geometry of the whole tip and support chip configuration [64]. This resonance can be seen in Figure 3.19(c). Furthermore, repeated time traces taken at the nanoscale show slight variation which may be attributed to uncertainty associated with the measurements. Nonetheless, the extracted values, both real and imaginary, are very much comparable to the expected range of values that we observe in the far-field shown in Figure 3.2 and calculated in Figure 3.3, showing the future potential of nanoscale THz-TDS.

Assuming, however, what we observe are the true values of the permittivity and that the nanoribbon indeed does show an opposite trend within our bandwidth, then we must remind ourselves that we are probing the properties at the nanoscale and comparing it to far-field bulk measurements. Though the nanoribbon is quite large ($0.8\ \mu\text{m} \times 7\ \mu\text{m} \times 15$ nm) it still remains much smaller than the wavelength used to probe the optical properties, thus probing in the deep sub-wavelength regime might induce changes. Another important point to mention is that we are currently comparing the extracted values to a local model, i.e., no momentum dependence. In the next part, we shall see that going from local to non-local responses for conductive materials changes the optical and electrical properties of the material in the THz region significantly. Therefore, further investigation into the non-local properties of the permittivity for MoS_2 must be studied.

Part II

Conductors: Semi-metals and metals

CHAPTER 4

Conductivity contrast

Since its discovery by Nobel laureates Novoselov and Geim [114], graphene has garnered considerable attention for its potential applications in future devices [115]. THz-TDS has proven itself to be an excellent technique to evaluate the material properties of graphene such as the conductivity, due to its non-invasive nature of probing the material [116–119]. As previously mentioned, the need for miniaturisation of devices is crucial for further advances within several branches of science. Consequently, given the increasing integration of s-SNOM and THz-TDS, graphene, a semi-metal, emerges as a natural candidate for study. Using THz-SNOM to study graphene has been done before, though the results seemed detrimental for further studies of graphene with THz-SNOM [120, 121].

4.1 Theory of conductive interfaces in THz-SNOM

In 2018 Zhang *et al.* concluded that graphene under ambient conditions acts as a ”near-perfect” reflector in the low-frequency range of terahertz [120]. In their work, they studied a graphene flake with layer thicknesses ranging from 0 to more than 6 layers under illumination of THz generated by a low-temperature grown gallium arsenide (LT-GaAS) photoconductive antenna. The results of this can be seen in Figure 4.1, from which it is evident that they were not able to distinguish the response from the different layers from each other. In addition, they also show comparable signal strengths between a 30 nm gold film and monolayer graphene. Moreover, they find that the near-field reflectivity is found to be independent of the carrier density of the graphene, by back-gating the sample and sweeping the gate voltage from -30 V to 30 V at ambient conditions.

The ability to distinguish different stacking configurations and different amounts of layers has been proven possible in the infra-red region [54, 122], thus the immediate explanation as to why this is not possible in the THz range, must lie in the nature of the low-frequency of THz and the material properties specifically in this range. Lowering the frequency of light causes the light’s wavenumber to shift towards lower values. Initially, at optical frequencies, it is comparable to the in-plane momentum to which the light is scattered by the tip. However, at THz frequencies, the in-plane momentum becomes orders of magnitude higher than the wavenumber. For 1 THz the wavenumber is $k = \frac{\omega}{c} \approx 2 \cdot 10^2$ cm^{-1}, whereas the in-plane momentum of s-SNOM is

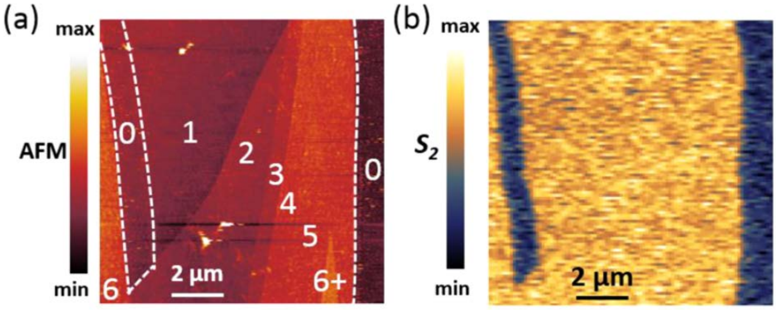

Figure 4.1. Graphene flake ranging from 0 layers to more than 6 layers as seen by (a) AFM and (b) THz-SNOM. Reprinted with permission from [120]. Copyright 2023 American Chemical Society.

$q \sim 1/R = 2 \cdot 10^4$ cm^{-1} for a 50 nm tip radius. This fact suggests the need to include non-local effects, which means the properties of a material are no longer invariant to the momentum, whereas for visible and near-IR frequencies these effects are usually disregarded.

Zhang *et al.* accounts for this by modelling the conductivity of graphene employing random phase approximation (RPA), as

$$\sigma(\omega, q) = \frac{ie^2\omega}{q^2}\Pi(\omega, q), \tag{4.1}$$

where e is the electron charge and $\Pi(\omega, q)$ is a 2D polarisability function dependent on the frequency ω, the momentum q, and the Fermi distribution in the graphene [123]. This description of the non-local conductivity in graphene does have a closed form for zero electron interactions and at temperature ($T = 0$) K. However, in the later sections we will see the non-local conductivity described differently, derived from the semi-classical Boltzmann transport equation under the Bhatnagar-Gross-Krook (bgk) model [124].

As described previously in chapter 1, the near-field reflection coefficient is what yields contrast in s-SNOM measurements. Thus, examining the reflection coefficient can provide insights into the expected contrast from or between materials.

From Eq. (1.24), we recall that the reflection coefficient can be written as,

$$\beta(\omega, q) = \frac{\varepsilon_2 - \varepsilon_1\frac{k_{2,z}}{k_{1,z}} + \frac{\sigma_s k_{2,z}}{\varepsilon_0\omega}}{\varepsilon_2 + \varepsilon_1\frac{k_{2,z}}{k_{1,z}} + \frac{\sigma_s k_{2,z}}{\varepsilon_0\omega}}. \tag{4.2}$$

Using Eqs. (4.1) and (4.2), Zhang *et al.* calculate the reflection coefficient for different sample constructions, Fermi energies, and temperatures. The results of this can be seen in Figure 4.2.

The vertical dashed line in Figure 4.2 indicates the inverse radius approximation $q \sim 1/R$ of the in-plane momentum, and from this it is evident that the reflection

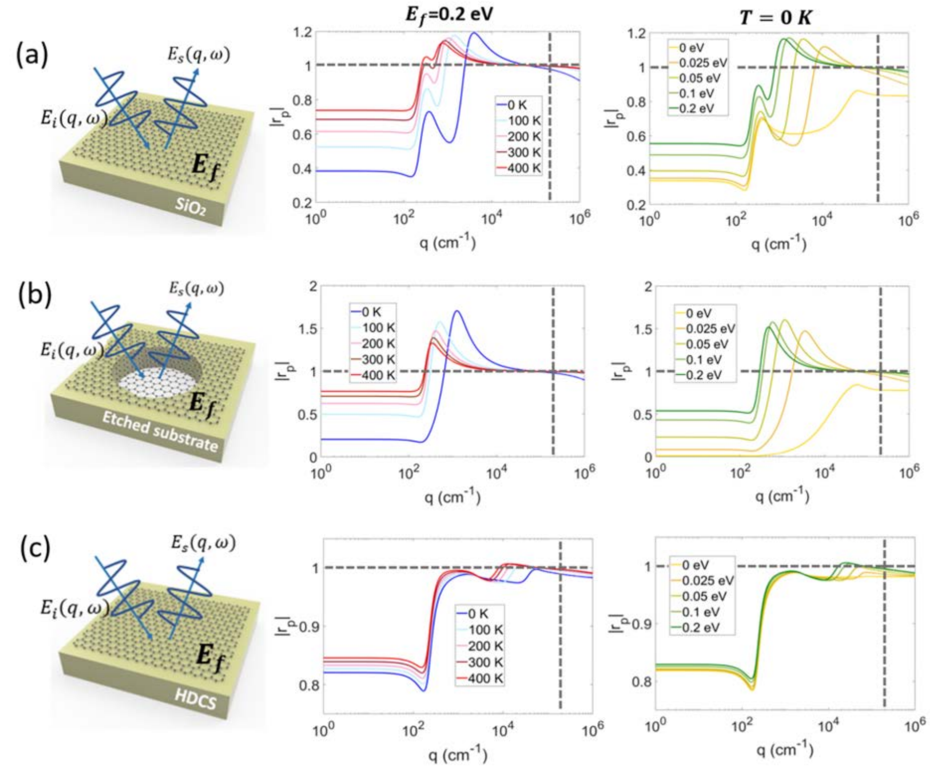

Figure 4.2. Non-local calculated reflection coefficient for (a) graphene in an SiO_2 substrate, (b) suspended in air, and (c) on a high dielectric constant substrate ($\varepsilon = 100$) at 1 THz. Reprinted with permission from [120]. Copyright 2023 American Chemical Society.

coefficient ($r_\mathrm{p} = \beta$) is unity, unless approaching cryogenic temperatures, for a typical Fermi energy of $E_\mathrm{F} = 0.2$ eV. At zero temperature ($T = 0$ K) we start to see a reflection coefficient that deviates slightly from unity when lowering the Fermi energy down to intrinsic graphene.

Note 1 Typical values of graphene

Exfoliated single-layer graphene on a standard SiO_2/Si substrate under ambient conditions typically displays a carrier concentration of $n \approx 10^{12}$ cm^{-2} and a mobility of $\mu \approx 3000 - 5000$ cm^{2}V^{-1}s^{-1}. Such a carrier concentration corresponds to a Fermi energy of $E_\mathrm{F} = \hbar v_\mathrm{F}\sqrt{\pi|n|} \approx 0.11$ eV and the mobility corresponds to a carrier scattering time of $\tau \approx 33 - 55$ fs, a mean free path of $\lambda_\mathrm{mf} \approx 33 - 55$ nm, and a DC conductivity $\sigma_\mathrm{dc} \approx 0.42 - 0.71$ mS [125, 126].

Later in 2019, Yao *et al.* studied OPTP near-field dynamics in an InAs-graphene heterostructure, where they draw similar conclusions: Graphene, in the near-field, acts as a ”near-perfect” reflector, thus shielding any THz dynamics directly under the graphene [121]. These near-field studies of graphene using THz suggest that the use of THz-SNOM for characterising highly conductive surfaces has, to some extent, reached a standstill. This is because graphene of any quality tends to yield the same response in such analyses.

4.1.1 Local and non-local conductivity of graphene

Conductivities at low-frequency, such as the THz range available in our system (up to 2 THz), are typically described with the Drude model, but a more intricate model which relates macroscopic observables (like the conductivity) to microscopic properties using linear response theory is the Kubo formalism. Using the Kubo formalism to describe the intraband conductivity of graphene in the local limit, which is the dominant term in the full conductivity description $\sigma = \sigma_{\text{inter}} + \sigma_{\text{intra}}$ in the low-frequency range, the intraband conductivity can be written as [127],

$$\sigma_{\text{intra}}(\omega) = \frac{2k_B T e^2 \tau}{\pi \hbar^2} \ln\left(2\cosh\left[\frac{E_F}{2k_B T}\right]\right) \frac{1}{1 - i\omega\tau} \, , \tag{4.3}$$

where E_F is the Fermi energy, τ is the electron scattering time, T is the temperature, e is the electron charge, and k_B is the Boltzmann constant. In the low temperature limit, i.e., $E_{\text{F}} \gg k_B T$, Eq. (4.3) reduces to a Drude-like shape of [127, 128],

$$\sigma_{\text{intra}}(\omega) = \frac{e^2 E_F \tau}{\pi \hbar^2 (1 - i\omega\tau)}. \tag{4.4}$$

Since graphene typically displays doping levels of $E_F \sim 0.1$ eV due to the presence of the substrate, then for room temperature, $k_{\text{B}}T \approx 26$ meV, the low-temperature approximation is reasonable.

Figure 4.3(a) shows the local response where the real part of the conductivity decreases when increasing the frequency from its largest value at DC, and the imaginary part starts to increase. As expected, this trend is very similar to a Drude response for metals. But as we have discussed previously, due to the large disparity between the wavenumber of the light and the in-plane momentum, it appears non-local effects need to be considered. Following the Kubo formalism it is indeed possible to describe the momentum dependent conductivity, i.e., non-local conductivity. This is done through the polarisability, which is also called the density-density response function or Lindhard function [111, 128]. This is exactly the model Zhang *et al.* used seen in Eq. (4.1). The polarisability is a complicated function, but at zero temperature, it can be described in a closed form. The polarisability changes depending on which region within a momentum-energy space one reside for graphene [120,128]. However, another approach to describe the non-local conductivity in graphene is from the semi-classical

Boltzman transport equation, which Lovat *et al.* used to describe the non-local intraband transverse and longitudinal conductivity of graphene nanoribbons [129]. In their work, they derived analytical expressions of the intraband conductivity tensor, derived from the semi-classical Boltzmann transport equation under the relaxation-time approximation and the Bhatnagar-Gross-Krook (bgk) model [124] that assures local charge conservation. From this, they found that the transverse and longitudinal conductivity can be expressed as,

$$\sigma_T^{(bgk)}(q,\omega) = \gamma \frac{2\pi\alpha}{v_F^2 q^2}(1-\chi) \ , \tag{4.5}$$

$$\sigma_L^{(bgk)}(q,\omega) = \frac{v_F}{2\pi\gamma_D(1-\chi)+v_F\chi}\sigma_T^{(bgk)}, \tag{4.6}$$

with,

$$\chi = \sqrt{1-\frac{v_F^2 q^2}{\alpha^2}} \ , \tag{4.7}$$

$$\gamma = i\frac{e^2 k_B T}{\pi^2\hbar^2}\ln\left[2\left(1+\cosh\left(\frac{E_F}{k_B T}\right)\right)\right] \ , \tag{4.8}$$

$$\gamma_D = -i\frac{v_F}{2\pi\omega\tau} \ , \tag{4.9}$$

$$\alpha = \omega + i/\tau \ . \tag{4.10}$$

Using the approach derived by Lovat *et al.*, we circumvent to need for zero temperature. Furthermore, comparisons with tight-binding calculations showed good agreement with their model.

Figure 4.3(b) shows the conductivity calculated from Eq. (4.6), where upon comparison with the conductivity calculated in the local regime we observe a drastic change, in which the maximum shifts to a higher frequency and the conductivity drops to zero at DC. Figure 4.3 shows the impact of the high in-plane momentum on the conductivity, further solidifying the need to account for non-local effects. Additionally, a significant correlation is observed between the conductivity and the carrier concentration, as seen by its dependency on the Fermi energy.

Note 2 Conductivity representation of multilayer graphene

In lack of a more precise representation, multilayer graphene can be described as being proportional to the conductivity of monolayer graphene as,

$$\sigma_N = N\sigma_{\text{graphene}} = N\sigma_{\text{intra}}(\omega,q), \tag{4.11}$$

where N is the number of layers. Though this is a crude simplification, DC measurements of conductivity in multilayer graphene show a similar trend [130].

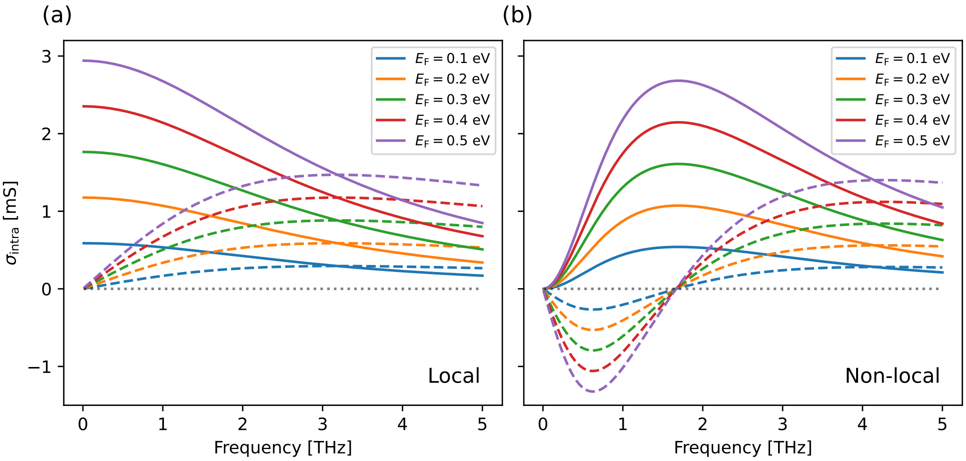

Figure 4.3. Conductivity calculated for a range of different Fermi energies for (a) the low temperature approximation of the local Kubo intraband conductivity and (b) non-local intraband conductivity derived from the semi-classical Boltzmann transport equation with bgk correction. The solid lines correspond to the real part of the conductivity $\mathrm{Re}(\sigma_{\mathrm{intra}})$ and the dashed lines correspond to the imaginary part $\mathrm{Im}(\sigma_{\mathrm{intra}})$. Values used are $\tau = 50$ fs, $v_F = 10^6 \ \frac{\mathrm{m}}{\mathrm{s}}$, $q = 1.42 \cdot 10^5$ cm^1, and $T = 300$ K.

Since these equations govern the response of monolayer graphene, then to examine the predicted contrast between graphene and multilayer graphene, we employ a simple approximation based on the intraband conductivity of graphene from Eq. (4.6). Thus, we approximate bilayer graphene to be twice as conductive as graphene and trilayer to be thrice as conductive, etc. It is important to note, that this is a stark simplification in lack of a better representation, since it is well known that the material properties of graphene change when increasing the number of layers [131, 132]. Thus, this approximation might overestimate the conductivity of few-layer graphene, though DC measurements show similar linear trends| [130]. Nonetheless, a change in the Fermi energy can then be viewed as a change in amount of layers.

Utilising the analytical form in Eq. (4.6), we can visualise the near-field reflection coefficient as a function of the in-plane momentum for different Fermi energies, and by that extension different layers, which can be seen in Figure 4.4. This figure shows similar trends as seen from Figure 4.2, where for high in-plane momenta the reflection coefficient approaches unity for all Fermi energies. For an in-plane momentum of $q = 1.42 \cdot 10^5$ cm^{-1}, which corresponds to a tip radius of 50 nm as per the weighted in-plane momentum distribution from the FDM as discussed in chapter 1, we see that the difference between a perfect reflector and undoped graphene ($E_F = 0$) is less than 3%, strengthening the prediction of no visible contrast between different layers in graphene.

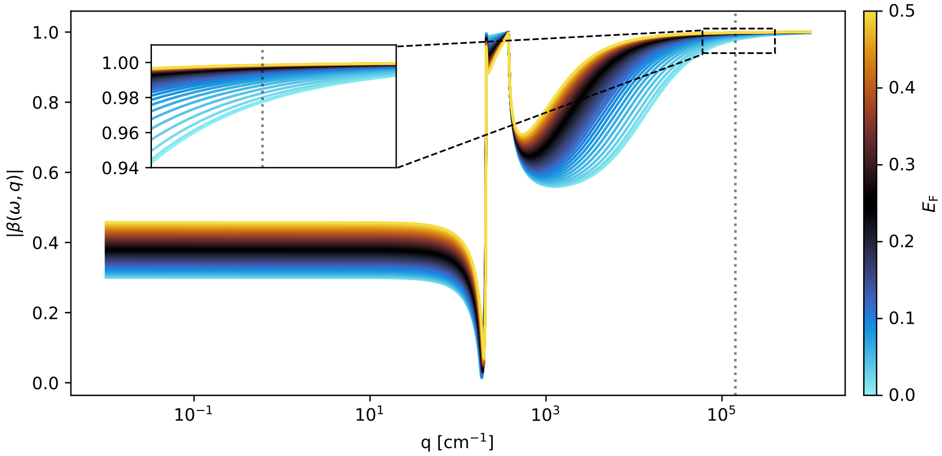

Figure 4.4. Predicted near-field reflection coefficient as a function of the in-plane momentum q by the Lovat model, for a range of Fermi energies. The vertical dashed line shows the expected in-plane momentum in the system for a 50 nm tip radius of $q = 1.42 \cdot 10^5$ cm^{-1} calculated from the momentum weight distribution for the FDM. Parameters used in this calculation are $\tau = 50$ fs, $\nu = 1$ THz, $\varepsilon_{\mathrm{subs}} = 3.80$, $T = 300$ K, and $v_F = 10^6 \ \frac{\mathrm{m}}{\mathrm{s}}$

4.1.2 Finite dipole model predictions

Until now, we have focused solely on the near-field reflection coefficient as a function of the in-plane momentum, without taking into account the tip-sample interactions. Given that the near-field reflection coefficient is the primary determinant of material contrast, this approach has been sufficient in most cases. However, we have yet to investigate the conductivity threshold at which a surface becomes a perfect reflector. As observed, incorporating non-local effects significantly impacts conductivity in the THz range, leading to a shift in the Drude weight from DC to a finite frequency. Therefore, by investigating the near-field response for various conductivities based on the FDM, we can assess the potential for obtaining measurable contrast.

By examining the scattering ratio $\eta_m = \frac{\sigma_{m,\mathrm{sample}}}{\sigma_{m,\mathrm{substrate}}}$, we simply sweep a wide range of conductivities. This approach enables us to determine the point at which a material becomes a perfect conductor, independent of specific material models. Consequently, it allows us to evaluate not just the appearance of graphene but that of any conductive surface.

Figure 4.5 shows the scattering ratio as a function of conductivity from 10^{-6} S to 0.1 S for the PDM and FDM. The calculation was performed with a frequency $\nu = 1$ THz, an in-plane momentum of $q = 1.42 \cdot 10^{-7}$ m^{-1}, a half-length of $L = 600$ nm, fraction of induced charge $g = 0.7$, tip radius of $R = 50$ nm, and a tapping frequency of $\Omega = 80$ kHz. The substrate is modelled as a 90 nm SiO$_2$ layer on a Si wafer. From

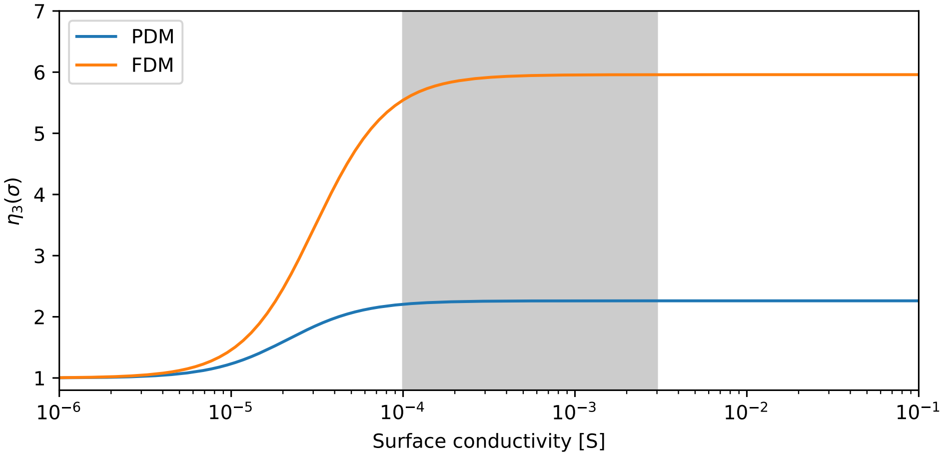

Figure 4.5. Scattering ratio η for the $m = 3$ harmonic as a function of the conductivity for the PDM and FDM. The grey area represents the range for typical values of conductivity for graphene.

Figure 4.5 it is clear that the FDM predicts a significantly larger scattering ratio than the PDM, however, both models follow the conclusions drawn earlier. That is, no contrast between different conductivity values within the grey area and above. For the FDM we see that for the threshold is slightly higher than for the PDM, but with typical DC conductivity values for graphene and metal films this still falls out of the contrast window. However, despite previous experiments and theoretical predictions suggesting no contrast in graphene, we will demonstrate in the forthcoming sections that significant contrast can be measured, not only between different layer amounts but also within the same layer.

4.2 Exfoliated graphene

In this section, we will see how exfoliated graphene of different layer amounts appear in our system and how we indeed are able to distinguish contrast in the conductivity of exfoliated graphene.

4.2.1 Sample preparation

The graphene samples we investigate were prepared by our collaborators at DTU Physics (Leonid Iliushyn, assoc. prof. Timothy J. Booth, and prof. Peter Bøggild) through mechanical exfoliation of graphite (NGS Naturgraphit GmbH). The exfoliation is performed on a standard Si wafer with a 90 nm SiO_2 layer, unless otherwise specified. This exfoliation results in a wide range of flakes ranging from purely monolayer graphene flakes to flakes with multiple layers, all on the same substrate. Optical microscopy, performed by Leonid Iliushyn, was used to identify suitable monolayer and few-layer flakes on the surface, and to assess the number of graphene layers on a given sample based on the optical contrast [133, 134].

4.2.2 Contrast between graphene layers

In this study, we systematically analyse a diverse array of graphene flakes. Our study encompasses a spectrum of conditions: from flakes located on a unified substrate to those positioned on an identical substrate and exfoliated concurrently, extending to flakes positioned on substrates with a different thicknesses of 300 nm of SiO_2 and exfoliated on separate days. A summary of some measurements can be seen in Figure 4.6, where the optical microscope image is shown on the left and the corresponding THz whitelight scan for the $m = 2$ harmonic is shown on the right. Flakes, (a), (c), and (e) are all from the same substrate, whereas (g) is from a sample with a 300 nm SiO_2 on Si substrate with Au connector arrays running parallel across the substrate. The flakes in Figure 4.6(a) and (g) are single crystal with mainly monolayer, bilayer and trilayer areas, whereas Figure 4.6(e) is a monolayer flake where another flake has been randomly been placed on top during the mechanical exfoliation process. Figure 4.6(c) is a monolayer flake where a strip has been ripped up and then folded across the flake.

It is evident from the whitelight images that the layers identified in the optical microscope images are clearly distinguishable, with an increase in layer yielding an increase in scattered signal. Horizontal bands on whitelight images are not attributed to a variation in conductivity, but rather attributed to be an artefact, since it co-aligns with the scanning direction and stretches across the entire row. Examples of this are visible in the bottom of Figure 4.6(b) and near the bottom of the graphene flake in Figure 4.6(f).

In Figure 4.6(h), we see a clear reproduction of the edge going from monolayer to trilayer, as well as the irregular shaped edge going from trilayer to bilayer and back to trilayer again. More interestingly, we see patches within the bilayer region which have an overall decrease in scattered signal. The origin of this still remains to be determined, however, one can speculate as to whether structural changes within the bilayer configuration could lead to a decrease in scattered signal and therefore conductivity, or whether some contaminant not visible in the optical microscope effectively lowers the scattered signal. Further investigation into this is necessary.

On several substrates, the presence of Au particles are observed, attributable to minor contamination during the wafer preparation process, even within a controlled clean room atmosphere. Such a particle is visible in Figure 4.6(a), where the graphene appears to conform around the particle, lying on top of it. A similar scenario is observed in Figure 4.11(c), showing an Au particle under the monolayer graphene. It is crucial to note that the existence of the Au particle does not impact the conclusion drawn from Figure 4.6(b), which is layer contrast. Polymer residuals from the transfer

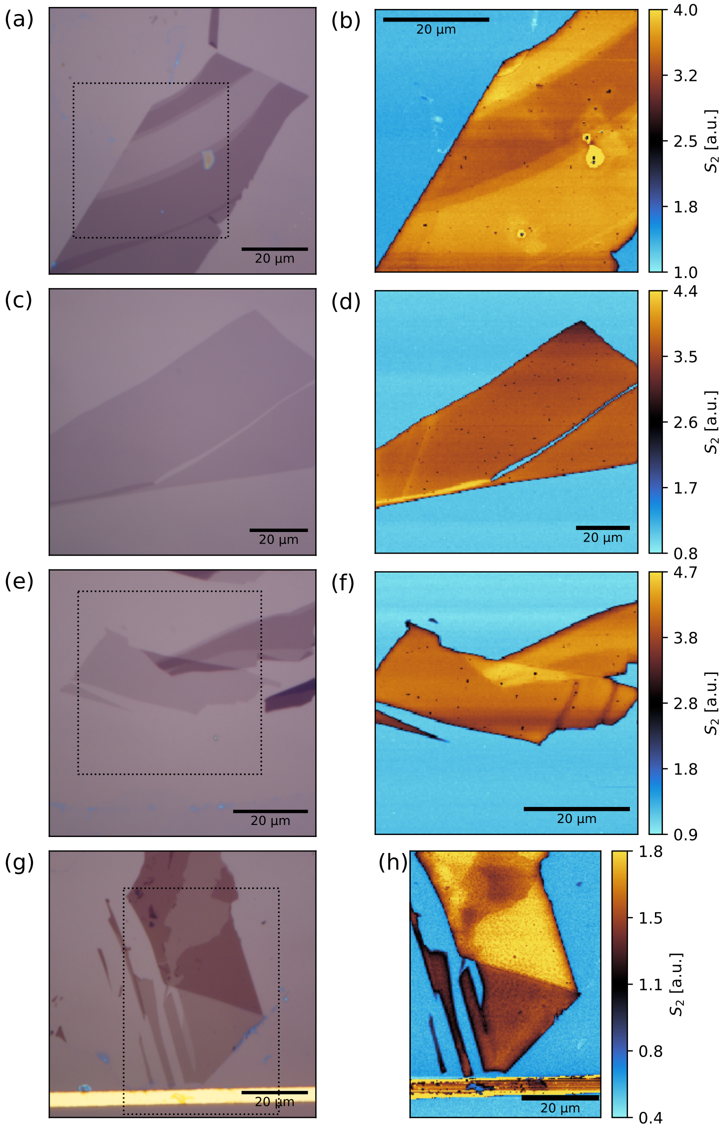

Figure 4.6. (a), (c), and (e) Optical microscope images of graphene layers, ranging from 0 layers (0L) to 6 layers (6L), on a standard substrate, where (b), (d), and (f) are their corresponding whitelight maps for the $m = 2$ harmonic. (g) and (h) are the optical microscope image on a 300 nm SiO_2 on Si wafer with gold (Au) stripes, and the corresponding whitelight map. The dotted boxes on (a), (e), and (g) indicate the area of whitelight maps.

process are visible in a blue shade around the graphene flakes on multiple substrates, which is evident in Figure 4.11.

Figure 4.6 is in stark contrast to what Zhang *et al.* saw in their experiment shown in Figure 4.1 and what the theory (both local and non-local) predicts. It is evident that we are able to resolve the layer amounts which has previously been demonstrated impossible. The quality of the graphene studied would be the first point of comparison between the two results. The graphene used in our experiments is assumed to fall within reasonable distance to standard exfoliated graphene with a moderate doping level due to the substrate. However, it was claimed that the lack of contrast was independent of carrier concentration studied through back gating [120]. Thus, the quality of the graphene should not impact whether contrast is visible or not.

Figure 4.4 indicates a potential minor percentage difference in the reflection coefficient at our expected in-plane momentum, however, moving slightly down in in-plane momentum results in a significant difference in the reflection coefficient between the different Fermi energies. This observation suggests that the actual operational in-plane momentum could be lower than initially estimated. As explained in chapter 2, we dent our tips in order to increase the signal-to-noise ratio, while compromising with a lowered spatial resolution. However, in many cases, though denting the tip results in an increase in signal, the loss of spatial resolution is kept remarkably low. Approach curves performed on graphene with a dented tip support this fact as shown in Figure 4.7, where the e^{-1} decay length estimates the field confinement and by that extend the spatial resolution [62]. Here we see an estimated spatial resolution of 25 nm for the $m = 2$ harmonic for the given tip.

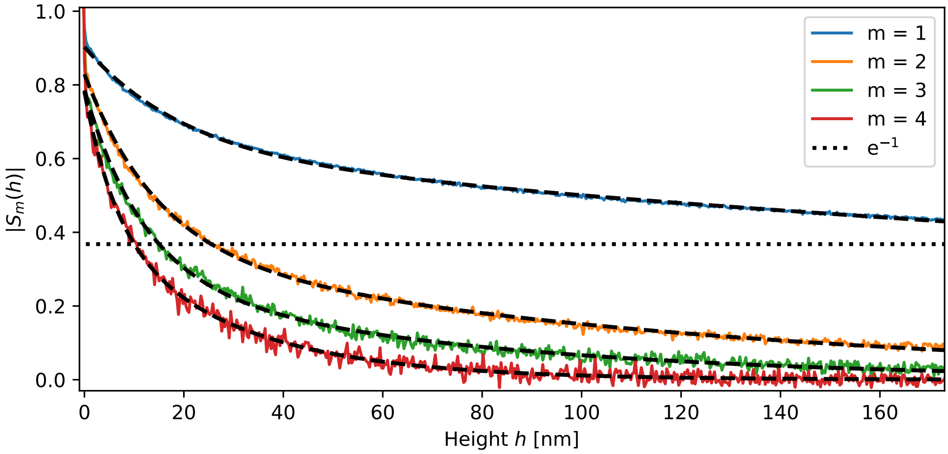

Figure 4.7. Experimental approach curves from monolayer graphene for the $m = 1, 2, 3, 4$ harmonic orders, where the dotted line indicates the e^{-1} decay length indicative of the spatial resolution. The dashed line on each approach curve in a double exponential fit.

The denting of the tip, however, is not attributable as the cause of the contrast observed between graphene layers, as evidenced by the visibility of contrast even brand new, non-dented tips. For instance, Figure 4.6(h) shows clear layer contrast obtained using a non-dented tip, in contrast to other white-light images performed using dented tips. Nonetheless, it may be that the tip itself is a determining factor in whether the contrast is visible or not.

4.2.3 Impact of AFM tip on contrast

In some cases, we are not able to distinguish between the different layers of graphene as shown in Figure 4.9(a), where the response appears to be uniform across the graphene. A subtle indication of a boundary appears to be present, but its clarity is considerably diminished compared to previous demonstrations. An optical microscope image of the whole graphene sample is shown in Figure 4.8 with the smaller and larger squares indicating the whitelight images shown in Figure 4.9 and Figure 4.10, respectively.

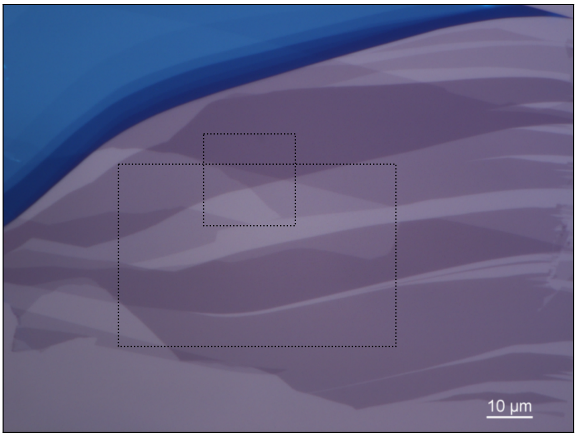

Figure 4.8. Optical microscope image of a graphene sample consisting of multiple layers ranging from one layer to four layers. The dashed squares indicates the locations of the performed whitelight scans.

Figure 4.9(b) shows the whitelight response of the same area after denting the tip. We observe a pronounced increase in signal intensity from both the graphene and the substrate. This observation aligns with expectations, attributed to the effective increase of the scattering area of the tip. Furthermore, we observe what appears to be a decrease in spatial resolution, since the edges appear more blurry than before denting, which is well within expectations. Subsequently, this enhancement in signal intensity facilitates differentiation between the layers, as indicated by the two small dashed lines.

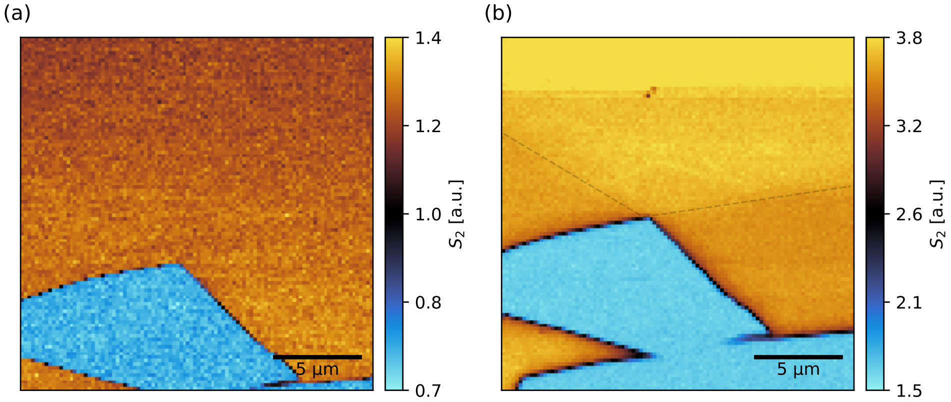

Figure 4.9. Whitelight images of (a) a non-dented tip and (b) the same tip but after denting, for the $m = 2$ harmonic.

A large area whitelight scan of the sample can be seen in Figure 4.10, performed with the dented tip. Here the contrast between the layers in the region from Figure 4.9 is significantly more pronounced as well as layer borders further away. On comparison with the optical microscope, we see that all layer borders are identifiable on the large area whitelight scan.

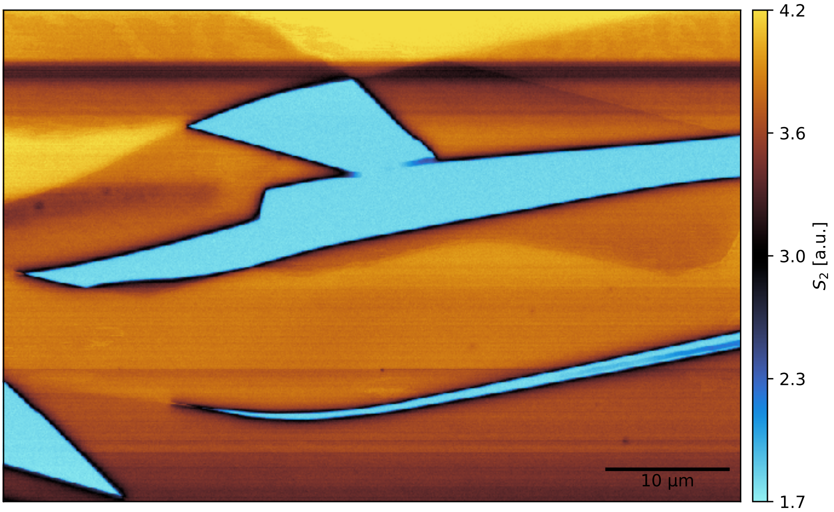

Figure 4.10. Large area whitelight scan capturing multiple borders between regions of different layers of graphene. Horizontal bands of decreased signal is attributed to scanning artefacts.

From this, it is inferred that the denting of the tip results in an enhancement in the observable contrast between the graphene layers. This enhancement could be attributed to either a reduction in the in-plane momentum caused by the denting or due to a substantial amplification in signal, which eases the distinction of a minimal percentage difference in the signal. The definitive factor responsible for this observation, however, remains to be determined.

4.2.4 Contrast within monolayer graphene

So far, we have seen that contrast between layers of graphene, contrary to previous results, indeed is possible. However, not only is contrast between layers possible to observe but also contrast within a given layer. This fact was seen in Figure 4.6(h), where a decrease in signal was observed in bilayer graphene. Figure 4.11 shows mainly monolayer graphene flakes, where the whitelight image shows contrast within the flake itself.

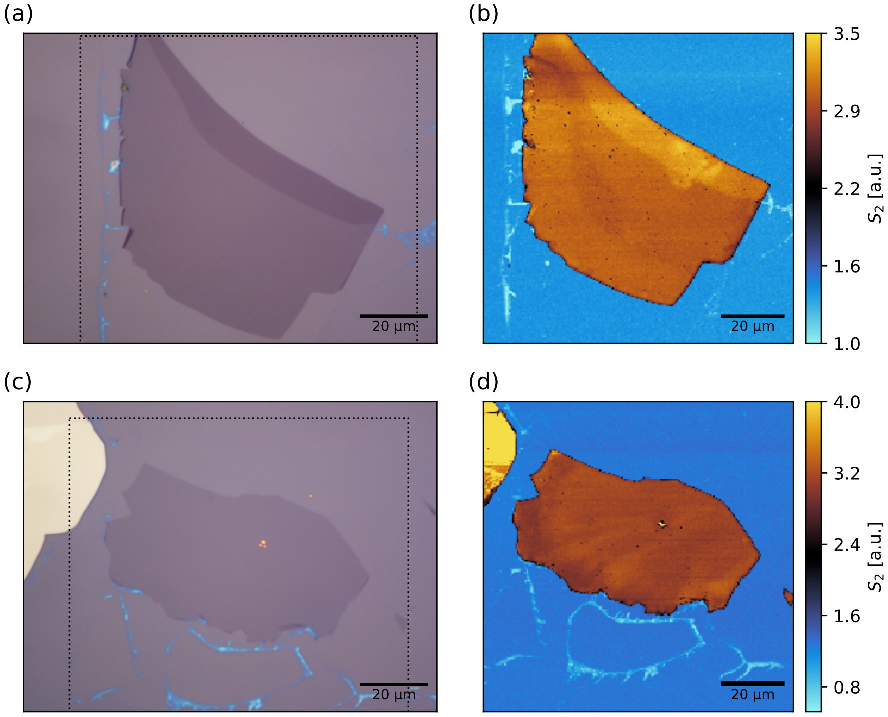

Figure 4.11. Optical microscope images of a monolayer flake with a bilayer edge at the top in (a) and a purely monolayer flake in (c), with (b) and (d) being the corresponding whitelight images.

The structure of the contrast in the two flakes differ significantly. In Figure 4.11(b), we observe a band flowing across the middle of the flake, whereas in Figure 4.11(d) the contrast we observe shows more resemblance to eroded landscape features on an island.

The origin of this contrast still remains to be determined, however, the expected difference in material properties that this contrast would indicate is expected to be quite minute, since no apparent defects or contamination are visible on the optical microscope image. This would suggest that the THz signal at the nanoscale is remarkably sensitive to changes in the material properties of graphene.

4.2.5 Spectral response of exfoliated graphene

To delve deeper into the apparent contrast between graphene layers, we conduct a comprehensive spectroscopic analysis across these layers. This is to determine if the contrast exists within the spectrum itself and not solely in the whitelight, which represents an averaged spectral response. We perform a 30 µm line scan across different layer amounts starting on the substrate with a step size of 200 nm and 3 time trace averages at each pixel. An example of the response from the substrate and graphene is shown i Figure 4.12(b) and (c). The reference for the whole line scan is formed by averaging the 10 first traces from the substrate.

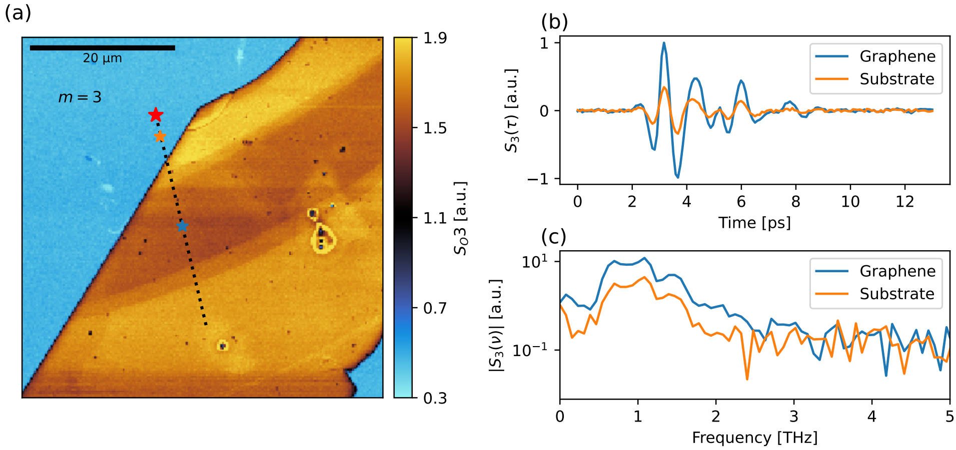

Figure 4.12. (a) Whitelight image of a sample with 1-3 layers of graphene distinctly distinguishable for the $m = 3$ harmonic, where the dotted line indicates where a TDS line scan was performed. The red star indicates the starting position. (b) Example of the time domain signal for the $m = 3$ for graphene and the substrate. Positions are shown in (a). (c) Corresponding spectra of the time pulses.

The full spectroscopic line scan is summarised in Figure 4.13 for the third-order signal, where we have limited the spectrum to span from 0.5 THz to 1.5 THz, due to the significantly lower signal elsewhere.

We clearly observe a significant increase in signal moving from the substrate to graphene. However, we are not able to clearly distinguish the boundaries between each region of layers. A minor increase in peak intensity is noted when comparing responses from the monolayer region to the last trilayer region; however, a definitive boundary is not discernible. Moreover, despite expecting the spectral response to be rather featureless, due to the spectral response of the conductivity of graphene, we observe significant variation during the line scan. The spectral response appears uniform until around 17 µm, where an increase at 0.8 THz and a decrease at 1.3 THz start to appear. In the phase we observe similar uniform behaviour until around 17 µm, where for at 1.25 THz a phase shift appears when moving onto graphene, which as the scan progress spread to higher frequencies. When moving back onto trilayer a positive phase shift then appears at 1.25 THz.

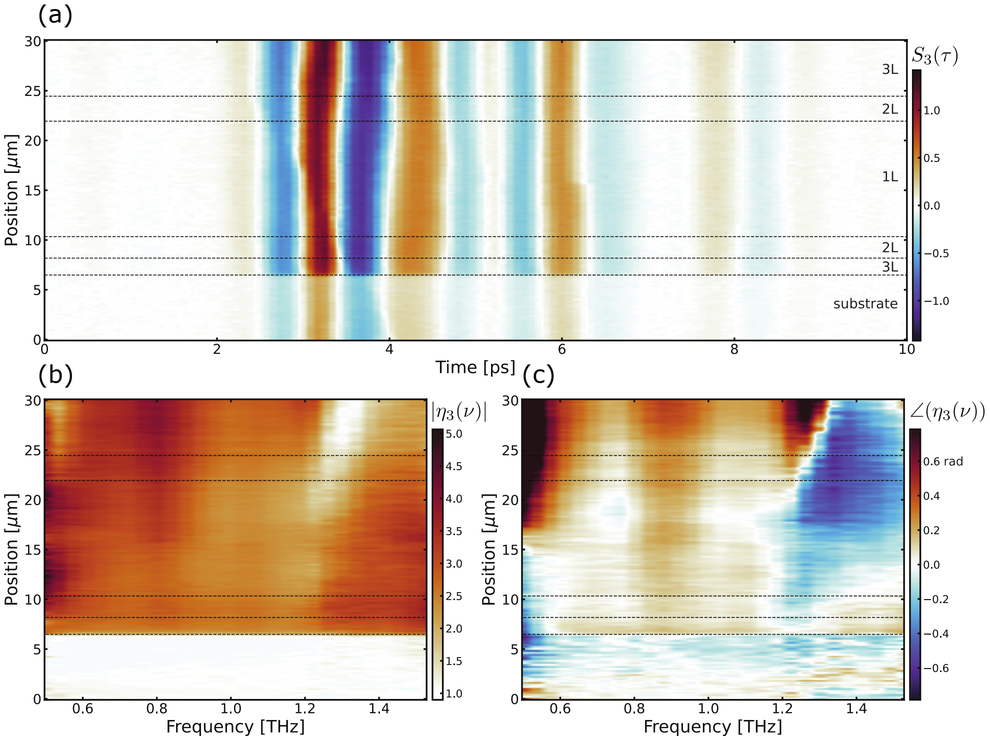

Figure 4.13. Full THz-TDS line scan along the line shown in Figure 4.12. (a) Time traces for the $m = 3$ harmonic, where the dotted lines indicate the approximate location of the borders between the layers. (b) The spectral scattering ratio and (c) the frequency resolved angle of the scattering ratio or phase ratio.

As we have discussed previously, the near-field spectral response is heavily dominated by resonances stemming from the tip shank and cantilever [64]. The frequencies at which the features in the spectral amplitude appear coincides with the frequencies of the resonances generated by the tip itself. Due to this, performing quantitative spectroscopy at the nanoscale is exceedingly difficult with the current tip technology. A way to suppress the resonances formed by the geometric nature of the AFM probes used must be devised in order to perform true quantitative spectroscopy at the nanoscale in the THz region.

4.2.6 FEM simulations

It has been surprising to observe that, contrary to previous experiments and theoretical predictions (including both local and non-local responses) related to graphene, we are in fact capable of distinguishing between graphene layers through whitelight scans. Given that state-of-the-art theoretical models fall short in explaining this contrast, we resort to utilising Finite Element Method (FEM) simulations to investigate whether the observed contrast is intrinsically linked to fundamental electromagnetic interactions. We model the tip as an elongated sphere, identical to the FDM depiction as previously done. The graphene was modelled as an infinitely thin layer between a 90 nm SiO_2 layer on Si substrate and air. The tip was modelled with a major semi-axis length of $L = 40$ µm and a tip radius of 50 nm, and the material was chosen to be a Drude metal with typical values of conductivity.

A tapping cycle from monolayer graphene is shown in Figure 4.14(a) with the resulting approach curves shown in Figure 4.14(b). This can be compared to how the FDM predicts the tapping cycle and corresponding approach curves shown in Figure 4.14(c) and (d). It is clear that FEM simulations and FDM predictions show similar trends and similar spatial resolution approximated by the e^{-1} decay length. The FEM approach curves starts at $h = 5$ nm, since that was chosen to be the minimum tapping height to resemble the experiments, whereas for the FDM $h = 0$ nm was chosen. Furthermore, to save computational demand and time, only half the tapping cycle was simulated and the response was mirrored in post processing to perform the demodulation, as well as only performing simulations in a 2D space as previously discussed.

A single simulation point (one height h, one frequency ω) requires 10-15 s of simulation time, leading to a run time of approximately 200 s for the simulation of a full tapping cycle on a desktop computer (Intel i9-11900K, eight physical cores, 128GB memory).

To simulate the response of graphene we sweep a range of frequencies (0.2 THz - 2 THz) across a strip of graphene. We vary whether it is monolayer, bilayer, etc. by scaling the conductivity as, $\sigma_N(\omega) = N\sigma_{\mathrm{intra}}(\omega)$, as mentioned earlier.

The spectral results of simulating monolayer graphene and bilayer graphene are shown in Figure 4.15 for a 50 µm long graphene strip. We can also calculate a frequency averaged spectral scattering ratio to be comparable to the whitelight scan.

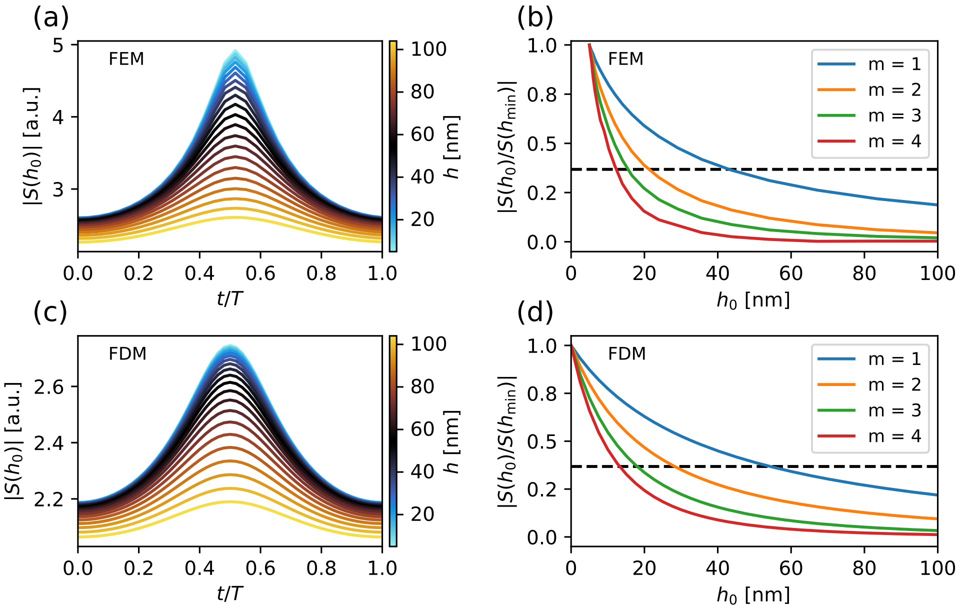

Figure 4.14. (a) Full tapping cycle ranging from 5 nm to 100 nm for FEM and (b) the resulting approach curves for the $m = 1, 2, 3, 4$ harmonics. (c) Full tapping cycle calculated from the FDM and (d) resulting approach curves. The dashed line on the approach curves indicates the e^{-1} decay length, from which an approximate spatial resolution can be estimated.

One can, however, not make a one-to-one comparison between the two, but only a general trend comparison can be made.

From Figure 4.15 we observe a uniform signal across the graphene strip with a slight overall decrease in signal just around the edges, which is comparable to experimental observations. Furthermore, we observe an overall increase in signal between monolayer and bilayer graphene in the spectral amplitude. This is also visible in the frequency averaged spectral amplitude, where monolayer graphene shows a scattering ratio of 5, while bilayer shows a scattering ratio of 6. Moreover, for bilayer graphene in Figure 4.15(b), we observe from the averaged response a slight decrease in amplitude going from positive positions towards negative positions, which is not as evident in the monolayer. This may be related to the fact that the plane-wave is incoming from the negative positions, and thus for the negative positions the far-field reflection would encompass more of the substrate. The tip would then shadow the response on the other side. The evident increase in tilt seen in the bilayer compared to monolayer would then be explained by the overall increase in signal. Figure 4.15(c) and (d) show the corresponding phase difference for monolayer and bilayer, respectively. The overall trend between the two is similar with slightly

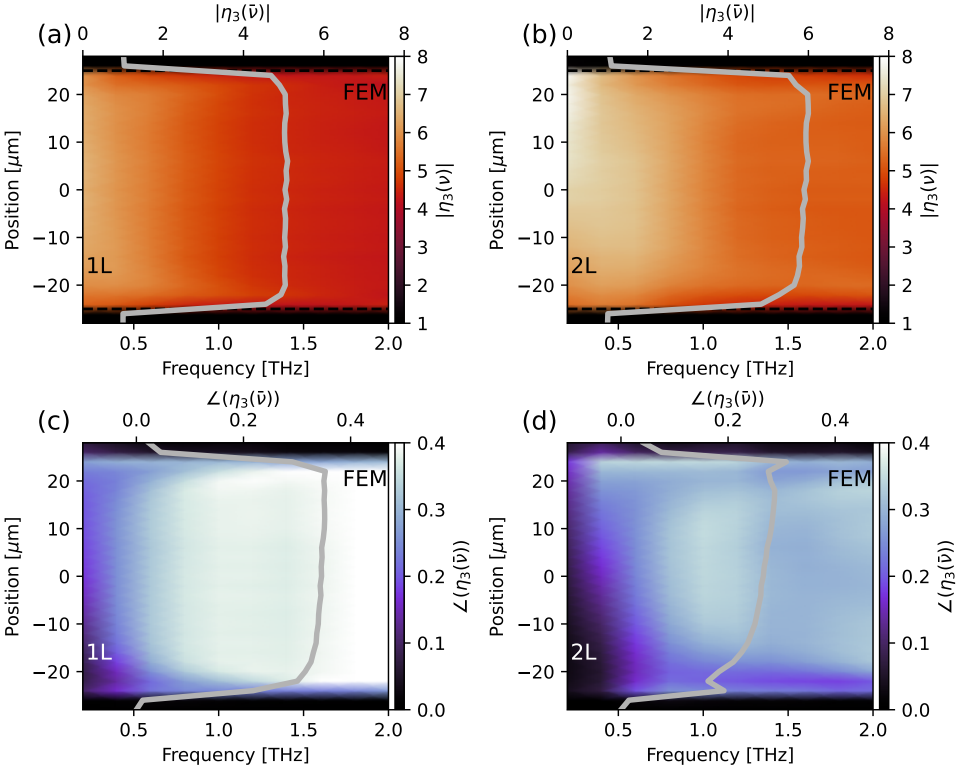

Figure 4.15. FEM simulated spectral amplitude of the $m = 3$ harmonic for (a) monolayer graphene and (b) bilayer graphene. (c) and (d) are the corresponding phase differences for monolayer and bilayer, respectively. The length of the graphene strip is 50 µm and the spectral range is from 0.2 THz to 2 THz. The grey curve indicates the frequency averaged scattering ratio referenced to the substrate.

lower phase shift in bilayer graphene. Around the edges on the bilayer we observe an oscillation which may be related to some plasmonic effect, however, no further investigation of this has been performed. Conclusively, FEM simulations also predict there to be a measurable contrast between monolayer graphene and bilayer graphene.

To further investigate this, we perform simulations where we vary the Fermi energy, which corresponds to varying the conductivity based on Eq. (4.3). The results of this can be seen in Figure 4.16(a) and (b) for a sweep of Fermi energies from 0 eV to 0.4 eV. Figure 4.16(c) and (d) show the predicted response based on the FDM with a local model for the conductivity of graphene, and Figure 4.16(e) and (f) with a non-local model.

We observe similar behaviour in the phase difference for all three methods, however, in the spectral scattering amplitude we observe large discrepancies between

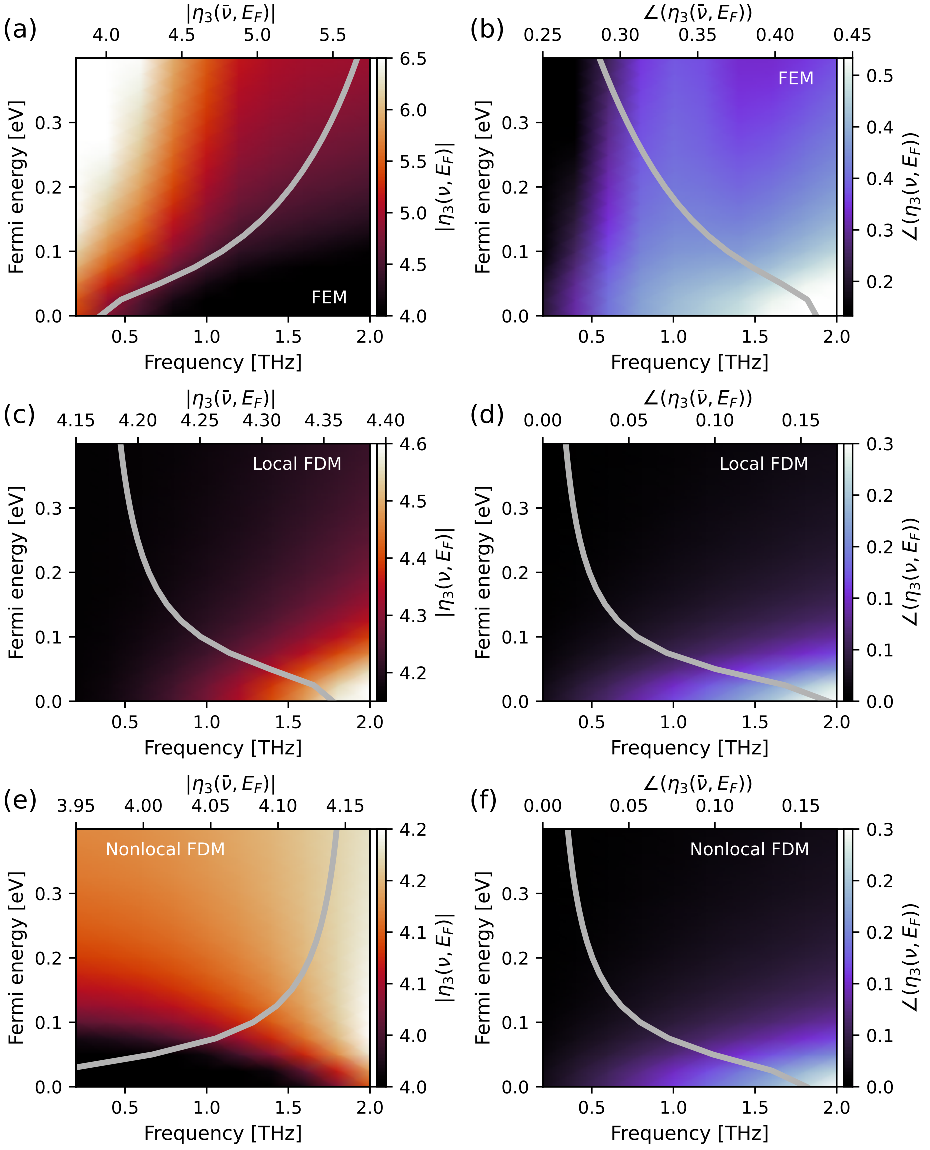

Figure 4.16. Spectrally resolved scattering ratio of monolayer graphene on a SiO_2/Si substrate for (a),(b) FEM, (c),(d) FDM with local response of graphene and (e),(f) FDM with non-local response of graphene. The left column depicts the spectral scattering amplitude with the corresponding phase shown in the right column. The grey line indicates the spectrally averaged scattering ratio.

each method. We observe the spectral distribution to be different in all three cases, however, the frequency averaged response of the non-local FDM model show similar trends as the FEM. Notably, as shown earlier, both the local and non-local FDM predict very little variation in scattering ratio compared to the FEM.

Interestingly, the FEM simulation is based in the local electromagnetic regime with local material models and assuming no dependence on the nearby positions. Therefore, the FEM in a local response predicts a measurable contrast between layers of graphene. Currently, implementing a non-local aspect into the simulation is difficult, since at each node in the spatial domain the response would vary based on the neighbouring nodes and therefore require extensive simulation taking derivatives of the spatial position into account. Nonetheless, we are still able to explain the contrast observed in the experiments with fundamental electromagnetic interactions.

Similar to the analysis of the FDM and PDM where we swept a range of conductivities, thus disregard any material model, we can simulate the same approach. Thus, we vary the conductivity as a free parameter in a range of 10^{-6} S to 0.1 S for graphene, and calculate the scattering ratio. Furthermore, we vary the length of the tip to investigate whether the length has an impact on the contrast, due to its relative size to the THz radiation. Figure 4.17 shows the results compared to the scattering ratio predicted by the PDM and FDM.

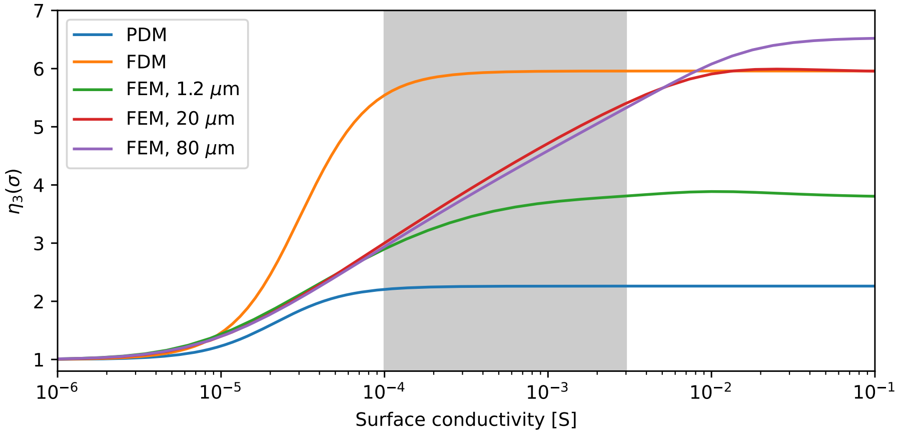

Figure 4.17. Scattering ratio between graphene and 90 nm SiO_2/Si substrate for the PDM, FDM, and FEM with total tip lengths of 1.2 µm, 20 µm, and 80 µm (corresponding to major semi-axis length of 600 nm, 10 µm, and 40 µm) as a function of conductivity. All scattering ratios are for the $m = 3$ harmonic. The grey area indicates typical conductivity values for graphene.

From Figure 4.17 we can conclude that within a typical range of conductivities, we are indeed able to observe contrast. Notably, we also observe that for realistic tip lengths, the scattering contrast only changes slightly, whereas for a tip length of 1.2 µm (major semi-axis $L = 600$ nm), the scattering ratio is significantly decreased, but still shows measurable contrast within the given range. This suggests that there are some dynamics which are not fully captured by the current state-of-the-art theory, being the FDM with a layered structure extension. Whether this is related to the model being fundamentally rooted in electrostatics or that the extension with the infinitely thin conductive layer is insufficient, remains to be determined.

Lastly, we simulate a structure resembling the line scan performed in Figure 4.13, where we move from substrate to trilayer to bilayer onto monolayer and back again, with similar dimensions, in order for the two to be comparable. The results are shown in Figure 4.18.

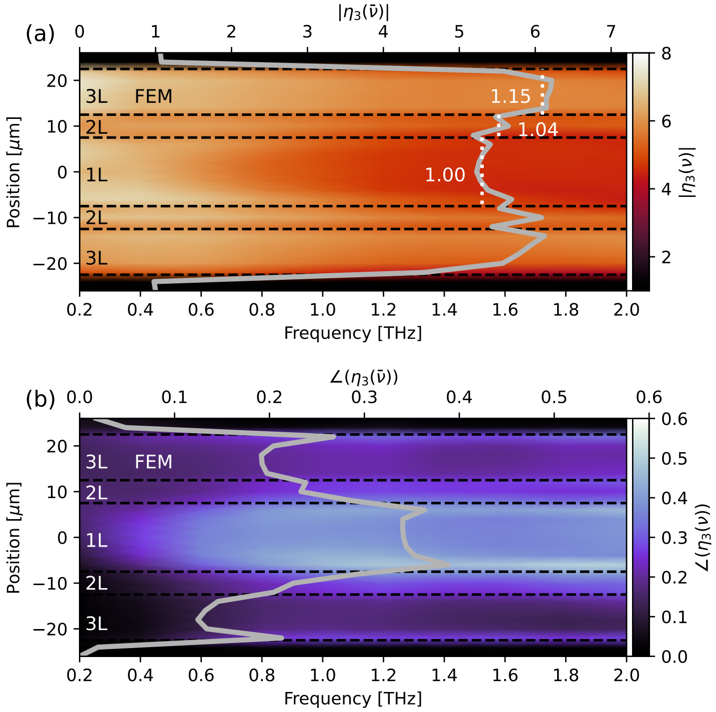

Figure 4.18. (a) Spectral scattering amplitude ratio and (b) corresponding phase difference for the $m = 3$ harmonic for a graphene structure similar to that seen in Figure 4.12(a). The grey curve indicates the frequency averaged scattering ratio.

As earlier, the grey line indicates the frequency averaged scattering ratio, and the white dashed vertical lines we see in Figure 4.18(a) indicates the scattering contrast between the layers with monolayer as the reference. Again, we see a tendency for an increased contrast for the positive positions, which eases the distinction between the layers. Furthermore, the edge effects we have seen when going from substrate onto graphene, where the signal slowly rises to a constant level, are also present at the borders between graphene layers. This could indicate that the edge itself may act as a scattering channel, thus effectively lowering the local conductivity. Figure 4.18(b) shows the phase difference between the substrate and the graphene structure, where similar to Figure 4.15(d), we see edge effects at all boundaries and an overall decrease in phase shift with increasing layer number.

Comparing the contrast that the FEM simulations predict to that of the whitelight image is shown in Figure 4.19. Surprisingly, the scattering contrast is remarkably similar, however, as mentioned before, we cannot directly compare the two. The FEM simulation is a highly simplified model in only being two-dimensional, with the assumption of the conductivity of multilayer graphene, and without a cantilever for the tip. Thus, a one-to-one comparison cannot be made, but only a general trend comparison can be made.

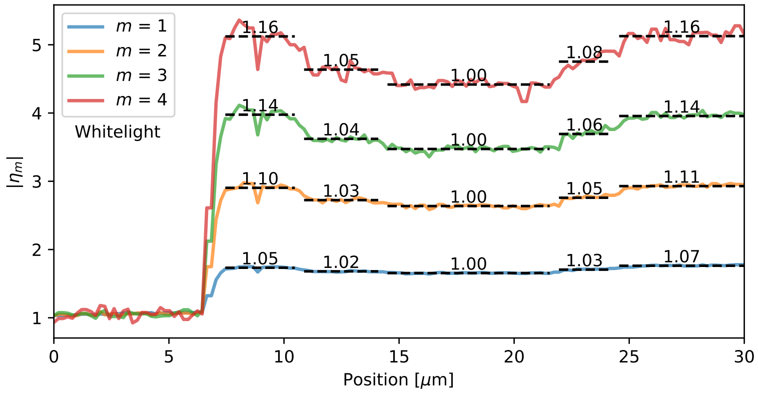

Figure 4.19. Scattering ratio from the whitelight image shown in Figure 4.12(a) along the path of the line scan for the $m = 1, 2, 3, 4$ harmonic orders. The dashed lines indicate the contrast compared to the monolayer scattering ratio.

Based on these studies, we can conclude that the experimental observation of contrast between layers of graphene can be reproduced by local finite-element method simulations without any regard for non-local interactions. This indicates, that the current model for describing the near-field interactions requires improvement to explain the observable contrast.

4.3 Platinum thin-films

In this section we will study the response of platinum (Pt) thin-films and study whether we are able to measure a contrast between different film thicknesses, similar to the graphene layers. The samples we are investigating were prepared by our collaborators at Capres A/S, a KLA company, specifically by Jonas D. Buron.

The original goal was to extract the conductivity and compare it to micro four-point probe (M4PP) electrical measurements performed on the same sample. However, as we have discussed, performing true quantitative spectroscopy with conductive surfaces currently faces many challenges. Thus, were are only able to compare the relative signal between the different thicknesses.

We investigate four different thicknesses of platinum at $d = 15$ nm, 10 nm, 5 nm and 3 nm on high resistivity silicon with no binding layer. The samples were prepared through the use of a shadow mask. AFM images of the four samples are shown in Figure 4.20.

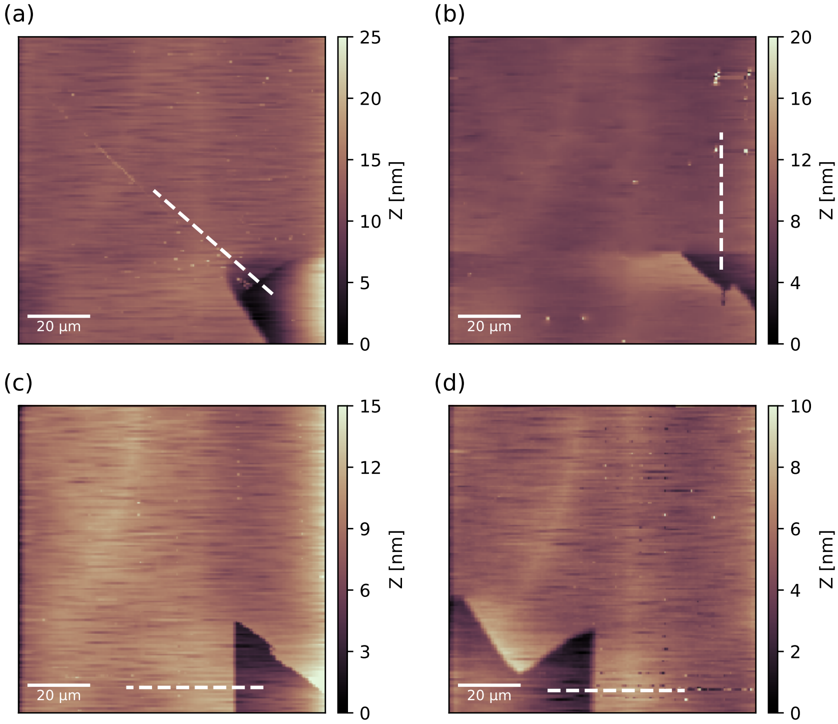

Figure 4.20. AFM image of platinum thin-films of thickness (a) 15 nm, (b) 10 nm, (c) 5 nm, and (d) 3 nm. The white dashed lines indicate the position the TDS line scan as well as the M4PP line scan.

The edge of the larger structure made from a shadow mask varies over hundreds of nanometres, however, during preparation rips occurred all over the structures which resulted in sharp edges being present. These sharp edges are perfect for the high spatial resolution of the THz-SNOM. In addition to performing whitelight scans of the thin-films, we also perform full TDS line scans across the sharp edges, as shown from the white dashed lines in Figure 4.20. From the AFM we also notice damages in the films, which stem from the M4PP line scans, as M4PP is an invasive technique, which has a risk of causing damage adn leaving traces from the measurement. In contrast, THz-SNOM is a non-invasive and thus a promising technique for nanoscale material characterisation for device fabrication.

Figure 4.21 shows the whitelight response for the different film thicknesses, plotted on the same colour scale for better comparison in signal amplitude.

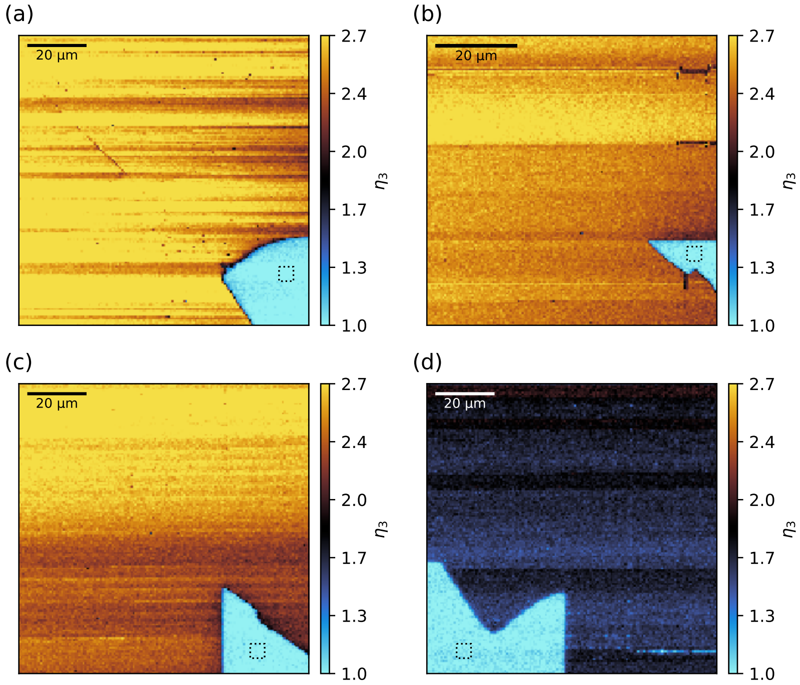

Figure 4.21. Whitelight images of platinum thin-films of thickness (a) 15 nm, (b) 10 nm, (c) 5 nm, and (d) 3 nm for the $m = 3$ harmonic. The black dotted boxes indicate the 5x5 pixel area used as reference for the maps.

In Figure 4.21(a), which is for the $d = 15$ nm thickness, we observe significant horizontal scarring. These most likely arise due to the presence of the M4PP line scan damage we see going diagonally. This caused some particles to protrude and may have made slight contact with the tip causing the rest of the horizontal line to have a decrease in signal.

From Figure 4.21 we clearly observe that going from $d = 15$ nm to $d = 5$ nm does not change the scattering ratio η drastically, however, we observe a drastic change in scattering ratio when approaching very thin films, as visible for the $d = 3$ nm in Figure 4.21(d). It it well known that decreasing the thickness will lower the conductivity, however, when approaching thicknesses below the mean free path, additional scattering boundaries being the interfaces are introduced. Thus, the conductivity does not scale linearly with low thicknesses.

From our observation in the previous section, we saw that above a certain conductivity threshold, the near-field reflection coefficient essentially becomes unity and no contrast will be visible. Figure 4.21 shows a similar trend.

The DC conductivities for the different film thicknesses are extracted through M4PP measurements and the results are shown in Figure 4.22(a), where line scans have been performed.

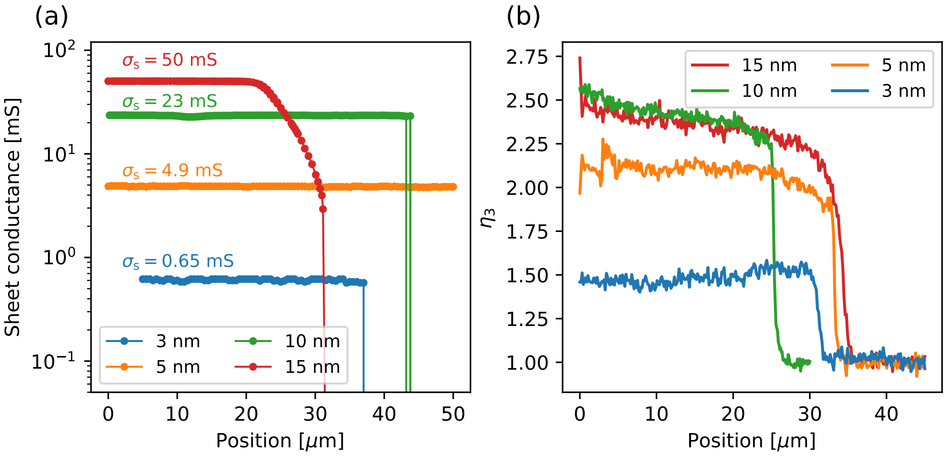

Figure 4.22. (a) Sheet conductance extracted from M4PP line scan and (b) whitelight scattering ratio for the $m = 3$ harmonic extracted from full TDS line scan, performed along the approximate paths shown in Figure 4.20.

Figure 4.22(b) shows the TDS line scans performed approximately along the same paths. Here, we have for each spatial position plotted the peak intensity in the time-domain, i.e., the whitelight response. From this we see a significant decrease in peak scattering ratio going down to $d = 3$ nm, only a slight decrease for $d = 5$ nm, and the same scattering ratio for $d = 10$ nm and $d = 15$ nm, whereas the M4PP is clearly able to distinguish all thicknesses.

As we have done for the other materials, we resort to modelling the experiment in COMSOL and use FEM to simulate the near-field response for the platinum thin films. We use the conductivity extracted from the M4PP in the simulation for each thickness and perform single point measurements (one on the metal and one on the substrate) and extract a scattering ratio. The results are summarised in Figure 4.23(b) for the $m = 1, 2, 3$ harmonic orders.

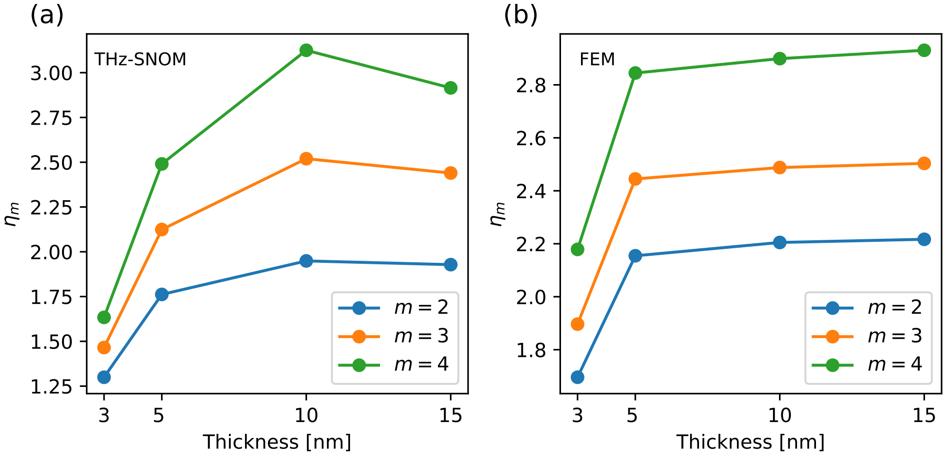

Figure 4.23. (a) Average whitelight scattering ratio extracted as a average of the first 20 µm of the line scans and (b) FEM simulated scattering ratio performed at a frequency of $\nu = 1.25$ THz. The conductivity used for each thickness in the FEM was obtained from the M4PP measurements.

The FEM simulation predicts approximately the same scattering ratio between the three thickest samples and only when lowering the thickness, and by that extension the conductivity, below 5 nm, do we observe a measurable lowering of the scattering ratio. Figure 4.23(a) shows the results from averaging the response from the metal films in Figure 4.23(b), and can thus be compared to the FEM results. We observe remarkable agreement between the experiment and the FEM simulations, however, a one-to-one comparison cannot be made, as the FEM results are performed at a single frequency ($\nu = 1.25$ THz). Regardless, the overall trend between the two can be compared, since we expect a flat spectral response in the conductivity for platinum within our bandwidth based on a Drude response. Thus, we can conclude that we are able to replicate the measurable contrast we observe between the different film thicknesses through FEM simulations.

The results further solidify our ability to distinguish between conductive materials within a given conductivity range, and when the conductivity increases beyond a certain threshold, which for platinum thin-films appears to be approximately 10 mS, contrast is no longer visible.

Part III

Engineered structures and devices: An outlook

Introduction

Until now, we have studying relatively simple structures being MoS_2, exfoliated graphene and large area platinum thin-films, where we have been investigating the material properties and the inherent nature of their near-field response. In this part, we will study more exotic structures and devices, where the purpose is to change or alter the material properties, thus leading new and exciting interactions in the near-field.

The purpose of this part will be to show our ongoing research topics, which at the point of writing is still unfinished, however, has interesting points for discussion and showcasing, and therefore highlights the near future of THz-SNOM and material characterisation. We will study a resonant structure which is engineered to have a resonance at 1 THz, which is around the peak in our bandwidth. Furthermore, we will study a twisted bilayer graphene device, and investigate how the twisting of the graphene layers alter the properties of the material.

CHAPTER 5

Resonant structures: Au antennas

In this chapter, we will look at how antennas with resonance frequencies within our bandwidth appear and behave in the near-field. The near-field response of resonant structures have gained great interest due to their role in sensing, and light-matter interactions, with simple dipole structures to split-ring resonators (SRRs) being studied [38, 135–138] The goal of our study is to determine whether we can map the field enhancement of the antenna, which similar studies have shown to be possible [135, 139]. Being able to map the field enhancement would assist in understanding how to apply resonant structures in metasurface designs for future application and how to optimise such structures. The sample provided in this chapter was fabricated by Dr. Matej Sebek in our group. As mentioned before, the work presented here is, as of time of writing, unfinished, therefore the purpose is to show one of our current projects as discuss initial results to the best of our ability.

5.1 Bowtie structure design

We examine the classical bowtie antenna structure, which in and of itself is a very simple design. The structure is made of electron beam evaporated gold with a 5 nm titanium adhesion layer and has a thickness of 50 nm. The total length of the antenna is 100 µm and a width of 50 µm. CST simulations conducted by Dr. Matej Sebek suggest that the antenna's resonance should be just below 1 THz. This makes it an excellent candidate for our specific bandwidth, since our bandwidth peaks around 1 THz. An AFM image of the sample is shown in Figure 5.1. We notice in the top left corner, that there is a large particle, which we can use as an identification marker later.

We also have antennas of varying sizes and gap lengths, including a bowtie antenna resonant at 0.7 THz. However, this frequency is at the limit of our bandwidth, which may prevent us from capturing the entire frequency enhancement, despite the gold bowtie structure's resonance width being quite narrow. Therefore, we for now limit our study to the specific dimensions of the sample shown in Figure 5.1.

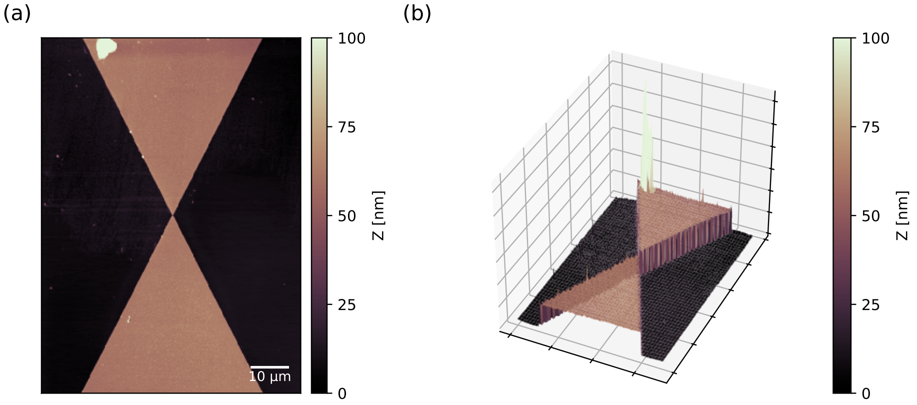

Figure 5.1. AFM profile of bowtie structure (a) seen from above and (b) from an angle. The thickness of the bowtie is 50 nm, and the total length of the structure is 100 µm, with a gap of 100 nm.

5.2 THz-SNOM response

We start, as we have done in the previous chapters, by performing a whitelight and examine the averaged frequency response. Noteworthy is that it is the far-field diffraction limited THz radiation that resonates with the antenna and not the deep sub-diffraction scattered fields. Figure 5.2 shows the whitelight response for the $m = 3$ harmonic of the whole 100 µm length of the antenna with a step size of 140 nm. Since the gap of the bowtie is 100 nm, with this step size we do not resolve the gap. CST simulations suggest that the field enhancement provided by the antenna should be localised in the gap. However, an interesting observation we make from the whitelight image is a structure in the scattered ratio, where the lower part of the antenna yields a stronger scattering ratio than the upper part around the gap. At the far ends of the antenna, we observe the opposite effect, with the upper part yielding a higher scattering ratio than the lower part. At first glance, one might speculate whether this resembles a standing wave pattern or if the corners facing upwards accumulate a higher scattering ratio. The latter would indicate that the orientation of the antenna may affect the distribution within the antenna.

The current orientation of the antenna corresponds to being parallel with the polarisation of the incoming THz pulse, therefore we rotate the sample with respect to the polarisation of the THz pulse and examine the response. Since the whitelight is an averaged frequency response, we do not expect any major changes in the distribution when rotating the sample by 90 degrees, thereby making it perpendicular with the polarisation of the THz. This will, however, give insights into the origins of the asymmetry in the whitelight scan. Figure 5.3 shows the whitelight response of the whole antenna at three different sample rotations: 180 degrees, 90 degrees, and 45

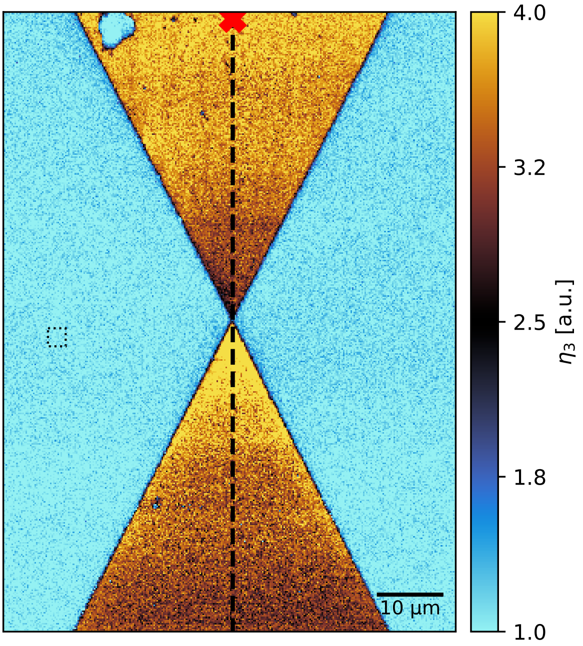

Figure 5.2. Whitelight response of the structure shown in Figure 5.1 for the $m = 3$ harmonic scattering ratio, referenced to the substrate, marked by the black dotted box. The step size in both directions is 140 nm. The black dashed line indicates where a full TDS line scan has been performed, with the red cross indicating the starting position.

degrees.

Firstly, in Figure 5.3(a), we observe that rotating the antenna 180 degrees yields an identical response. This suggests that the observed effect is not inherent to the antenna and material itself, but rather a characteristic of the THz-SNOM measurement technique. Secondly, when examining the response with the antenna perpendicular to the THz polarisation, as shown in Figure 5.3(c), we note an almost symmetric response around the gap. However, a larger scattering ratio is again observed in the upper corners compared to the lower corners, albeit not to the same extent as in the parallel orientation. Lastly, for the 45 degree antenna rotation shown in Figure 5.3(b), we observe similar behaviour to the parallel orientation, however in this configuration the lower most part also shows an increase in scattering ratio. All this leads to the preliminary conclusion that the orientation of the antenna with respect to the incident THz pulses and the configuration of the setup must influence the intensity of the scattered signal.

Thomas *et al.* studied in 2022 a narrow bandwidth SSR and the resulting near-field signal when probing with a continuous wave (CW) CO_2 pumped methanol laser at 2.5

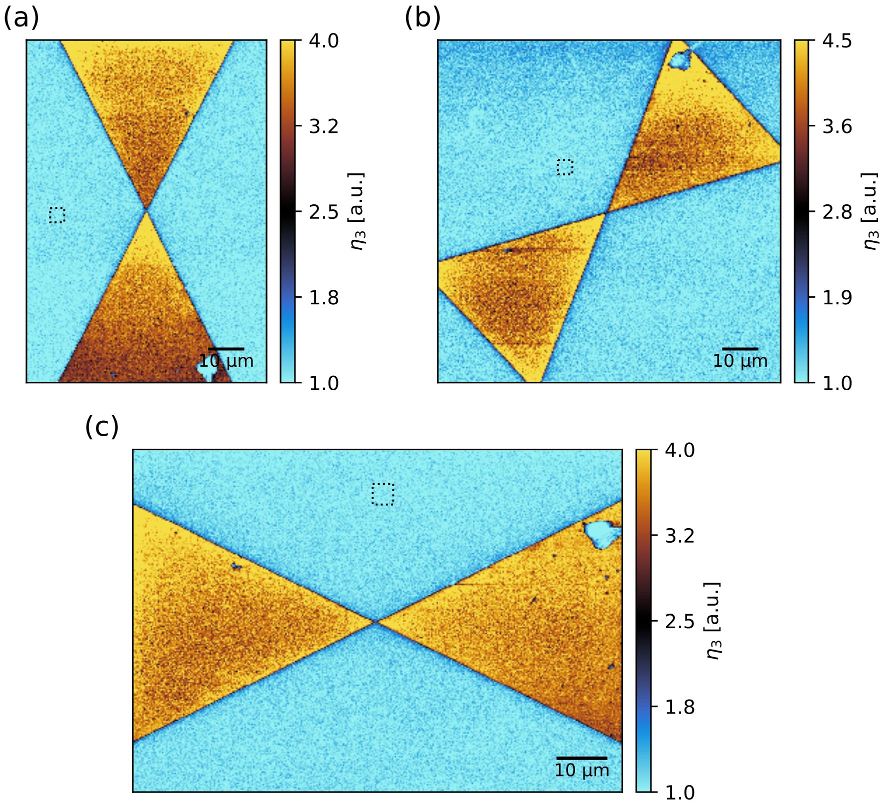

Figure 5.3. Whitelight image for the $m = 3$ harmonic scattering ratio for a sample rotation of (a) 180°, (b) 45°, and (c) 90°. Each image is referenced to the black dotted square shown on the substrate. Step sizes for all image are 140 nm.

THz [138]. In their study, Thomas *et al.* observe similar behaviour for their resonant structure, yielding an asymmetry in the scattered signal. They attribute it to the collection mechanism through the parabolic mirror in the far-field, where depending on which local maxima the tip is in contact with, the light is scattered mainly in a different direction. However, in our case, we observe not only an asymmetry near the field concentration point in the structure, which is in the gap between the upper and lower part but also the opposite asymmetry in the far ends of the structure.

5.3 Spectrally resolved response

A key difference between the two experiments is that we use a broadband pulsed source compared to a single frequency CW source, which could account for the slight differences in observations. To investigate this asymmetry further, we start by performing a full TDS line scan across the whole structure as shown in Figure 5.2. The results of this are shown in Figure 5.4. Here we notice slight fluctuations in the position of the pulse in the time-domain. In the spectral amplitude ratio in Figure 5.4(b), which has been referenced to the first trace (uppermost part of the antenna), we see significant variation when moving onto the lower part as well as variation within each part of the bowtie itself. This fact is especially visible in the phase difference shown in Figure 5.4(c). Thus, it appears that within the bowtie structure itself, significant variations occur at all positions, not only around the gap, where the field gets concentrated. Since we observe slight fluctuations in the position of the peak amplitude in the time-domain, the whitelight scan may be compromised slightly. During a typical whitelight scan, we measure a full time trace at the start and keep that position in time for the whole scan. This means that if a slight drift in the pulse occurs due to, e.g., environmental fluctuations or material phase changes etc., that could result in a drop in amplitude and a misinterpretation can happen.

To further investigate this, we have the possibility to fully map the whole structure with a surface TDS scan, and thus we would be able to examine the spectral response at all position on the bowtie antenna. Furthermore, since we have the full waveform at each pixel, we can plot a true whitelight image. Figure 5.5(a) shows such a manually extracted whitelight image from a 90×150 pixel (~ 600 nm step size) surface TDS scan. From this figure, we do observe many similarities with the whitelight image shown in Figure 5.2, where the lower part of the structure yields an increased signal. However, contrary to Figure 5.2, we now observe that the lowermost corners also yield an increased scattering ratio.

Figure 5.5(b) and (c) show the full waveform and spectra at three different locations on the sample. From the spectrum, e observe a clear enhancement around 1 THz frequency for both the upper and lower parts around the gap, compared to the substrate, as expected.

Apart from creating a whitelight image from the surface scan, we can create a 2D map showing the response at each discrete frequency. This is shown in Figure 5.6.

From this figure, we observe around the resonance frequency similar distributions to the whitelight images, which is to be expected, since the whitelight image is an averaged frequency response, where all frequencies are in phase and therefore participate equally. Thus, due to the enhancement at and around the resonance frequency, these frequencies would dominate in a weighted average. However, in Figure 5.6(b) at 0.7 THz, we observe a distribution we have not observed so far, where the right lowermost part of the bowtie antenna yields the largest scattering ratio. Similar distribution is observed for $\nu = 0.63$ THz. Moreover, for the higher frequencies, we observe horizontal bands, which may be attributed to artefacts in the scan, which are

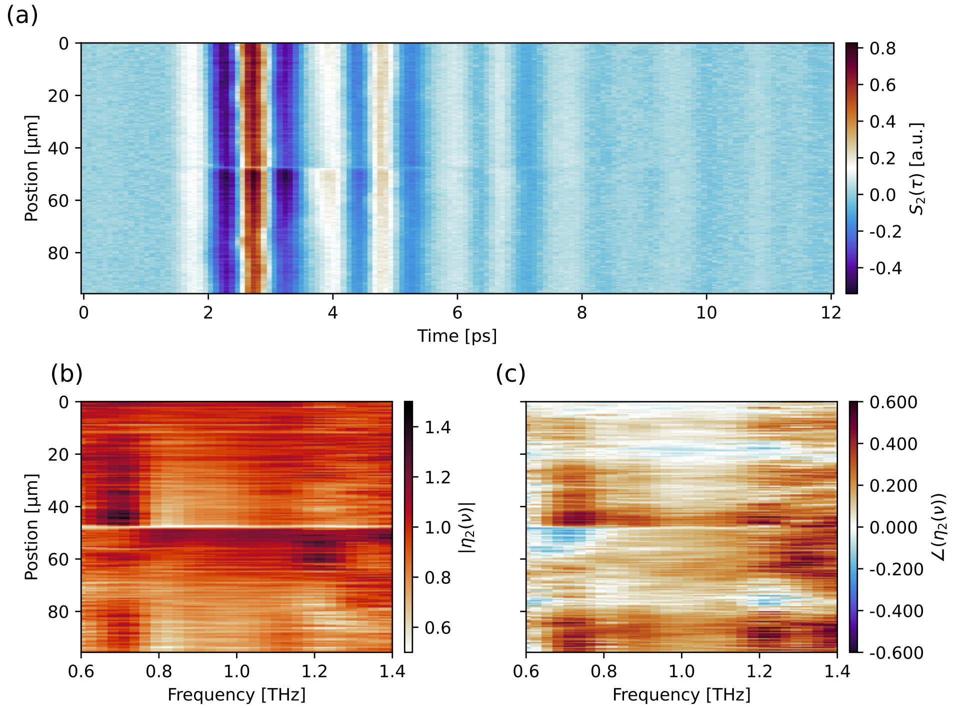

Figure 5.4. (a) Time traces along the path shown in Figure 5.2. (c) Scattering spectral amplitude ratio and (c) corresponding phase difference, where the reference is an average of the first three time traces.

more pronounced at lower intensities of the signal. Most noteworthy from comparing the distribution at each frequency is that we observe changes in the distributions. Currently, one can only speculate as to the reason behind this, therefore further experiments are necessary in order to fully understand the nature of resonant structures in the near-field.

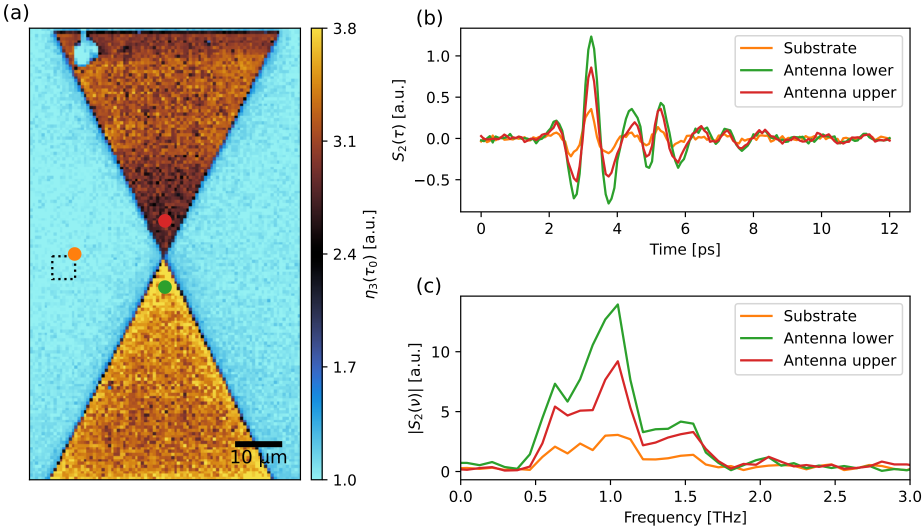

Figure 5.5. (a) True whitelight image generated from a full surface TDS scan with a step size of ~ 600 nm in both directions, with the black dotted box being a 5×5 pixel average of the substrate. (b) Time-domain traces at three different position indicated in (a), and (c) their corresponding spectra.

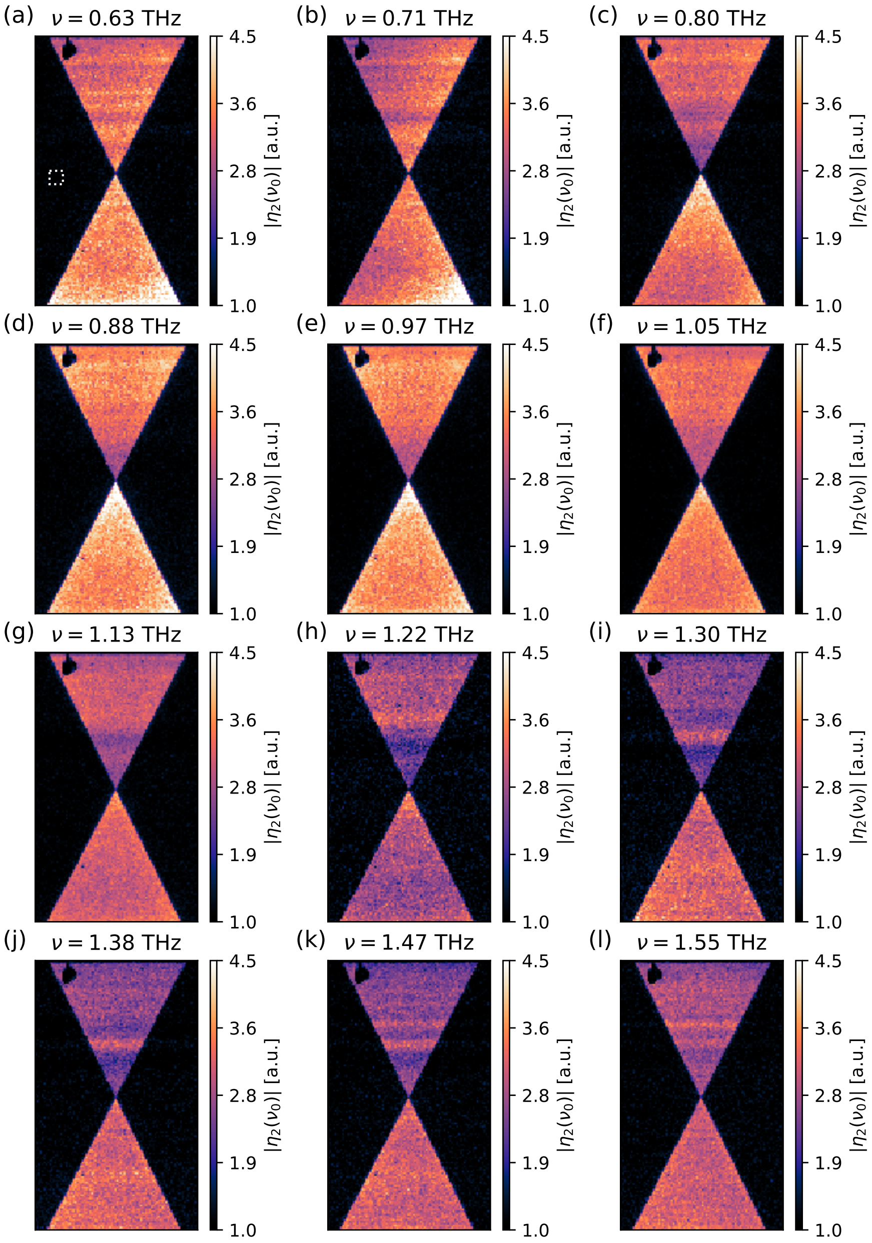

Figure 5.6. Spectral amplitude of the $m = 2$ harmonic at a single frequency ν_0 within our bandwidth. The white dotted box in (a) indicate the area chosen for reference at each frequency.

CHAPTER 6

Magic-angle twisted bi-layer graphene

Twisted bilayer graphene (tBLG) has emerged as a fascinating subject of study in the realm of condensed matter physics and material science due to its unique electronic properties and structural versatility [140–142]. For tBLG, two layers of graphene sheets are stacked together with a relative twist angle between them. This twisting results in a moiré superlattice pattern, giving rise to new electronic band structures and correlated electronic states that are highly sensitive to the twist angle [141, 143–145].

One intriguing aspect of tBLG is the ”magic angle” phenomenon. This is when the twist angle between the two graphene layers is close to a specific value, approximately 1.1 degrees. Magic angle twisted bilayer graphene (mtBLG) exhibits exceptionally flat electronic bands, leading to enhanced electron interactions and correlation effects, which brings about a variety of exotic physical phenomena, such as superconductivity [146, 147], ferromagnetism [148, 149], and correlated insulator states [150, 151], opening new frontiers for fundamental research.

For these reasons, mtBLG is currently a fascinating material and has gathered great interest. This chapter is dedicated to showing our first results with mtBLG and its near-field response in the THz range.

6.1 Sample structure

The sample, shown in Figure 6.1, was fabricated by our collaborators at DTU Physics, specifically by Dr. Tuan Khanh Chau in the group of Prof. Peter Bøggild. Optical microscope images of the sample were also obtained by Dr. Tuan Khanh Chau.

In Figure 6.1, the approximate positions of the graphene and the twisted graphene areas are highlighted by the yellow and red dashed regions, respectively. The twist angle of the graphene is aimed to be 1.1 degrees, which would result in magic angle twisted bilayer graphene. In addition to the twisted graphene layer, the structure is placed on top of an α-ruthenium trichloride ($\alpha - \mathrm{RuCl}_3$) piece, which acts as a dopant source for the graphene, inducing a strongly p-doped state to the graphene and lead to many interesting phenomena [152–159]. The whole structure is then fully encapsulated between two hexagonal-boron nitride (hBN) flakes, which shields the graphene from ambient contaminants.

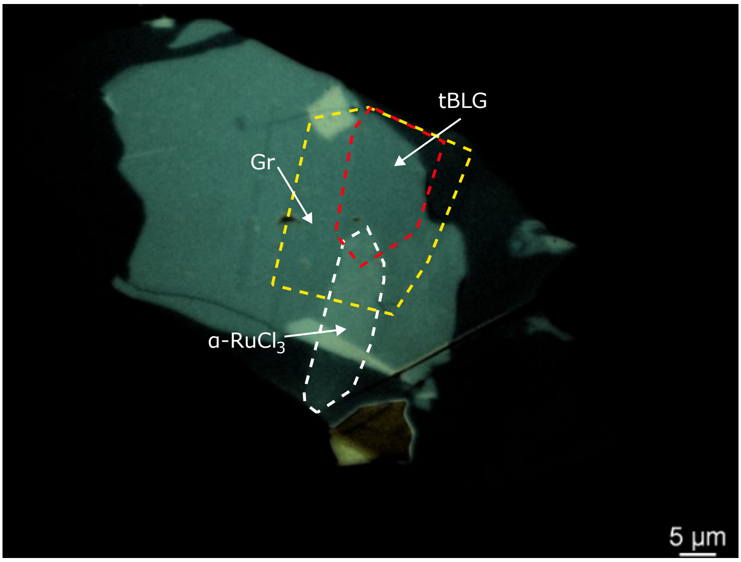

Figure 6.1. Optical microscope image of twisted bilayer graphene sample. Approximate positions of material regions are highlighted. The graphene is fully encapsulated in hBN.

6.2 THz-SNOM response

In the same fashion as earlier experiments, we perform initial whitelight scans of the structure, which are shown in Figure 6.2 along side AFM obtained concurrently. We perform an initial overview scan which captures most of the structure, while also being aware of the large protruding piece observed near the bottom of the device as seen in Figure 6.1. Figure 6.2(a) and (c) show a 30×30 μm^2 area with a 200×200 pixel density, yielding a step size of 150 nm.

From the whitelight images, we are clearly able to identify the boundaries of the graphene as well as the $\alpha - \mathrm{RuCl}_3$ piece. Furthermore, we observe two regions with a decreased signal. The region in the top left corner we attribute to an additional piece of hBN, which shows a similar response as the substrate, but the added height effectively lowers the signal obtained from the graphene. However, the large area around the centre of the graphene flake with decreased signal corresponds to the area where the twisted bilayer should be. Threfore, we performed a higher resolution scan of that area, marked by the white dotted box, shown in Figure 6.2(b) and (d).

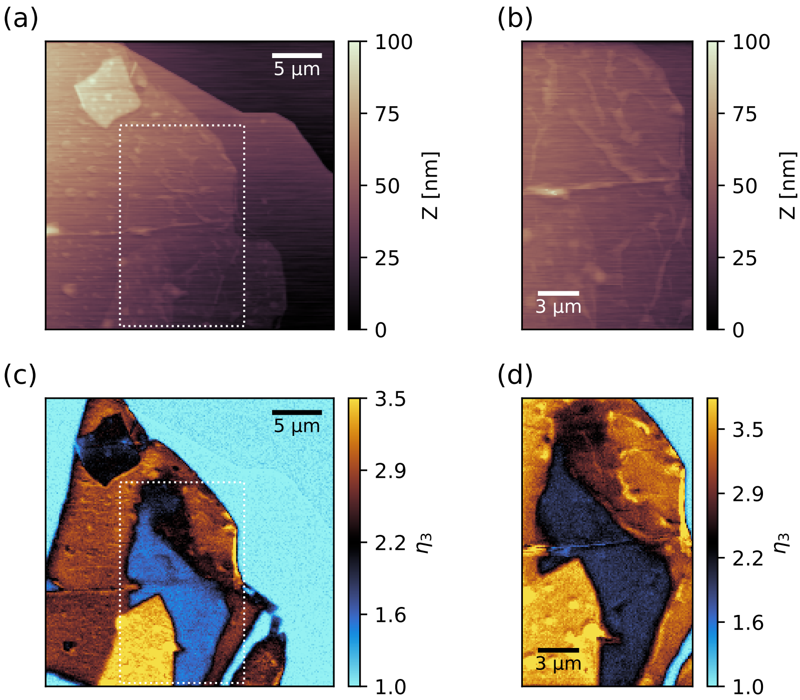

Figure 6.2. (a) AFM and (c) corresponding whitelight images of the device. (b) AFM and (d) corresponding whitelight images of a close-up high resolution scan of the region marked by the white dotted box in (a) and (c). Both whitelight images show the scattering ratio referenced to the hBN on substrate for the $m = 3$ harmonic.

Comparing the two scans, they overall show similar tendencies with the $\alpha - \mathrm{RuCl}_3$ region yielding the highest scattering ratio and a large area of decreased scattering ratio. Based on this, we can isolate all the regions in the whitelight image, which is shown in Figure 6.3. Interestingly, we observe a region between the graphene and the assumed mtBLG, which shows a decreased scattering ratio compared to graphene, but yields a larger scattering ratio than mtBLG. This area is marked by the green dashed line. It may be that this specific region has a slightly different twist angle compared to the other area, which could cause a change in the material properties and is therefore reflected in the scattering ratio. We have previously seen an area on bilayer graphene which showed a lowering in scattered signal (see Figure 4.6(h)). This was, however, from the same crystal and therefore should not be able to have a twist. To fully uncover the green region, further investigation is needed.

Most importantly is that the region where the supposed mtBLG resides shows a lowering in the scattering ratio, compared to the previous chapter, where we observed an increase in scattered signal with increasing amount of layers. Thus, from these

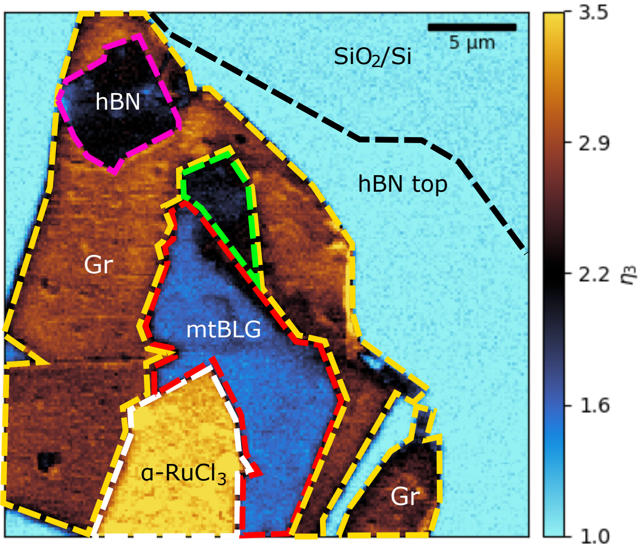

Figure 6.3. Identification of regions in the whitelight scan of the device. The green region is undefined. The yellow regions are monolayer graphene, the red region is the supposed magic-angle twisted bilayer graphene, the white region is the $\alpha - RuCl_3$ and the purple region is an hBN flake on top of the monolayer graphene.

first measurements we can conclude that the twisting of two graphene layers at the magic angle appears to lower the scattering ratio and therefore would correspond to a lowering of conductivity, within our bandwidth.

Another interesting observation from comparing Figure 6.2(a) and (c) to the close-up area in Figure 6.2(b) and (d) is the wrinkles or bubbles in the hBN layer. The large fold in hBN going across the sample is visible in both scans. However, the smaller wrinkles appear to have slightly changed positions. This is especially visible from the AFM images. This could indicate that the tip being in close proximity with the surface is able to effectively move these wrinkles or bubbles without doing damage to the surface. We also observe that the wrinkles or bubbles appear in the whitelight image to increase the scattered signal, which may be attributed to edge effects.

6.3 Gate sweep

To further study the dynamics of this sample consisting of monolayer graphene, mtBLG, and the p-dopant $\alpha - RuCl_3$, Au electrodes were fabricated onto the sample for electrical control of the doping. By doing so, we are able to perform gate sweeping and study the effects on the conductivity. Based on the previous chapter, we expect to see a gate voltage at which the monolayer region and the monolayer on $\alpha - \mathrm{RuCl}_3$ region appear equal.

Figure 6.4 shows an optical microscope image of the device where a cut through the sample has been made in order to attach the side contacts to the graphene. The electrodes are made out of gold and are 50 nm in thickness. Again, the approximate positions of the regions of interest have been marked.

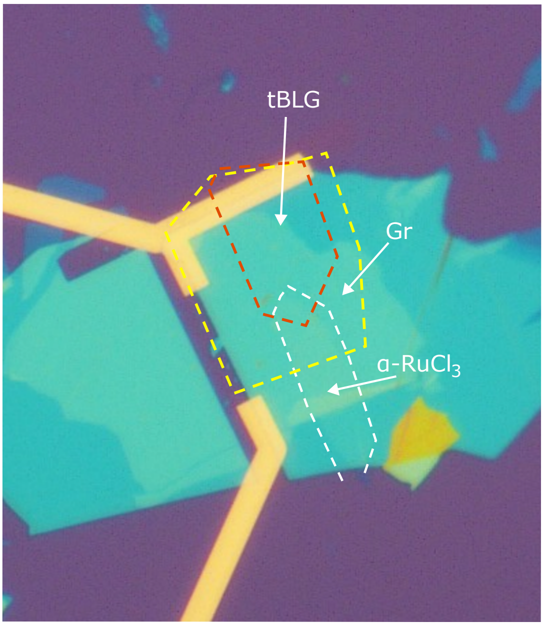

Figure 6.4. Optical microscope image of the device with gold electrodes fabricated onto the device for gating. Approximate positions of the materials are highlighted.

Figure 6.5(a) and (b) show the AFM and the whitelight imaged at 0 V of the region of interest, respectively. Figure 6.5(b) should therefore be almost identical to Figure 6.2(c) and (d), though some slight changes could happen since the device, instead of having a floating potential, is now grounded. We do observe many similarities between the floating and grounded images, such as the monolayer region yielding a lower scattering ratio than the monolayer on $\alpha - \mathrm{RuCl}_3$. Again, we observe the twisted bilayer region to yield a lowering in the scattered signal. Thus, we commence the gate sweep.

The procedure for performing the gate sweep measurements was to start at 0 V and go towards negative voltages, before returning to zero and compare to the starting point, confirming that no distinct damages or changes had occurred. After that we swept the positive voltages. We have an additional positive voltage point ($V_g = 75$ V) compared to the negative voltages, since we decided to get to monitor differences happening around these gate voltages. Due to the quality of the sample, we were able

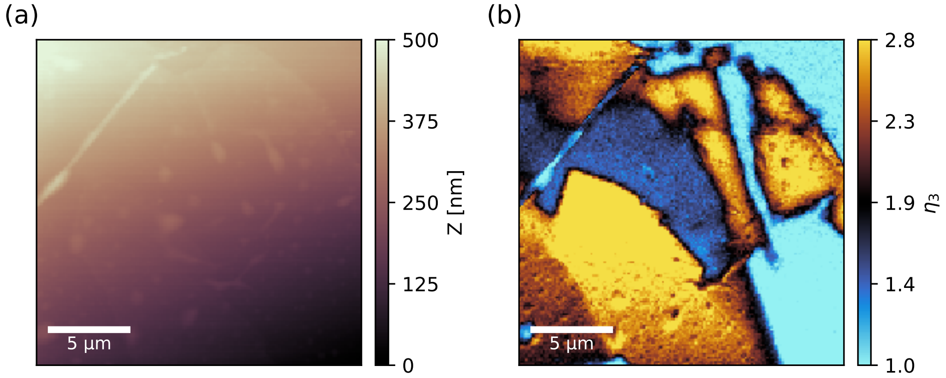

Figure 6.5. (a) AFM image and (b) whitelight image showing the $m = 3$ scattering ratio of the device at $V_g = 0$ V.

to sweep the voltage all the way down to -100 V and all the way up to 100 V, before the leakage current started to approach dangerous values of a few nA.

A summary of the whitelight images taken at 8 different voltages is shown in Figure 6.6. All whitelight maps are referenced to the substrate (which in this case is hBN/SiO_2/Si) at $V_g = 0$ V and plotted on the same colour for ease of comparison.

From Figure 6.6, it is evident that changing the gate voltage has a significant impact on the scattered signal measured. For $V_g = -100$ V, we are clearly able to make out the border of the $\alpha - RuCl_3$ compared to the surrounding monolayer graphene and the twisted bilayer regions. On the other hand, at $V_g = 50$ V and above, we are no longer able to distinguish between the graphene on $\alpha - RuCl_3$, and the pure monolayer graphene. This is exactly what we expect to see, since we increase the conductivity of graphene so much that the near-field reflection coefficient essentially becomes unity, a topic we discussed in detail in chapter 4. Concurrently, we observe that we are able to increase and decrease the scattered signal from the twisted bilayer region as well. We observe that going from $V_g = 50$ V to $V_g = 75$ V the monolayer graphene and $\alpha - RuCl_3$ region appear relatively unchanged, suggesting that though we increase the conductivity, the near-field reflection coefficient is already near unity. However, we are still able to increase the scattered signal from the twisted bilayer region, until reaching $V_g = 100$ V where we observe an overall decrease in signal, which may be related to approaching the threshold of the device. Interestingly, the twisted bilayer region shows a lower scattering ratio across all gate voltages. The overall trend of how the THz response of graphene behaves during gate sweeping is similar to previous far-field studies, where in one extreme the graphene shows a low conductivity, and in the other extreme shows a large conductivity [117, 160].

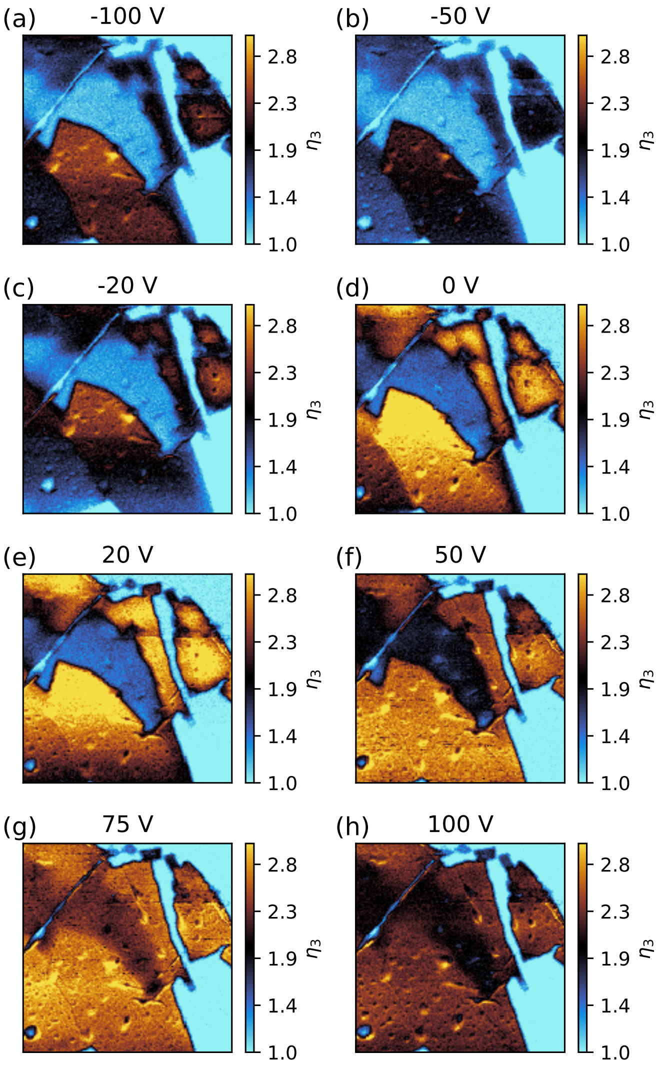

Figure 6.6. Whitelight images showing the scattering ratio for the $m = 3$ harmonic at gate voltages ranging from -100 V to 100 V for the device. Each whitelight image is 150 × 150 pixels resulting in a step size of 133 nm. All maps are referenced to the substrate at $V_g = 0$ V.

From Figure 6.6, we can extract point gate sweeps and compare the evolution between the different regions. Thus, we extract 4 × 4 pixel areas from monolayer graphene, monolayer graphene on $\alpha - \mathrm{RuCl}_3$, and the twisted bilayer region. This can be seen in Figure 6.7, where the extraction location is shown by the starts in the inset.

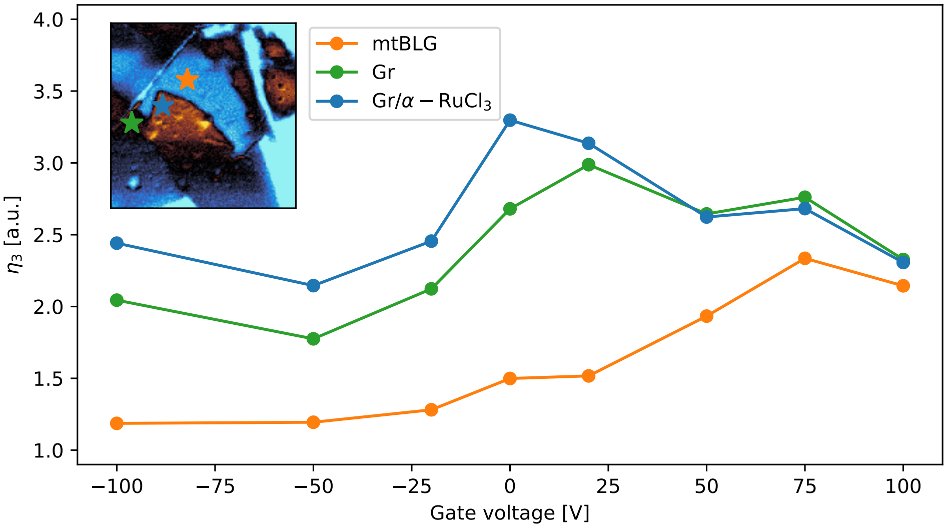

Figure 6.7. Scattering ratio as a function of the gate voltage at three different position on the device, marked in the inset, resembling an IV curve. The plotted points are an average of a 4 × 4 pixel area at the position marked.

It is important to mention, that this is not necessarily an I-V curve, so one cannot make a one-to-one correlation. However, if one were to speculate, it would appear as if the charge neutrality point (CNG) sits at around $V_\mathrm{g} = -50$ V. We also see that the twisted bilayer rises significantly slower with a maximum at a higher gate voltage compared to the monolayer graphene. However, we do also see a decrease in scattered signal as noted earlier for graphene and $\alpha - \mathrm{RuCl}_3$. To better understand this phenomenon, additional experiments are needed to confirm the trends we observe.

Conclusion

In summary, this thesis has outlined the current state of performing terahertz time-domain spectroscopy (THz-TDS) at the nanoscale by combining the technique with scattering-type scanning near-field optical microscopy (s-SNOM), and has shown the current limitations the combined technique (THz-SNOM) faces.

The thesis was divided into three distinct parts, each with their own unique properties. In part I, we studied the THz near-field response of the semiconductor molybdenum disulfide (MoS_2) with the aim of extracting the optical properties in the form of the dielectric permittivity in the THz range. The specific sample studied was a PLD-grown MoS_2 nanoribbon, measuring 0.8×7 μm^2 in size and up to 15 nm in height. From the whitelight image, corresponding to the delay stage in the THz generation and detection system being parked at the peak intensity in the time domain, we observed a lower amount of scattered signal from the nanoribbon compared to the Al_2O_3 (sapphire) substrate. This was immediately explained by MoS_2 having a lower permittivity than sapphire. Additionally, we observed contrast within the nanoribbon itself, suggesting local variations in the properties of the nanoribbon, on a scale much smaller than the probing wavelength.

We used the finite dipole model (FDM) with a layered extension through the transfer matrix model to describe the near-field interactions with the goal of extracting a value for the permittivity. A minimisation routine was employed, since it is currently not possible to directly invert the model, to extract a frequency-averaged permittivity map directly from the whitelight image. This permittivity map contained only information on the real part of the complex permittivity, as no phase information is contained in the whitelight image.

Next, we performed full spectroscopic analysis of the nanoribbon by conducting a TDS line scan across its width. By using the same minimisation routine as for the whitelight image, we were able to obtain not only the real part of the permittivity but also the imaginary part for our given frequency range, ranging from 0.5 THz to 1.6 THz. The extracted, frequency-resolved permittivity at the nanoscale was compared to previous far-field studies and models, which showed similar values, though some differences were present. Nonetheless, this study demonstrates the promising aspects of the technique, being capable of extracting optical properties at the nanoscale in the THz region.

Part II then shifted the focus to conductive samples, with particular emphasis on graphene. Our goal, similar to that with MoS_2, was to extract the optical and electrical properties of graphene in the low-frequency THz region. However, previous reports suggested this to be a challenging task, as graphene was observed to be a near-perfect reflector regardless of quality in the THz region. In contrast, we found that we were indeed able to distinguish not only graphene of different layer amounts but also to observe contrast within a single layer, reigniting the possibility of quantitative analysis of graphene in the near-field. The observable contrast, however, could not be explained with the current state-of-the-art theory pertaining to tip-sample near-field interactions, namely the FDM with an infinitely thin conductive layer accounted for through the layered extension.

Finite element method (FEM) simulations were performed to investigate whether the contrast was observable in full wave simulations. Surprisingly, we were able to reproduce the scattering contrast observed experimentally without the need to account for non-local behaviour, suggesting that the contrast can be explained through classical electromagnetic interactions.

The ability to observe contrast between varying conductivity was not limited to graphene but was also visible in platinum thin films. Here, we studied four different thicknesses of platinum thin films: $d = 3$ nm, $d = 5$ nm, $d = 10$ nm, and $d = 15$ nm. Moving from 3 nm to 5 nm in thickness, we observed an increase in scattered signal, corresponding to an increase in conductivity. However, further increasing the thickness showed that a clear contrast was no longer observable, indicating that beyond a certain conductivity threshold, the near-field reflection coefficient approaches unity, and contrast is therefore no longer discernible. These results were in great agreement with FEM simulations.

Lastly, the purpose of part III was to investigate more complex sample compositions, such as graphene devices and resonant structures. In chapter 5, we demonstrated that through THz-SNOM, we can utilise the broadband THz source to spatially map the response of a bowtie antenna at different frequencies, unveiling the resonance behaviour of the antenna. To fully explore spectroscopic aspects, however, improvements in tip design are needed, as the spectrum is currently heavily dominated by resonances stemming from the cantilever. Previous reports also suggest that the tip interferes with the signal enhanced at resonance, where we observed similar trends in the scattered signal from the structure.

In chapter 6, we investigated what happens when two graphene layers are placed at an angle, leading to twisted bilayer graphene. When this angle is approximately 1.1 degrees, the properties of bilayer graphene change drastically. We observed a lower scattered response from twisted bilayer graphene compared to the monolayer response, which starkly contrasts the trends established in chapter 4, suggesting that the optical and electrical properties indeed change drastically. Furthermore, we performed gate sweeps on the device, with gate voltages ranging from -100 V to 100 V. We found that we were able to increase the conductivity of the monolayer graphene region to a point where it was indiscernible from the region heavily doped by a $\alpha - RuCl_3$ piece, confirming our ability to observe contrast in conductivity below a certain threshold.

Future and outlook: Next steps

The next steps will be to continue on the results presented in part III of this thesis, thus investigate the impact of magic-angle twisted bilayer graphene. Figure 6.8 shows such a new device.

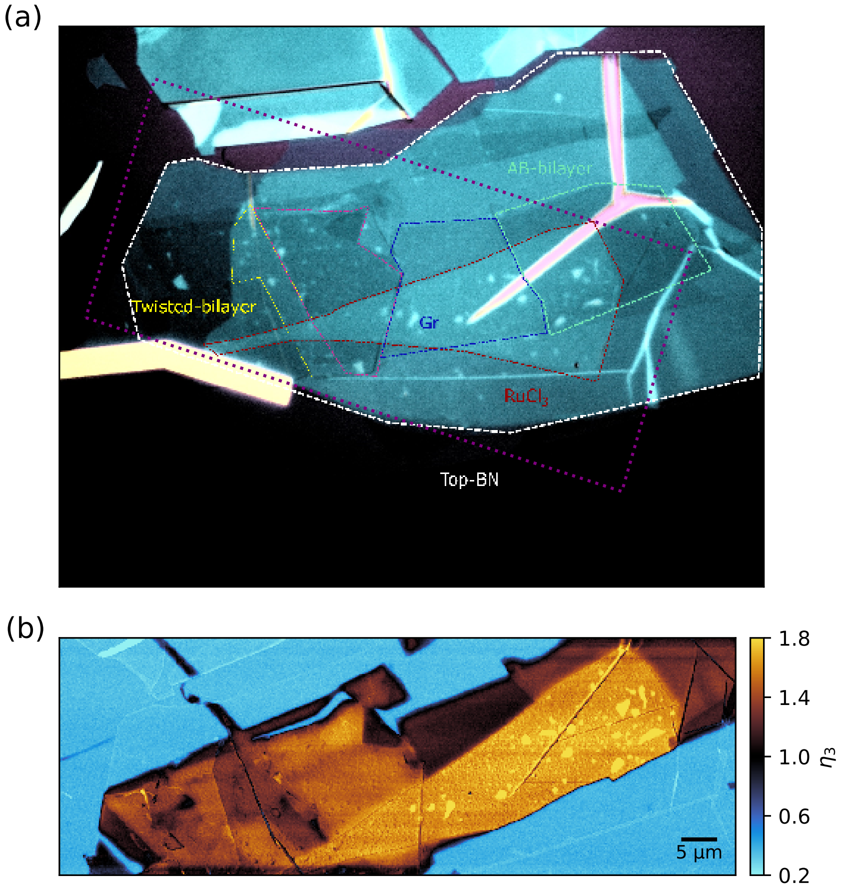

Figure 6.8. (a) Optical microscope image of twisted bilayer graphene device with twisted bilayer, monolayer graphene, AB bilayer graphene and $\alpha - \mathrm{RuCl_3}$ regions. (b) Whitelight image of the outer purple dotted rectangle shown in (a).

In this device, we combine and summarise a few of the key points presented in this thesis regarding conductive materials:

1. Bilayer graphene yields a larger scattering ratio than monolayer, even under full encapsulation.
2. $\alpha - \mathrm{RuCl}_3$ heavily dopes graphene and we are able to observe this increase compared to undoped regions.
3. Contrast within a single layer or region is able to be resolved.

The subsequent phase of the research will involve conducting gate voltage sweeps on this sample, allowing for a comprehensive investigation of a multitude of phenomena in a single experimental sequence.

In conclusion, this thesis underscores the future prospects and potential applications of THz-SNOM in non-invasively probing the material properties of nanoscale devices, thereby enabling an assessment of their quality. It also solidifies the importance of advancing our theoretical understanding of the complex interactions between the tip and the sample.

Appendices

List of Figures

List of Tables

Bibliography

[1] G. Binnig, C. F. Quate, and C. Gerber, “Atomic force microscope,” *Physical Review Letters*, vol. 56, pp. 930–933, 3 1986.

[2] F. Ohnesorge and G. Binnig, “True atomic resolution by atomic force microscopy through repulsive and attractive forces,” *Science*, vol. 260, pp. 1451–1456, 6 1993.

[3] N. Jalili and K. Laxminarayana, “A review of atomic force microscopy imaging systems: application to molecular metrology and biological sciences,” *Mechatronics*, vol. 14, pp. 907–945, 10 2004.

[4] F. J. Giessibl, “Advances in atomic force microscopy,” *Reviews of Modern Physics*, vol. 75, pp. 949–983, 7 2003.

[5] H.-J. Butt, B. Cappella, and M. Kappl, “Force measurements with the atomic force microscope: Technique, interpretation and applications,” *Surface Science Reports*, vol. 59, pp. 1–152, 10 2005.

[6] M. Khan, Q. Wang, and M. Fitzpatrick, “Atomic force microscopy (afm) for materials characterization,” 2016.

[7] O. D. Payton, L. Picco, and T. B. Scott, “High-speed atomic force microscopy for materials science,” *International Materials Reviews*, vol. 61, pp. 473–494, 11 2016.

[8] M. Marrese, V. Guarino, and L. Ambrosio, “Atomic force microscopy: A powerful tool to address scaffold design in tissue engineering,” *Journal of Functional Biomaterials*, vol. 8, p. 7, 2 2017.

[9] C. Möller, M. Allen, V. Elings, A. Engel, and D. J. Müller, “Tapping-mode atomic force microscopy produces faithful high-resolution images of protein surfaces,” *Biophysical Journal*, vol. 77, pp. 1150–1158, 8 1999.

[10] P. Eaton and P. West, *Atomic Force Microscopy.* Oxford University Press, 3 2010.

[11] E. Synge, "A suggested method for extending microscopic resolution into the ultra-microscopic region," *The London, Edinburgh, and Dublin Philosophical Magazine and Journal of Science*, vol. 6, pp. 356–362, 8 1928.

[12] E. A. Ash and G. Nicholls, "Super-resolution aperture scanning microscope," *Nature*, vol. 237, pp. 510–512, 6 1972.

[13] D. W. Pohl, W. Denk, and M. Lanz, "Optical stethoscopy: Image recording with resolution $\lambda/20$," *Applied Physics Letters*, vol. 44, pp. 651–653, 4 1984.

[14] E. Betzig, M. Isaacson, and A. Lewis, "Collection mode near-field scanning optical microscopy," *Applied Physics Letters*, vol. 51, pp. 2088–2090, 12 1987.

[15] B. Hecht, B. Sick, U. P. Wild, V. Deckert, R. Zenobi, O. J. F. Martin, and D. W. Pohl, "Scanning near-field optical microscopy with aperture probes: Fundamentals and applications," *The Journal of Chemical Physics*, vol. 112, pp. 7761–7774, 5 2000.

[16] F. Zenhausern, Y. Martin, and H. K. Wickramasinghe, "Scanning interferometric apertureless microscopy: Optical imaging at 10 angstrom resolution," *Science*, vol. 269, pp. 1083–1085, 8 1995.

[17] B. Knoll and F. Keilmann, "Near-field probing of vibrational absorption for chemical microscopy," *Nature*, vol. 399, pp. 134–137, 5 1999.

[18] B. Knoll and F. Keilmann, "Enhanced dielectric contrast in scattering-type scanning near-field optical microscopy," *Optics Communications*, vol. 182, pp. 321–328, 2000.

[19] F. Keilmann and R. Hillenbrand, "Near-field microscopy by elastic light scattering from a tip," *Philosophical Transactions of the Royal Society A: Mathematical, Physical and Engineering Sciences*, vol. 362, pp. 787–805, 4 2004.

[20] S. Amarie, T. Ganz, and F. Keilmann, "Mid-infrared near-field spectroscopy," *Optics Express*, vol. 17, p. 21794, 11 2009.

[21] H. A. Bechtel, E. A. Muller, R. L. Olmon, M. C. Martin, and M. B. Raschke, "Ultrabroadband infrared nanospectroscopic imaging," *Proceedings of the National Academy of Sciences*, vol. 111, pp. 7191–7196, 5 2014.

[22] I. Amenabar, S. Poly, W. Nuansing, E. H. Hubrich, A. A. Govyadinov, F. Huth, R. Krutokhvostov, L. Zhang, M. Knez, J. Heberle, A. M. Bittner, and R. Hillenbrand, "Structural analysis and mapping of individual protein complexes by infrared nanospectroscopy," *Nature Communications*, vol. 4, p. 2890, 12 2013.

[23] F. Mooshammer, F. Sandner, M. A. Huber, M. Zizlsperger, H. Weigand, M. Plankl, C. Weyrich, M. Lanius, J. Kampmeier, G. Mussler, D. Grützmacher, J. L. Boland, T. L. Cocker, and R. Huber, "Nanoscale near-field tomography

of surface states on $(Bi_{0.5}Sb_{0.5})_2Te_3$," *Nano Letters*, vol. 18, pp. 7515–7523, 12 2018.

[24] J. A. Gerber, S. Berweger, B. T. O'Callahan, and M. B. Raschke, "Phase-resolved surface plasmon interferometry of graphene," *Physical Review Letters*, vol. 113, p. 055502, 7 2014.

[25] K. J. Kaltenecker, S. R. D. S., M. Rasmussen, H. B. Lassen, E. J. R. Kelleher, E. Krauss, B. Hecht, N. A. Mortensen, L. Grüner-Nielsen, C. Markos, O. Bang, N. Stenger, and P. U. Jepsen, "Near-infrared nanospectroscopy using a low-noise supercontinuum source," *APL Photonics*, vol. 6, 6 2021.

[26] K. J. Kaltenecker, E. Krauss, L. Casses, M. Geisler, B. Hecht, N. A. Mortensen, P. U. Jepsen, and N. Stenger, "Mono-crystalline gold platelets: a high-quality platform for surface plasmon polaritons," *Nanophotonics*, vol. 9, pp. 509–522, 2 2020.

[27] L. N. Casses, K. J. Kaltenecker, S. Xiao, M. Wubs, and N. Stenger, "Quantitative near-field characterization of surface plasmon polaritons on monocrystalline gold platelets," *Optics Express*, vol. 30, p. 11181, 3 2022.

[28] E. Yoxall, M. Schnell, A. Y. Nikitin, O. Txoperena, A. Woessner, M. B. Lundeberg, F. Casanova, L. E. Hueso, F. H. L. Koppens, and R. Hillenbrand, "Direct observation of ultraslow hyperbolic polariton propagation with negative phase velocity," *Nature Photonics*, vol. 9, pp. 674–678, 10 2015.

[29] J. Taboada-Gutiérrez, G. Álvarez Pérez, J. Duan, W. Ma, K. Crowley, I. Prieto, A. Bylinkin, M. Autore, H. Volkova, K. Kimura, T. Kimura, M.-H. Berger, S. Li, Q. Bao, X. P. A. Gao, I. Errea, A. Y. Nikitin, R. Hillenbrand, J. Martín-Sánchez, and P. Alonso-González, "Broad spectral tuning of ultra-low-loss polaritons in a van der waals crystal by intercalation," *Nature Materials*, vol. 19, pp. 964–968, 9 2020.

[30] P. Jepsen, D. Cooke, and M. Koch, "Terahertz spectroscopy and imaging - modern techniques and applications," *Laser Photonics Reviews*, vol. 5, pp. 124–166, 1 2011.

[31] M. Tonouchi, S. Kim, I. Kawayama, and H. Murakami, "Laser terahertz emission microscope," p. 80230Q, 5 2011.

[32] H. Jiang, C. Gong, T. Nishimura, H. Murakami, I. Kawayama, H. Nakanishi, and M. Tonouchi, "Terahertz emission spectroscopy and microscopy on ultrawide bandgap semiconductor $\beta - Ga_2O_3$," *Photonics*, vol. 7, p. 73, 9 2020.

[33] H. Nakanishi, A. Ito, K. Takayama, I. Kawayama, H. Murakami, and M. Tonouchi, "Comparison between laser terahertz emission microscope and conventional methods for analysis of polycrystalline silicon solar cell," *AIP Advances*, vol. 5, 11 2015.

[34] M. Yamashita, K. Kawase, C. Otani, T. Kiwa, and M. Tonouchi, "Imaging of large-scale integrated circuits using laser-terahertz emission microscopy," *Optics Express*, vol. 13, p. 115, 2005.

[35] T. Kiwa, M. Tonouchi, M. Yamashita, and K. Kawase, "Laser terahertz-emission microscope for inspecting electrical faults in integrated circuits," *Optics Letters*, vol. 28, p. 2058, 11 2003.

[36] A. Pizzuto, D. M. Mittleman, and P. Klarskov, "Laser thz emission nanoscopy and thz nanoscopy," *Optics Express*, vol. 28, p. 18778, 6 2020.

[37] P. Klarskov, H. Kim, V. L. Colvin, and D. M. Mittleman, "Nanoscale laser terahertz emission microscopy," *ACS Photonics*, vol. 4, pp. 2676–2680, 11 2017.

[38] N. Sulollari, J. Keeley, S. J. Park, P. Rubino, A. D. Burnett, L. Li, M. C. Rosamond, E. H. Linfield, A. G. Davies, J. E. Cunningham, and P. Dean, "Coherent terahertz microscopy of modal field distributions in micro-resonators," *AIP Advances*, vol. 6, 6 2021.

[39] F. Qiu, G. You, Z. Tan, W. Wan, C. Wang, X. Liu, X. Chen, R. Liu, H. Tao, Z. Fu, H. Li, and J. Cao, "A terahertz near-field nanoscopy revealing edge fringes with a fast and highly sensitive quantum-well photodetector," *iScience*, vol. 25, p. 104637, 7 2022.

[40] E. A. A. Pogna, M. Asgari, V. Zannier, L. Sorba, L. Viti, and M. S. Vitiello, "Unveiling the detection dynamics of semiconductor nanowire photodetectors by terahertz near-field nanoscopy," *Light: Science Applications*, vol. 9, p. 189, 11 2020.

[41] M. C. Giordano, S. Mastel, C. Liewald, L. L. Columbo, M. Brambilla, L. Viti, A. Politano, K. Zhang, L. Li, A. G. Davies, E. H. Linfield, R. Hillenbrand, F. Keilmann, G. Scamarcio, and M. S. Vitiello, "Phase-resolved terahertz self-detection near-field microscopy," *Optics Express*, vol. 26, p. 18423, 7 2018.

[42] V. Pistore, E. A. A. Pogna, L. Viti, L. Li, A. G. Davies, E. H. Linfield, and M. S. Vitiello, "Self-induced phase locking of terahertz frequency combs in a phase-sensitive hyperspectral near-field nanoscope," *Advanced Science*, vol. 9, 10 2022.

[43] J. D. Jackson, *Classical electrodynamics.* Wiley, 3rd edition ed., 1999.

[44] J. M. Atkin, S. Berweger, A. C. Jones, and M. B. Raschke, "Nano-optical imaging and spectroscopy of order, phases, and domains in complex solids," *Advances in Physics*, vol. 61, pp. 745–842, 12 2012.

[45] A. Cvitkovic, N. Ocelic, and R. Hillenbrand, "Analytical model for quantitative prediction of material contrasts in scattering-type near-field optical microscopy," *Optics Express*, vol. 15, pp. 8550–8565, 2007.

[46] J. Skaar, “Fresnel’s equations in statics and quasistatics,” *European Journal of Physics*, vol. 40, 6 2019.

[47] N. Ocelić, *Quantitative Near-field Phonon-polariton Spectroscopy.* PhD thesis, 2007.

[48] A. A. Govyadinov, I. Amenabar, F. Huth, P. S. Carney, and R. Hillenbrand, “Quantitative measurement of local infrared absorption and dielectric function with tip-enhanced near-field microscopy,” *Journal of Physical Chemistry Letters*, vol. 4, pp. 1526–1531, 5 2013.

[49] E. T. Ritchie, C. B. Casper, T. A. Lee, and J. M. Atkin, “Quantitative local conductivity imaging of semiconductors using near-field optical microscopy,” *J. Phys. Chem. C*, vol. 126, pp. 4515–4521, 2022.

[50] L. Mester, A. A. Govyadinov, and R. Hillenbrand, “High-fidelity nano-ftir spectroscopy by on-pixel normalization of signal harmonics,” *Nanophotonics*, vol. 11, pp. 377–390, 1 2022.

[51] S. Amarie and F. Keilmann, “Broadband-infrared assessment of phonon resonance in scattering-type near-field microscopy,” *Physical Review B - Condensed Matter and Materials Physics*, vol. 83, 1 2011.

[52] B. Hauer, A. P. Engelhardt, and T. Taubner, “Quasi-analytical model for scattering infrared near-field microscopy on layered systems,” *Optics Express*, vol. 20, pp. 13173–13188, 2012.

[53] T. Zhan, X. Shi, Y. Dai, X. Liu, and J. Zi, “Transfer matrix method for optics in graphene layers,” *J. Phys.: Condens. Matter*, vol. 25, p. 215301, 2013.

[54] K. G. Wirth, H. Linnenbank, T. Steinle, L. Banszerus, E. Icking, C. Stampfer, H. Giessen, and T. Taubner, “Tunable s-snom for nanoscale infrared optical measurement of electronic properties of bilayer graphene,” *ACS Photonics*, vol. 8, pp. 418–423, 2021.

[55] B. E. A. Saleh and M. C. Teich, *Fundamentals of Photonics.* Wiley, 2nd edition ed., 2007.

[56] B. Hauer, *Nano-optical mapping of permittivity contrasts and electronic properties at the surface and beneath.* PhD thesis, 2015.

[57] B. Wang and C. H. Woo, “Atomic force microscopy-induced electric field in ferroelectric thin films,” *Journal of Applied Physics*, vol. 94, pp. 4053–4059, 9 2003.

[58] Z. Fei, G. O. Andreev, W. Bao, L. M. Zhang, A. S. Mcleod, C. Wang, M. K. Stewart, Z. Zhao, G. Dominguez, M. Thiemens, M. M. Fogler, M. J. Tauber, A. H. Castro-Neto, C. N. Lau, F. Keilmann, and D. N. Basov, “Infrared

nanoscopy of dirac plasmons at the graphene-SiO_2 interface," *Nano Lett*, vol. 11, 2011.

[59] A. S. McLeod, P. Kelly, M. D. Goldflam, Z. Gainsforth, A. J. Westphal, G. Dominguez, M. H. Thiemens, M. M. Fogler, and D. N. Basov, "Model for quantitative tip-enhanced spectroscopy and the extraction of nanoscale-resolved optical constants," *Physical Review B - Condensed Matter and Materials Physics*, vol. 90, 8 2014.

[60] G. Wurtz, R. Bachelot, and P. Royer, "Imaging a gaalas laser diode in operation using apertureless scanning near-field optical microscopy," *Eur. Phys. J. AP*, vol. 5, pp. 269–275, 1999.

[61] M. B. Raschke and C. Lienau, "Apertureless near-field optical microscopy: Tip-sample coupling in elastic light scattering," *Applied Physics Letters*, vol. 83, pp. 5089–5091, 12 2003.

[62] A. Pizzuto, X. Chen, H. Hu, Q. Dai, M. Liu, and D. M. Mittleman, "Anomalous contrast in broadband thz near-field imaging of gold microstructures," *Optics Express*, vol. 29, p. 15190, 2021.

[63] G. Conrad, C. B. Casper, E. T. Ritchie, and J. M. Atkin, "Quantitative modeling of near-field interactions incorporating polaritonic and electrostatic effects," *Optics Express*, vol. 30, p. 11619, 3 2022.

[64] F. Mooshammer, M. Plankl, T. Siday, M. Zizlsperger, F. Sandner, R. Vitalone, R. Jing, M. A. Huber, D. N. Basov, and R. Huber, "Quantitative terahertz emission nanoscopy with multiresonant near-field probes," *Optics Letters*, vol. 46, p. 3572, 8 2021.

[65] X. Chen, C. F. B. Lo, W. Zheng, H. Hu, Q. Dai, and M. Liu, "Rigorous numerical modeling of scattering-type scanning near-field optical microscopy and spectroscopy," *Applied Physics Letters*, vol. 111, 11 2017.

[66] X. Chen, Z. Yao, Z. Sun, S. G. Stanciu, D. N. Basov, R. Hillenbrand, and M. Liu, "Rapid simulations of hyperspectral near-field images of three-dimensional heterogeneous surfaces – part II," *Optics Express*, vol. 30, p. 11228, 3 2022.

[67] C. Maissen, S. Chen, E. Nikulina, A. Govyadinov, and R. Hillenbrand, "Probes for ultrasensitive thz nanoscopy," *ACS Photonics*, vol. 6, pp. 1279–1288, 5 2019.

[68] J. Zhu, J.-H. Park, S. A. Vitale, W. Ge, G. S. Jung, J. Wang, M. Mohamed, T. Zhang, M. Ashok, M. Xue, X. Zheng, Z. Wang, J. Hansryd, A. P. Chandrakasan, J. Kong, and T. Palacios, "Low-thermal-budget synthesis of monolayer molybdenum disulfide for silicon back-end-of-line integration on a 200 mm platform," *Nature Nanotechnology*, vol. 18, pp. 456–463, 5 2023.

[69] X. Zhang, L. Huangfu, Z. Gu, S. Xiao, J. Zhou, H. Nan, X. Gu, and K. K. Ostrikov, "Controllable epitaxial growth of large-area MoS_2/WS_2 vertical heterostructures by confined-space chemical vapor deposition," *Small*, vol. 17, 5 2021.

[70] X. Zhang, H. Nan, S. Xiao, X. Wan, X. Gu, A. Du, Z. Ni, and K. Ostrikov, "Transition metal dichalcogenides bilayer single crystals by reverse-flow chemical vapor epitaxy," *Nature Communications*, vol. 10, p. 598, 2 2019.

[71] D. Jariwala, V. K. Sangwan, L. J. Lauhon, T. J. Marks, and M. C. Hersam, "Emerging device applications for semiconducting two-dimensional transition metal dichalcogenides," *ACS Nano*, vol. 8, pp. 1102–1120, 2 2014.

[72] J. Y. Lim, M. Kim, Y. Jeong, K. R. Ko, S. Yu, H. G. Shin, J. Y. Moon, Y. J. Choi, Y. Yi, T. Kim, and S. Im, "Van der waals junction field effect transistors with both n- and p-channel transition metal dichalcogenides," *npj 2D Materials and Applications*, vol. 2, p. 37, 11 2018.

[73] T. Shen, A. V. Penumatcha, and J. Appenzeller, "Strain engineering for transition metal dichalcogenides based field effect transistors," *ACS Nano*, vol. 10, pp. 4712–4718, 4 2016.

[74] S. Zhang, H. Xu, F. Liao, Y. Sun, K. Ba, Z. Sun, Z.-J. Qiu, Z. Xu, H. Zhu, L. Chen, Q. Sun, P. Zhou, W. Bao, and D. W. Zhang, "Wafer-scale transferred multilayer MoS_2 for high performance field effect transistors," *Nanotechnology*, vol. 30, p. 174002, 4 2019.

[75] T. Sun, J. Wang, X. Chi, Y. Lin, Z. Chen, X. Ling, C. Qiu, Y. Xu, L. Song, W. Chen, and C. Su, "Engineering the electronic structure of MoS_2 nanorods by n and mn dopants for ultra-efficient hydrogen production," *ACS Catalysis*, vol. 8, pp. 7585–7592, 2018.

[76] Z. Li, Z. Jiang, W. Zhou, M. Chen, M. Su, X. Luo, T. Yu, and C. Yuan, "MoS_2 nanoribbons with a prolonged photoresponse lifetime for enhanced visible light photoelectrocatalytic hydrogen evolution," *Inorganic Chemistry*, vol. 60, pp. 1991–1997, 2 2021.

[77] F. Sultana, M. Mushtaq, J. Wang, K. Althubeiti, A. Zaman, A. K. Rais, A. Ali, and Q. Yang, "An insight to catalytic synergic effect of Pd-MoS_2 nanorods for highly efficient hydrogen evolution reaction," *Arabian Journal of Chemistry*, vol. 15, p. 103735, 5 2022.

[78] P. Zeng, W. Wang, D. Han, J. Zhang, Z. Yu, J. He, P. Zheng, H. Zheng, L. Zheng, W. Su, D. Huo, Z. Ni, Y. Zhang, and Z. Wu, "MoS_2/WSe_2 vdw heterostructures decorated with pbs quantum dots for the development of high-performance photovoltaic and broadband photodiodes," *ACS Nano*, vol. 16, pp. 9329–9338, 2022.

[79] M. M. Furchi, A. Pospischil, F. Libisch, J. Burgdö, and T. Mueller, “Photovoltaic effect in an electrically tunable van der waals heterojunction terms of use cc-by,” *Nano Lett*, vol. 14, pp. 4785–4791, 2014.

[80] A. Varghese, D. Saha, K. Thakar, V. Jindal, S. Ghosh, N. V. Medhekar, S. Ghosh, and S. Lodha, “Near-direct bandgap WSe_2/ReS_2 type-II pn heterojunction for enhanced ultrafast photodetection and high-performance photovoltaics,” *Nano Letters*, vol. 20, pp. 1707–1717, 2020.

[81] Y. Sun, D. Wang, and Z. Shuai, “Indirect-to-direct band gap crossover in few-layer transition metal dichalcogenides: A theoretical prediction,” *Journal of Physical Chemistry C*, vol. 120, pp. 21866–21870, 9 2016.

[82] S. Li, Y. C. Lin, W. Zhao, J. Wu, Z. Wang, Z. Hu, Y. Shen, D. M. Tang, J. Wang, Q. Zhang, H. Zhu, L. Chu, W. Zhao, C. Liu, Z. Sun, T. Taniguchi, M. Osada, W. Chen, Q. H. Xu, A. T. S. Wee, K. Suenaga, F. Ding, and G. Eda, “Vapour-liquid-solid growth of monolayer MoS_2 nanoribbons,” *Nature Materials*, vol. 17, pp. 535–542, 6 2018.

[83] Y. Li, E. C. Moy, A. A. Murthy, S. Hao, J. D. Cain, E. D. Hanson, J. G. DiStefano, W. H. Chae, Q. Li, C. Wolverton, X. Chen, and V. P. Dravid, “Large-scale fabrication of MoS_2 ribbons and their light-induced electronic/thermal properties: Dichotomies in the structural and defect engineering,” *Advanced Functional Materials*, vol. 28, 3 2018.

[84] T. Chowdhury, J. Kim, E. C. Sadler, C. Li, S. W. Lee, K. Jo, W. Xu, D. H. Gracias, N. V. Drichko, D. Jariwala, T. H. Brintlinger, T. Mueller, H. G. Park, and T. J. Kempa, “Substrate-directed synthesis of MoS_2 nanocrystals with tunable dimensionality and optical properties,” *Nature Nanotechnology*, vol. 15, pp. 29–34, 1 2020.

[85] T. Hu, J. Zhou, J. Dong, and Y. Kawazoe, “Electronic and magnetic properties of armchair MoS_2 nanoribbons under both external strain and electric field, studied by first principles calculations,” *Journal of Applied Physics*, vol. 116, 8 2014.

[86] G. Ghimire, R. K. Ulaganathan, A. Tempez, O. Ilchenko, R. R. Unocic, J. Heske, D. I. Miakota, C. Xiang, M. Chaigneau, T. Booth, P. Bøggild, K. S. Thygesen, D. B. Geohegan, and S. Canulescu, “Molybdenum disulfide nanoribbons with enhanced edge nonlinear response and photoresponsivity,” *Advanced Materials*, vol. 35, 8 2023.

[87] A. Splendiani, L. Sun, Y. Zhang, T. Li, J. Kim, C. Y. Chim, G. Galli, and F. Wang, “Emerging photoluminescence in monolayer MoS_2,” *Nano Letters*, vol. 10, pp. 1271–1275, 4 2010.

[88] P. Johari and V. B. Shenoy, “Tuning the electronic properties of semiconducting transition metal dichalcogenides by applying mechanical strains,” *ACS Nano*, vol. 6, pp. 5449–5456, 6 2012.

[89] L. Dong, R. R. Namburu, T. P. O’Regan, M. Dubey, and A. M. Dongare, “Theoretical study on strain-induced variations in electronic properties of monolayer MoS_2,” vol. 49, pp. 6762–6771, Kluwer Academic Publishers, 2014.

[90] J. Pető, G. Dobrik, G. Kukucska, P. Vancsó, A. A. Koós, J. Koltai, P. Nemes-Incze, C. Hwang, and L. Tapasztó, “Moderate strain induced indirect bandgap and conduction electrons in MoS_2 single layers,” *npj 2D Materials and Applications*, vol. 3, 12 2019.

[91] Z. Li, Y. Lv, L. Ren, J. Li, L. Kong, Y. Zeng, Q. Tao, R. Wu, H. Ma, B. Zhao, D. Wang, W. Dang, K. Chen, L. Liao, X. Duan, X. Duan, and Y. Liu, “Efficient strain modulation of 2d materials via polymer encapsulation,” *Nature Communications*, vol. 11, 12 2020.

[92] H. J. Conley, B. Wang, J. I. Ziegler, R. F. Haglund, S. T. Pantelides, and K. I. Bolotin, “Bandgap engineering of strained monolayer and bilayer MoS_2,” *Nano Letters*, vol. 13, pp. 3626–3630, 2013.

[93] G. A. Ermolaev, Y. V. Stebunov, A. A. Vyshnevyy, D. E. Tatarkin, D. I. Yakubovsky, S. M. Novikov, D. G. Baranov, T. Shegai, A. Y. Nikitin, A. V. Arsenin, and V. S. Volkov, “Broadband optical properties of monolayer and bulk MoS_2,” *npj 2D Materials and Applications*, vol. 4, 12 2020.

[94] J. R. Young, M. Chilcote, M. Barone, J. Xu, J. Katoch, Y. K. Luo, S. Mueller, T. J. Asel, S. K. Fullerton-Shirey, R. Kawakami, J. A. Gupta, L. J. Brillson, and E. Johnston-Halperin, “Uniform large-area growth of nanotemplated high-quality monolayer MoS_2,” *Appl. Phys. Lett*, vol. 110, p. 263103, 2017.

[95] H. Zhang, Y. Ma, Y. Wan, X. Rong, Z. Xie, W. Wang, and L. Dai, “Measuring the refractive index of highly crystalline monolayer MoS_2 with high confidence,” *Scientific Reports*, vol. 5, 2 2015.

[96] X. Yan, L. Zhu, Y. Zhou, Y. E, L. Wang, and X. Xu, “Dielectric property of MoS_2 crystal in terahertz and visible regions,” *Applied Optics*, vol. 54, pp. 6732–6736, 8 2015.

[97] Y. Wang, J. Z. Ou, A. F. Chrimes, B. J. Carey, T. Daeneke, M. M. Y. A. Alsaif, M. Mortazavi, S. Zhuiykov, N. Medhekar, M. Bhaskaran, J. R. Friend, M. S. Strano, and K. Kalantar-Zadeh, “Plasmon resonances of highly doped two-dimensional MoS_2,” *Nano Letters*, vol. 15, pp. 883–890, 2 2015.

[98] W. Zhu, F. Xiao, M. Kang, D. Sikdar, X. Liang, J. Geng, M. Premaratne, and R. Jin, “MoS_2 broadband coherent perfect absorber for terahertz waves,” *IEEE Photonics Journal*, vol. 8, 12 2016.

[99] C. C. Shen, Y. T. Hsu, L. J. Li, and H. L. Liu, “Charge dynamics and electronic structures of monolayer MoS_2 films grown by chemical vapor deposition,” *Applied Physics Express*, vol. 6, 12 2013.

[100] B. Mukherjee, F. Tseng, D. Gunlycke, K. K. Amara, G. Eda, and E. Simsek, “Complex electrical permittivity of the monolayer molybdenum disulfide (MoS_2) in near UV and visible,” *Optical Materials Express*, vol. 5, p. 447, 2 2015.

[101] Y. K. Srivastava, A. Chaturvedi, M. Manjappa, A. Kumar, G. Dayal, C. Kloc, and R. Singh, “MoS_2 for ultrafast all-optical switching and modulation of THz fano metaphotonic devices,” *Advanced Optical Materials*, vol. 5, 12 2017.

[102] A. Ramasubramaniam, “Large excitonic effects in monolayers of molybdenum and tungsten dichalcogenides,” *Physical Review B - Condensed Matter and Materials Physics*, vol. 86, 9 2012.

[103] Y. Yoon, K. Ganapathi, and S. Salahuddin, “How good can monolayer MoS_2 transistors be?,” *Nano Letters*, vol. 11, pp. 3768–3773, 9 2011.

[104] D. I. Miakota, G. Ghimire, R. K. Ulaganathan, M. E. Rodriguez, and S. Canulescu, “A novel two-step route to unidirectional growth of multilayer MoS_2 nanoribbons,” *Applied Surface Science*, vol. 619, p. 156748, 2023.

[105] C. Lee, H. Yan, L. E. Brus, T. F. Heinz, J. Hone, and S. Ryu, “Anomalous lattice vibrations of single- and few-layer MoS_2,” *ACS Nano*, vol. 4, pp. 2695–2700, 5 2010.

[106] R. Luo, W. W. Xu, Y. Zhang, Z. Wang, X. Wang, Y. Gao, P. Liu, and M. Chen, “Van der waals interfacial reconstruction in monolayer transition-metal dichalcogenides and gold heterojunctions,” *Nature Communications*, vol. 11, 12 2020. MoS_2 Raman peaks reference.

[107] D. Grischkowsky, S. Keiding, M. V. Exter, and C. Fattinger, “Far-infrared time-domain spectroscopy with terahertz beams of dielectrics and semiconductors,” *J. Opt. Soc. Am. B*, vol. 7, pp. 2006–2015, 1990.

[108] H. W. Tu, C. C. Shih, C. L. Lin, M. Z. Yu, J. J. Lai, J. C. Luo, G. L. Lin, W. B. Jian, K. Watanabe, T. Taniguchi, and C. Hu, “High field-effect performance and intrinsic scattering in the two-dimensional MoS_2 semiconductors,” *Applied Surface Science*, vol. 564, 10 2021.

[109] J. H. Strait, P. Nene, and F. Rana, “High intrinsic mobility and ultrafast carrier dynamics in multilayer metal-dichalcogenide MoS_2,” *Physical Review B - Condensed Matter and Materials Physics*, vol. 90, 12 2014.

[110] C. J. Docherty, P. Parkinson, H. J. Joyce, M. H. Chiu, C. H. Chen, M. Y. Lee, L. J. Li, L. M. Herz, and M. B. Johnston, “Ultrafast transient terahertz conductivity of monolayer MoS_2 and WSe_2 grown by chemical vapor deposition,” *ACS Nano*, vol. 8, pp. 11147–11153, 11 2014.

[111] J. Lindhard, “On the properties of a gas of charged particles,” *Matematisk-fysiske Meddelelser Kongle Danske Videnskabernes Selskab*, vol. 28, pp. 1–57, 1954.

[112] N. D. Mermin, “Lindhard dielectric function in the relaxation-time approximation,” *Physical Review B*, vol. 1, pp. 2362–2363, 3 1970.

[113] A. A. Govyadinov, S. Mastel, F. Golmar, A. Chuvilin, P. S. Carney, and R. Hillenbrand, “Recovery of permittivity and depth from near-field data as a step toward infrared nanotomography,” *ACS Nano*, vol. 8, pp. 6911–6921, 7 2014.

[114] K. S. Novoselov, A. K. Geim, S. V. Morozov, D. Jiang, Y. Zhang, S. V. Dubonos, I. V. Grigorieva, and A. A. Firsov, “Electric field effect in atomically thin carbon films,” 2004.

[115] C. Backes, A. M. Abdelkader, C. Alonso, A. Andrieux-Ledier, R. Arenal, J. Azpeitia, N. Balakrishnan, L. Banszerus, J. Barjon, R. Bartali, S. Bellani, C. Berger, R. Berger, M. M. B. Ortega, C. Bernard, P. H. Beton, A. Beyer, A. Bianco, P. Bøggild, F. Bonaccorso, G. B. Barin, C. Botas, R. A. Bueno, D. Carriazo, A. Castellanos-Gomez, M. Christian, A. Ciesielski, T. Ciuk, M. T. Cole, J. Coleman, C. Coletti, L. Crema, H. Cun, D. Dasler, D. D. Fazio, N. Díez, S. Drieschner, G. S. Duesberg, R. Fasel, X. Feng, A. Fina, S. Forti, C. Galiotis, G. Garberoglio, J. M. García, J. A. Garrido, M. Gibertini, A. Gölzhäuser, J. Gómez, T. Greber, F. Hauke, A. Hemmi, I. Hernandez-Rodriguez, A. Hirsch, S. A. Hodge, Y. Huttel, P. U. Jepsen, I. Jimenez, U. Kaiser, T. Kaplas, H. Kim, A. Kis, K. Papagelis, K. Kostarelos, A. Krajewska, K. Lee, C. Li, H. Lipsanen, A. Liscio, M. R. Lohe, A. Loiseau, L. Lombardi, M. F. López, O. Martin, C. Martín, L. Martínez, J. A. Martin-Gago, J. I. Martínez, N. Marzari, Álvaro Mayoral, J. McManus, M. Melucci, J. Méndez, C. Merino, P. Merino, A. P. Meyer, E. Miniussi, V. Miseikis, N. Mishra, V. Morandi, C. Munuera, R. Muñoz, H. Nolan, L. Ortolani, A. K. Ott, I. Palacio, V. Palermo, J. Parthenios, I. Pasternak, A. Patane, M. Prato, H. Prevost, V. Prudkovskiy, N. Pugno, T. Rojo, A. Rossi, P. Ruffieux, P. Samorì, L. Schué, E. Setijadi, T. Seyller, G. Speranza, C. Stampfer, I. Stenger, W. Strupinski, Y. Svirko, S. Taioli, K. B. K. Teo, M. Testi, F. Tomarchio, M. Tortello, E. Treossi, A. Turchanin, E. Vazquez, E. Villaro, P. R. Whelan, Z. Xia, R. Yakimova, S. Yang, G. R. Yazdi, C. Yim, D. Yoon, X. Zhang, X. Zhuang, L. Colombo, A. C. Ferrari, and M. Garcia-Hernandez, “Production and processing of graphene and related materials,” *2D Materials*, vol. 7, p. 022001, 1 2020.

[116] J. D. Buron, D. H. Petersen, P. Bøggild, D. G. Cooke, M. Hilke, J. Sun, E. Whiteway, B. S. Jessen, P. F. Nielsen, O. Hansen, A. Yurgens, and P. U. Jepsen, “Graphene conductance uniformity mapping,” *Nano Letters*, vol. 12, pp. 5074–5081, 10 2012.

[117] J. D. Buron, F. Pizzocchero, P. U. Jepsen, D. H. Petersen, J. M. Caridad, B. S. Jessen, T. J. Booth, and P. Bøggild, "Graphene mobility mapping," *Scientific Reports*, vol. 5, p. 12305, 7 2015.

[118] P. Bøggild, D. M. A. Mackenzie, P. R. Whelan, D. H. Petersen, J. D. Buron, A. Zurutuza, J. Gallop, L. Hao, and P. U. Jepsen, "Mapping the electrical properties of large-area graphene," *2D Materials*, vol. 4, p. 042003, 9 2017.

[119] P. R. Whelan, B. Zhou, O. Bezencenet, A. Shivayogimath, N. Mishra, Q. Shen, B. S. Jessen, I. Pasternak, D. M. A. Mackenzie, J. Ji, S. Cunzhi, P. Seneor, B. Dlubak, B. Luo, F. Østerberg, D. Huang, H. Shi, D. Luo, M. Wang, R. S. Ruoff, B. Conran, C. McAleese, C. Huyghebaert, S. Brems, T. Booth, I. Napal, W. Strupinskii, D. H. Petersen, S. Forti, C. Coletti, A. Jouvray, K. B. K. Teo, A. Centeno, A. Zurutuza, P. Legagneux, P. U. Jepsen, and P. Boggild, "Case studies of electrical characterisation of graphene by terahertz time-domain spectroscopy," *2D Materials*, 1 2021.

[120] J. Zhang, X. Chen, S. Mills, T. Ciavatti, Z. Yao, R. Mescall, H. Hu, V. Semenenko, Z. Fei, H. Li, V. Perebeinos, H. Tao, Q. Dai, X. Du, and M. Liu, "Terahertz nanoimaging of graphene," *ACS Photonics*, vol. 5, pp. 2645–2651, 7 2018.

[121] Z. Yao, V. Semenenko, J. Zhang, S. Mills, X. Zhao, X. Chen, H. Hu, R. Mescall, T. Ciavatti, S. March, S. R. Bank, T. H. Tao, X. Zhang, V. Perebeinos, Q. Dai, X. Du, and M. Liu, "Photo-induced terahertz near-field dynamics of graphene/inas heterostructures," *Optics Express*, vol. 27, p. 13611, 5 2019.

[122] D.-S. Kim, O. H. Kwon, O. A. Y. Nikitin, S. Ahn, L. Martín-Moreno, F. J. García-Vidal, S. Ryu, H. Min, and Z. H. Kim, "Stacking structures of few-layer graphene revealed by phase-sensitive infrared nanoscopy," *ACS Nano*, vol. 9, pp. 6765–6773, 2015.

[123] E. H. Hwang and S. D. Sarma, "Dielectric function, screening, and plasmons in two-dimensional graphene," *Physical Review B - Condensed Matter and Materials Physics*, vol. 75, 5 2007.

[124] P. L. Bhatnagar, E. P. Gross, , and M. Krook, "Model for collision processes in gases. i. small amplitude processes in charged and neutral one-component systems ," 1954.

[125] S. Rumyantsev, G. Liu, W. Stillman, M. Shur, and A. A. Balandin, "Electrical and noise characteristics of graphene field-effect transistors: Ambient effects, noise sources and physical mechanisms," *Journal of Physics Condensed Matter*, vol. 22, 10 2010.

[126] L. Gammelgaard, J. M. Caridad, A. Cagliani, D. M. MacKenzie, D. H. Petersen, T. J. Booth, and P. Bøggild, "Graphene transport properties upon exposure to pmma processing and heat treatments," *2D Materials*, vol. 1, 12 2014.

[127] L. A. Falkovsky, “Optical properties of graphene,” *Journal of Physics: Conference Series*, vol. 129, 2008.

[128] P. A. D. Gonçalves, *Plasmonics and Light–Matter Interactions in Two-Dimensional Materials and in Metal Nanostructures.* Springer International Publishing, 2020.

[129] G. Lovat, G. W. Hanson, R. Araneo, and P. Burghignoli, “Semiclassical spatially dispersive intraband conductivity tensor and quantum capacitance of graphene,” *Physical Review B - Condensed Matter and Materials Physics*, vol. 87, 3 2013.

[130] G. Liu, S. Rumyantsev, M. S. Shur, and A. A. Balandin, “Origin of 1/f noise in graphene multilayers: Surface vs. volume,” *Applied Physics Letters*, vol. 102, 3 2013.

[131] J. Ye, M. F. Craciun, M. Koshino, S. Russo, S. Inoue, H. Yuan, H. Shimotani, A. F. Morpurgo, and Y. Iwasa, “Accessing the transport properties of graphene and its multilayers at high carrier density,” *Proceedings of the National Academy of Sciences*, vol. 108, pp. 13002–13006, 8 2011.

[132] S. Latil and L. Henrard, “Charge carriers in few-layer graphene films,” *Physical Review Letters*, vol. 97, 2006.

[133] C. Casiraghi, A. Hartschuh, E. Lidorikis, H. Qian, H. Harutyunyan, T. Gokus, K. S. Novoselov, and A. C. Ferrari, “Rayleigh imaging of graphene and graphene layers,” *Nano Letters*, vol. 7, pp. 2711–2717, 9 2007.

[134] B. S. Jessen, P. R. Whelan, D. M. Mackenzie, B. Luo, J. D. Thomsen, L. Gammelgaard, T. J. Booth, and P. Bøggild, “Quantitative optical mapping of two-dimensional materials,” *Scientific Reports*, vol. 8, 12 2018.

[135] L. L. Hale, T. Siday, and O. Mitrofanov, “Near-field imaging and spectroscopy of terahertz resonators and metasurfaces [invited],” *Optical Materials Express*, vol. 13, p. 3068, 11 2023.

[136] N. J. van Hoof, D. R. Abujetas, S. E. ter Huurne, F. Verdelli, G. C. Timmermans, J. A. Sánchez-Gil, and J. G. Rivas, “Unveiling the symmetry protection of bound states in the continuum with terahertz near-field imaging,” *ACS Photonics*, vol. 8, pp. 3010–3016, 10 2021.

[137] R. Büchner, T. Weber, L. Kühner, S. A. Maier, and A. Tittl, “Tip coupling and array effects of gold nanoantennas in near-field microscopy,” *ACS Photonics*, vol. 8, pp. 3486–3494, 12 2021.

[138] L. Thomas, T. Hannotte, C. N. Santos, B. Walter, M. Lavancier, S. Eliet, M. Faucher, J. F. Lampin, and R. Peretti, “Imaging of thz photonic modes by scattering scanning near-field optical microscopy,” *ACS Applied Materials and Interfaces*, vol. 14, pp. 32608–32617, 7 2022.

[139] A. Bhattacharya and J. G. Rivas, “Full vectorial mapping of the complex electric near-fields of thz resonators,” *APL Photonics*, vol. 1, 11 2016.

[140] A. O. Sboychakov, A. L. Rakhmanov, A. V. Rozhkov, and F. Nori, “Electronic spectrum of twisted bilayer graphene,” *Physical Review B*, vol. 92, p. 075402, 8 2015.

[141] H. Polshyn, M. Yankowitz, S. Chen, Y. Zhang, K. Watanabe, T. Taniguchi, C. R. Dean, and A. F. Young, “Large linear-in-temperature resistivity in twisted bilayer graphene,” *Nature Physics*, vol. 15, pp. 1011–1016, 10 2019.

[142] E. S. Morell, J. D. Correa, P. Vargas, M. Pacheco, and Z. Barticevic, “Flat bands in slightly twisted bilayer graphene: Tight-binding calculations,” *Physical Review B*, vol. 82, p. 121407, 9 2010.

[143] G. Tarnopolsky, A. J. Kruchkov, and A. Vishwanath, “Origin of magic angles in twisted bilayer graphene,” *Physical Review Letters*, vol. 122, p. 106405, 3 2019.

[144] P. Moon and M. Koshino, “Optical absorption in twisted bilayer graphene,” *Physical Review B*, vol. 87, p. 205404, 5 2013.

[145] C. Shen, Y. Chu, Q. Wu, N. Li, S. Wang, Y. Zhao, J. Tang, J. Liu, J. Tian, K. Watanabe, T. Taniguchi, R. Yang, Z. Y. Meng, D. Shi, O. V. Yazyev, and G. Zhang, “Correlated states in twisted double bilayer graphene,” *Nature Physics*, vol. 16, pp. 520–525, 5 2020.

[146] M. Yankowitz, S. Chen, H. Polshyn, Y. Zhang, K. Watanabe, T. Taniguchi, D. Graf, A. F. Young, and C. R. Dean, “Tuning superconductivity in twisted bilayer graphene,” *Science*, vol. 363, pp. 1059–1064, 3 2019.

[147] M. Oh, K. P. Nuckolls, D. Wong, R. L. Lee, X. Liu, K. Watanabe, T. Taniguchi, and A. Yazdani, “Evidence for unconventional superconductivity in twisted bilayer graphene,” *Nature*, vol. 600, pp. 240–245, 12 2021.

[148] A. L. Sharpe, E. J. Fox, A. W. Barnard, J. Finney, K. Watanabe, T. Taniguchi, M. A. Kastner, and D. Goldhaber-Gordon, “Emergent ferromagnetism near three-quarters filling in twisted bilayer graphene,” *Science*, vol. 365, pp. 605–608, 8 2019.

[149] K. Seo, V. N. Kotov, and B. Uchoa, “Ferromagnetic mott state in twisted graphene bilayers at the magic angle,” *Physical Review Letters*, vol. 122, p. 246402, 6 2019.

[150] Y. Saito, J. Ge, K. Watanabe, T. Taniguchi, and A. F. Young, “Independent superconductors and correlated insulators in twisted bilayer graphene,” *Nature Physics*, vol. 16, pp. 926–930, 9 2020.

[151] M. Xie and A. MacDonald, "Nature of the correlated insulator states in twisted bilayer graphene," *Physical Review Letters*, vol. 124, p. 097601, 3 2020.

[152] B. Zhou, J. Balgley, P. Lampen-Kelley, J.-Q. Yan, D. G. Mandrus, and E. A. Henriksen, "Evidence for charge transfer and proximate magnetism in graphene–$\alpha - \mathrm{RuCl}_3$ heterostructures," *Physical Review B*, vol. 100, p. 165426, 10 2019.

[153] Y. Wang, J. Balgley, E. Gerber, M. Gray, N. Kumar, X. Lu, J.-Q. Yan, A. Fereidouni, R. Basnet, S. J. Yun, D. Suri, H. Kitadai, T. Taniguchi, K. Watanabe, X. Ling, J. Moodera, Y. H. Lee, H. O. H. Churchill, J. Hu, L. Yang, E.-A. Kim, D. G. Mandrus, E. A. Henriksen, and K. S. Burch, "Modulation doping via a two-dimensional atomic crystalline acceptor," *Nano Letters*, vol. 20, pp. 8446–8452, 12 2020.

[154] V. Leeb, K. Polyudov, S. Mashhadi, S. Biswas, R. Valentí, M. Burghard, and J. Knolle, "Anomalous quantum oscillations in a heterostructure of graphene on a proximate quantum spin liquid," *Physical Review Letters*, vol. 126, p. 097201, 3 2021.

[155] J. Balgley, J. Butler, S. Biswas, Z. Ge, S. Lagasse, T. Taniguchi, K. Watanabe, M. Cothrine, D. G. Mandrus, J. Velasco, R. Valentí, and E. A. Henriksen, "Ultrasharp lateral p–n junctions in modulation-doped graphene," *Nano Letters*, vol. 22, pp. 4124–4130, 5 2022.

[156] S. Biswas, Y. Li, S. M. Winter, J. Knolle, and R. Valentí, "Electronic properties of $\alpha - \mathrm{RuCl}_3$ in proximity to graphene," *Physical Review Letters*, vol. 123, p. 237201, 12 2019.

[157] E. Gerber, Y. Yao, T. A. Arias, and E.-A. Kim, "Ab initio mismatched interface theory of graphene on $\alpha - \mathrm{RuCl}_3$: Doping and magnetism," *Physical Review Letters*, vol. 124, p. 106804, 3 2020.

[158] D. J. Rizzo, B. S. Jessen, Z. Sun, F. L. Ruta, J. Zhang, J.-Q. Yan, L. Xian, A. S. McLeod, M. E. Berkowitz, K. Watanabe, T. Taniguchi, S. E. Nagler, D. G. Mandrus, A. Rubio, M. M. Fogler, A. J. Millis, J. C. Hone, C. R. Dean, and D. N. Basov, "Charge-transfer plasmon polaritons at graphene/$\alpha - \mathrm{RuCl}_3$ interfaces," *Nano Letters*, vol. 20, pp. 8438–8445, 12 2020.

[159] D. J. Rizzo, S. Shabani, B. S. Jessen, J. Zhang, A. S. McLeod, C. Rubio-Verdú, F. L. Ruta, M. Cothrine, J. Yan, D. G. Mandrus, S. E. Nagler, A. Rubio, J. C. Hone, C. R. Dean, A. N. Pasupathy, and D. N. Basov, "Nanometer-scale lateral p–n junctions in graphene/$\alpha - \mathrm{RuCl}_3$ heterostructures," *Nano Letters*, vol. 22, pp. 1946–1953, 3 2022.

[160] J. D. Buron, *Terahertz transport dynamics of graphene charge carriers.* PhD thesis, 2013.